UNIVERSITE DE PROVENCE (Aix-Marseille I)

Ecole Doctorale Sciences pour l'Ingénieur:
Mécanique, Physique, Micro-nanoélectronique

Institut Universitaire des Systèmes
Thermiques Industriels - UMR CNRS 7343

Thèse

pour obtenir le grade de

DOCTEUR

D'AIX-MARSEILLE UNIVERSITÉ

Spécialité : Énergétique

présentée par

Rodrigo Andrés DEMARCO BULL

Modelling thermal radiation and soot formation in buoyant diffusion flames

Directeur de thèse : Jean-Louis CONSALVI

Soutenue le 09 Juillet 2012 devant la commission d'examen :

Président :	
Jean-Claude LORAUD	Professeur, Aix-Marseille Université/IUSTI, Marseille
Rapporteurs :	
Fengshan LIU	Senior Research Officer, National Research Council/ Ottawa, Canada
Guillaume LEGROS	Maître de Conférences, Univ. Pierre et Marie Curie/IJLRA, Saint-Cyr
Examinateurs :	
Denis LEMONNIER	Directeur de Recherche au CNRS/PPRIME, Poitiers
Rodolphe VAILLON	Directeur de Recherche au CNRS/CETHIL, Lyon
Jean-Louis CONSALVI	Maître de Conférences, Aix-Marseille Université/IUSTI, Marseille
Invitée :	
Laurence RIGOLLET	Adjointe au chef du SA2I, IRSN

Modelling thermal radiation and soot formation in buoyant diffusion flames

Summary: The radiative heat transfer plays an important role in fire problems since it is the dominant mode of heat transfer between flames and surroundings. It controls the pyrolysis, and therefore the heat release rate, and the growth rate of the fire. In the present work a numerical study of buoyant diffusion flames is carried out, with the main objective of modelling the thermal radiative transfer and the soot formation/destruction processes. In a first step, different radiative property models were tested in benchmark configurations. It was found that the FSCK coupled with the Modest and Riazzi mixing scheme was the best compromise in terms of accuracy and computational requirements, and was a good candidate to be implemented in CFD codes dealing with fire problems. In a second step, a semi-empirical soot model, considering acetylene and benzene as precursor species for soot nucleation, was validated in laminar coflow diffusion flames over a wide range of hydrocarbons (C1-C3) and conditions. In addition, the optically-thin approximation was found to produce large discrepancies in the upper part of these small laminar flames. Reliable predictions of soot volume fractions require the use of an advanced radiation model. Then the FSCK and the semi-empirical soot model were applied to simulate laboratory-scale and intermediate-scale pool fires of methane and propane. Predicted flame structures as well as the radiant heat flux transferred to the surroundings were found to be in good agreement with the available experimental data. Finally, the interaction between radiation and turbulence was quantified.

Keywords: Thermal radiation, Soot model, Laminar diffusion flames, Turbulent diffusion flames.

Modélisation du rayonnement thermique et de la formation de suies dans des flammes de diffusion affectes par des forces de flottabilité

Résumé : Le rayonnement joue un rôle fondamental dans les problèmes d'incendie puisque c'est le mode dominant de transfert de chaleur entre la flamme et le milieu environnant. Il contrôle la pyrolyse, et donc la puissance de flamme, et la vitesse de croissance de l'incendie. Etudier les flammes de diffusion contrôlées par les forces de flottabilité est une première étape pour comprendre et de prédire les incendies. Le principal objectif de ce travail est de modéliser le transfert radiatif et les processus de production/destruction de la suie dans ce type de flammes. Premièrement, différents modèles de propriétés radiatives des gaz ont été comparés dans des configurations tests. Il est apparu que le modèle FSCK couplé avec le schéma de mélange de Modest et Riazzi est le meilleur compromis entre précision et temps de calcul, ce modèle étant un bon candidat pour être implémenté dans des codes CFD traitant des problèmes d'incendie. Dans un second temps, un modèle de formation/oxydation des suies semi-détaillé, considérant l'acétylène et le benzène comme précurseurs, a été validé dans des flammes de diffusion laminaires de type coflow sur une large gamme d'hydrocarbures (C1-C3) et pour différentes conditions. Ensuite, le FSCK et le modèle de formation/destruction ont été appliqués pour simuler des feux de nappe de méthane et de propane aux échelles du laboratoire et intermédiaire. Les structures de flamme prédites ainsi que les flux radiatif transférés au milieu environnant ont montré un bon accord avec les résultats

expérimentaux disponibles. Finalement, les interactions entre le rayonnement et la turbulence ont été quantifiées.

Mots-clés : Rayonnement thermique, Modèle de suies, Flamme laminaire de diffusion, Flamme turbulente de diffusion.

Institut Universitaire des Systèmes Thermiques Industriels - CNRS UMR 7343

5 Rue Enrico Fermi 13453 Marseille Cedex 13

RESUME EN FRANÇAIS

Ce travail de thèse s'inscrit dans le cadre du thème 2 du laboratoire ETIC qui lie l'IRSN et l'IUSTI pour une durée de 4 ans. L'objectif de ce thème est de mieux appréhender la combustion en milieux sous ventilés et notamment les phénomènes de pyrolyse à l'origine du dégagement de chaleur par le feu. La modélisation de ces phénomènes nécessite d'une part de décrire de manière fine les processus de dégradation thermique au niveau de la phase condensée et d'autre part de modéliser correctement les flux de chaleur transférés par la flamme vers cette phase. Dans le cadre de feux à grande échelle, comme ceux susceptibles d'avoir lieu dans les centrales nucléaires, ce transfert de chaleur s'effectue majoritairement par le rayonnement des particules de suie. Ces dernières sont des particules de carbone solide, formées dans la partie riche en combustible des flammes, qui émettent du rayonnement de manière continue de un point de vue spectrale. L'objectif de cette thèse est de développer un modèle radiatif et un modèle de formation des suies susceptibles d'être implémentés dans les modèles CFD pour étudier des configurations sous-ventilées caractéristiques des incendies en milieux confinés.

La prédiction précise des transferts radiatifs dans les flammes est une tâche difficile dans la mesure où elle nécessite une solution précise de l'équation de transfert radiatif, une modélisation propre de la dépendance spectrale du rayonnement des espèces (produits de combustion en phase gazeuse et suies) et une évaluation propre des interactions entre le rayonnement et la turbulence si nécessaire. Les modèles radiatifs utilisés dans le cadre des codes de calcul traitant des problèmes d'incendie sont souvent extrêmement simplifiés. Ces simplifications sont généralement dues au fait qu'introduire des modèles plus complexes donne des temps de calcul prohibitifs lorsque l'écoulement, la combustion et les transferts radiatifs sont résolus de manière couplés. Les gaz de combustion participant d'un point de vue radiatif et les suies sont alors traités comme des milieux gris tandis que les interactions entre le rayonnement et la turbulence sont ignorées.

Les processus de formation/oxydation des suies sont également complexes à modéliser. La chimie des suies étant une chimie relativement lente, il n'est pas possible de découpler ces processus de l'écoulement en considérant des relations d'état (appelés « flammelettes ») comme cela est généralement le cas pour les produits gazeux de combustion. De plus, comme mentionné précédemment, les suies affectent l'écoulement à travers les pertes radiatives qu'elles génèrent. De manière imagée la production des suies s'effectue selon les étapes suivantes: la première étape est la génération du benzène et du phényle qui jouent un rôle important dans la formation des hydrocarbures aromatiques polycycliques (HAP), à l'origine de la nucléation des suies. A partir de benzène et du phényle, des molécules de HAP de plus en plus grandes se forment, tout d'abord en ayant une géométrie bidimensionnelle puis une géométrie tridimensionnelle. On suppose que la première apparition d'un HAP tridimensionnel coïncide avec la nucléation d'une particule de suie. Les particules de suie croissent ensuite en masse du fait de deux mécanismes : le premier mécanisme est relatif à l'addition d'acétylène sur la surface des particules de suie tandis que le second est relatif à la condensation des HAP. D'un point de vue de la dynamique des particules, les particules de suie

coagulent et s'agglomèrent pour former de larges chaines de géométrie fractale de particules primaires. De façon concomitante, elles perdent de la masse sous l'action d'espèces oxydantes telles que l'oxygène ou le radical hydroxyle. La prise en compte de tous ces phénomènes nécessite de développer une cinétique chimique extrêmement détaillée en phase gazeuse de sorte à prédire les concentrations des espèces à l'origine des mécanismes décrits précédemment. D'autre part il est nécessaire de formuler un modèle cinétique pour prendre en compte les interactions entre la phase gazeuse et les particules de suie. Finalement il faut développer un modèle de dynamique des particules de suie pour simuler les interactions entre elles. Une modélisation détaillée est généralement assez lourde et nécessitera des simplifications en vue d'applications à des flammes turbulentes. Dans cette thèse, on se limitera à la mise en place de modèles de formation des suies semi-détaillés, suffisamment précis pour les hydrocarbures usuels C1-C3 mais suffisamment simplifiés pour permettre la simulation des flammes turbulentes.

Le premier chapitre de la thèse évoque le contexte, les phénomènes physiques mis en jeu, ainsi qu'une revue bibliographique sur les modèles de propriétés radiatives de gaz, sur les interactions entre le rayonnement et la turbulence et sur les modèles de formation/oxydation des suies. Le plan de l'exposé est donné : le Chapitre 2 concernera la formulation des différents modèles de propriétés des gaz qui seront comparés dans le chapitre 3 à travers des calculs radiatifs découplés effectués sur des configurations de référence. Le chapitre 4 sera dédié à la formulation et à la validation d'un modèle de suies. Un modèle de suies semi-détaillé sera considéré. La validation s'effectuera en considérant des flammes laminaires axisymétriques générées par des hydrocarbures usuels de type C1-C3. Des flammes normales et inverses seront considérées, ces dernières présentant du point de vue de la formation des suies les mêmes caractéristiques que les flammes en milieux sous-ventilés. Avant d'effectuer ces comparaisons, l'hypothèse de milieu optiquement mince, susceptible d'être valide dans ces petites flammes laminaires, sera évaluée. Le chapitre 5 concernera l'application aux flammes turbulentes. Le modèle radiatif présentant le meilleur compromis en termes de précision et de temps de calcul ainsi que le modèle de formation des suies seront utilisés en vue de simuler sept flammes de diffusion turbulentes contrôlées par les forces de flottabilité. Deux combustibles ayant des propensions à générer des suies complètement différentes, le méthane et le propane, seront retenus. Des flammes à l'échelle du laboratoire, c'est-à-dire générées par des brûleurs poreux d'environ 30cm, et des flammes à une échelle intermédiaire, c'est-à-dire générées par des brûleurs poreux de 1 m, seront considérées.

Le chapitre 2 présente les modèles de propriétés radiatives des gaz considérés dans cette étude. On peut classifier ces modèles en bandes étroites, bandes larges, globaux et gris. Après avoir présenté l'équation de transfert radiatif (ETR) dans la première section, les modèles à bandes étroites sont abordés. Il s'agit des modèles dont les bandes sont suffisamment étroites pour pouvoir considérer que la seule grandeur qui varie sur ces bandes est le coefficient d'absorption des gaz, l'intensité du corps noir et les propriétés radiatives des particules et des parois étant constantes. Le modèle statistique à bandes étroites, qui sera utilisé comme référence dans le chapitre suivant en l'absence de calculs « raies par raies », est présenté en premier. Le modèle statistique à bande étroite k-corrélé est ensuite décrit. Ce modèle est basé sur le concept de k-distribution qui permet de réduire l'intégration sur un grand nombre de longueur d'ondes à une intégration simple en utilisant quelques points de quadrature. Une des difficultés du modèle réside dans le fait que la prise en compte d'un mélange de gaz nécessite des temps de calcul prohibitifs si l'approche « corrélée » est appliquée. Dans ce cas le nombre d'équations de transfert radiatif à résoudre sur une bande étroite est ${N_G}^{N_S}$ où

N_G est le nombre de points de quadrature utilisés pour l'intégration et N_S est le nombre d'espèces gazeuses, respectivement. Par conséquent un certain nombre de modèles de mélange, destinés à générer une k-distribution unique pour le mélange de gaz et donc à réduire le nombre de résolutions de l'ETR à N_G, sont discutés. Cette section est close par la présentation du modèle « Grey Narrow Band », GNB, qui détermine le coefficient d'absorption sur une bande étroite à partir de la transmissivité. Le seul modèle à bandes larges considéré dans cette étude est le « Grey Wide Band » (GWB). Ce modèle est implémenté dans le logiciel de calcul FDS, destiné à simuler les incendies. Il est construit en calculant la moyenne de Planck pour le coefficient d'absorption sur six bandes. La version grise simplifiée de ce modèle est également présentée. Les modèles globaux sont ensuite considérés : la « somme pondérée de gaz gris » (WSGG) est discutée. Ce modèle, relativement simple, est largement utilisé dans les applications. Les modèles « Full-Spectrum correlated-k » (FSCK), «Full Spectrum Scaled-k" (FSSK) et " Spectral Line-based Weighted-sum-of-gray-gases" (SLW) sont basés sur le même concept de « ré-ordonnement » du coefficient d'absorption sur la totalité du spectre à l'aide d'une « Full Spectrum k-distribution ». Ils sont donc présentés dans la même section. Le FSK et le SLW diffèrent par la manière avec laquelle la « Full Spectrum k-distribution » est intégrée : le FSK utilise un schéma de quadrature tandis que le SLW considère un simple schéma trapézoïdal. L'application de ces méthodes à des configurations non-isothermes et non-homogènes nécessite d'introduire l'hypothèse que le coefficient d'absorption est soit « corrélé » ou « scalé ». Le modèle FSK a été explicité dans les deux cas (FSCK pour « corrélé » et FSSK pour « scaled ») et les deux formulations sont présentées. De plus, il est alors nécessaire d'introduire un état de référence. La manière dont ce dernier est défini est également présentée. La procédure pour assembler la « FS k-distribution » à partir d'une base de données à bandes étroites est ensuite décrite. Le dernier modèle de propriétés radiatives des gaz considéré est l'approximation de milieu optiquement mince, qui sera utilisée dans le chapitre 4. Finalement, les méthodes utilisées pour résoudre l'ETR sont brièvement décrites.

Dans le chapitre 3, les modèles radiatifs présentés précédemment sont testés dans les configurations de référence mettant en jeu de la vapeur d'eau, du dioxyde de carbone et des suies. Les suies sont supposées rayonner dans le régime de Rayleigh. Les calculs radiatifs sont effectués de manière découplée, les températures et les concentrations des espèces étant prescrites. Des configurations monodimensionnelles et bidimensionnelles axisymétriques sont étudiées. Pour chaque configuration, des milieux isothermes et homogènes et non-isothermes et non-homogènes sont considérés. Dans chaque cas des fractions volumiques de suie variant sur une large gamme sont utilisées. Le modèle statistique à bandes étroites est utilisé comme référence. Les conclusions suivantes peuvent être tirées de cette étude : 1) Le modèle SNBCK, couplé avec la base de données à 367 bandes étroites, est recommandé si des solutions avec un haut degré de précision sont nécessaires. L'approche « correlée » est la plus précise pour traiter les mélanges de gaz mais elle est très lourde d'un point de vue du temps de calcul. Son efficacité en termes de temps calcul peut être considérablement améliorée sans altérer la qualité des solutions en utilisant à la fois une base de données à 43 bandes étroites et le modèle de mélange développé par Modest and Riazzi [114]. Si le modélisateur est seulement intéressé par des quantités intégrées spectralement, un schéma de quadrature de Gauss-Legendre à deux points offre une précision acceptable, réduisant considérablement le temps de calcul par rapport au schéma de Gauss-Legendre à 7 points. 2) les modèles gris conduisent à des prédictions erronées bien qu'ils nécessitent des temps de calcul faibles. Leur utilisation devrait être évitée si des solutions précises sont désirées. 3) Les modèles

WSGG et le GWB améliorent les prédictions des modèles gris. Cependant, ils ne peuvent pas être utilisés avec confiance sur une large gamme de chargements en particules de suie. Le modèle WSGG produit généralement des solutions plutôt satisfaisantes mais peut conduire à des erreurs significatives dans certaines situations. Le Modèle GWB conduit, quant à lui, à de mauvaises solutions pour des fractions volumiques de suie faibles et modérées. Lorsque le rayonnement des suies domine, il fournit des solutions acceptables en dépit de fortes erreurs locales. 4) Les modèles FSCK et SLW, utilisant le « FS k-distributions » générées à partir d'une base de données à bandes étroites et du schéma de mélange de Modest et Riazzi [114], constituent un bon compromis entre précision et temps de calcul. Ce schéma de mélange est plus précis que ceux développés par Solovjov et Webb [144]. Le FSCK est généralement plus précis que le SLW, conduisant à des solutions de qualité en considérant un schéma de quadrature de Gauss-Legendre à seulement 7 points.

Dans le chapitre 4, le modèle de formation/oxydation des suies est présenté et validé sur des flammes laminaires axisymétriques, s'apparentant dans la configuration normale à des flammes de bougie. Un modèle de suie semi-détaillé, basé sur le benzène et l'acétylène comme espèces responsables de la nucléation et incluant également les phénomènes de croissance de surface, de coagulation et d'oxydation par les espèces O, OH, et O_2, est utilisé. Quinze flammes axisymétriques, normales ou inverses, sont utilisées pour la validation. Quatre hydrocarbures (méthane, éthylène, propane, propylène) sont considérés. Les faibles dimensions de ces flammes suggèrent que l'approximation de milieu optiquement mince peut être utilisée. Une étude est effectuée, en considérant deux flammes d'éthylène « suitante » et « non-suitante », pour s'assurer de la validité de cette hypothèse. Les conclusions suivantes peuvent être tirées de cette étude : 1) la contribution du rayonnement lié au CO peut être ignorée, 2) la réabsorption des gaz et des suies sont des caractéristiques cruciales pour estimer précisément les pertes radiatives, les températures et les fractions volumiques des suies. Par conséquent, l'approximation de milieu optiquement mince conduit à des prédictions erronées pour les flammes lourdement chargées en suie, spécialement dans leur partie supérieure où l'oxydation a lieu, 3) la nature spectrale des gaz et des suies est une caractéristique importante pour obtenir des prédictions fiables. Par conséquent, l'utilisation de modèle gris devrait être évitée. 4) Le FSCK fournit des résultats similaires à ceux obtenus avec le SNBCK avec un gain considérable en termes de temps de calcul. Il est donc une bonne alternative pour être implémenté pour étudier les processus de formation/oxydation des suies dans les flammes laminaires axisymétriques. 5) Le modèle de suies considéré conduit à des prédictions acceptables pour l'ensemble des flammes étudiées. Deux ensembles de paramètres ont été nécessaires pour obtenir un accord raisonnable, un pour les hydrocarbures C1-C2 et un autre pour les C3. Cependant ces deux ensembles de paramètres ne diffèrent que par la valeur du facteur pré-exponentiel pour le terme de croissance de surface. Ce modèle est jugé suffisamment robuste pour être appliqué pour simuler les flammes turbulentes.

Dans le chapitre 5, sept flammes de diffusion turbulentes de méthane et de propane contrôlées par les forces de flottabilité sont simulées. Deux types d'échelle sont considérés : des flammes à l'échelle du laboratoire, i.e. générées par des brûleurs ayant un diamètre de l'ordre d'une trentaine de centimètres et des flammes à l'échelle intermédiaire, c'est-à-dire générées par des brûleurs de diamètre de l'ordre du mètre. En accord avec les conclusions des chapitres 3 et 4, le FSCK couplé avec le modèle de mélange de Modest et Riazzi [114] est utilisé pour prendre en compte le caractère spectral des produits de combustion gazeux et des suies. Conformément aux conclusions du chapitre 4, les processus de formation/oxydation des suies sont modélisés en utilisant une variante du modèle

de Leung *et al*. [77]. Finalement les interactions entre le rayonnement et la turbulence sont discutées et quantifiées. Les conclusions suivantes peuvent être tirées: 1) Le modèle numérique est capable de fournir des prédictions fiables concernant la structure de ces flammes, 2) les pertes radiatives et les flux radiatifs sur des cibles environnantes sont correctement reproduits, 3) l'utilisation de modèle gris pour traiter les gaz de combustion conduit à des sur-prédictions importantes des pertes radiatives. D'autre part, l'hypothèse de modèle gris pour les particules de suie est valide en première approximation, conduisant à un gain substantiel en termes de temps de calcul, 4) les interactions entre le rayonnement et la turbulence augmentent les pertes et les flux radiatifs. La corrélation complète entre le coefficient d'absorption des gaz et la fonction de Planck doit être prise en compte pour modéliser correctement l'influence des interactions entre le rayonnement et la turbulence sur le terme d'émission. Les effets de la turbulence sur le terme d'absorption ne peuvent pas être négligés dans la mesure où ils contribuent à accroitre l'absorption de manière non-négligeable

Le chapitre 6 reprend les conclusions générales de l'étude ainsi que les perspectives de ce travail. De manière générale, ce travail a permis de dégager un modèle radiatif et un modèle de formation des suies susceptibles d'être utilisés pour analyser les effets de la sous-ventilation dans le cadre des incendies en milieu confiné. Les perspectives à ce travail sont nombreuses et diverses. La modélisation de la formation des suies pour des combustibles plus complexes est une voie de recherche, la mise en place de modèles semi-détaillés pour ce type de combustibles étant un challenge. L'influence de l'oxygène sur la formation des suies en flammes laminaires axisymétriques, normale ou inverse constitue un sujet de recherche fondamental. Une prédiction de la puissance de la flamme en considérant un couplage direct entre la flamme et le combustible solide est également à retenir dans les perspectives à court terme. Pour ce faire, des modèles de pyrolyse précis et efficaces devront être développés. Finalement, on retiendra l'application à des feux sous-ventilés, introduisant la problématique du modèle de combustion à choisir pour ce type de configurations.

Contents

List of Tables

List of Figures

Nomenclature

A_s	soot surface area per unit volume, [m^{-1}]
a	weight function for full-spectrum *k*-distribution methods, [-]
a_j	weight factors for sum-of-gray-gases, [-]
C	soot constant, [-]
C_a	agglomeration constant rate, [-]
C_{min}	number of carbon atoms in the incipient soot particle, [-]
C_p	thermal capacity, [J kg^{-1} K^{-1}]
D_{th}	thermal diffusivity, [m^2 s^{-1}]
d	diameter, [m]
$E_{r,i}$	relative error at mesh point i ($E_{r,i} = (\varphi_i - \varphi_{ref,i})/\lvert\varphi_{ref,i}\rvert$), [-]
$E_{r,mean}$	mean relative error over N mesh points ($\sum_{i=1}^{N}\lvert E_{r,i}\rvert/N$), [-]
$E_{r,max}$	maximum relative error over N mesh points ($\max_{i=1,N}\lvert E_{r,i}\rvert$), [-]
Fr	Froude number
f	*k*-distribution function, [m^{-1}]
f_s	soot volume fraction, [-]
G	buoyancy production term of turbulence
g	acceleration of gravity, [m s^{-2}]
g	cumulative *k*-distribution function, [-]
g_i	quadrature points, [-]
H	Heaviside function
h	enthalphy, [J]
I	radiative intensity
I_b	blackbody intensity (Planck function)
k	absorption coefficient variable, [m^{-1}]
k	turbulent kinetic energy
k_i	*i*-th reaction rate constant
l	geometrical path length, [m]
L	length, [m]

L_v	latent heat of vaporization, [J kg^{-1}]
M_c	soot density, [kg kmol^{-1}]
$\dot{m}''_{pyr}$	pyrolysis mass flow, [kg s^{-1}]
$\vec{n}$	unit surface normal, [-]
N	number of mesh points considered for error estimation, [-]
N_A	Avogadro's Number (=6.022×10^{26} part kmol^{-1})
N_G	number of quadrature points or gray gases, [-]
N_S	number of gaseous species, [-]
N_s	soot number density per unit of mixture, [kg m^{-3} s^{-1}]
P	shear production term of turbulence
P	probability density function
Pr	Prandlt Number
p	pressure, [Pa]
$\dot{Q}$	heat release rate, [W]
q_R	radiative flux, [w m^{-2}]
R	radius, [m]
R	CO_2/H_2O molar fraction ratio
r	radial coordinate, [m]
r_i	*i*-th reaction rate
S	surface, [m^2]
S_c	Schmidt Number
S_{burn}	pyrolysing surface , [m^2]
S_m	soot mas fraction source term
S_N	soot number density source term
$\vec{s}$	unit vector into a given direction, [-]
T	temperature, [K]
u	scaling function
u_r, u_z	velocity, [m s^{-1}]
V	volume, [m^3]
V_T	thermophoretic velocity of soot, [m s^{-1}]
w_i	quadrature weights, [-]
X_i	molar fraction of species i, [-]

X_R	radiative loss fraction or enthalpy defect parameter, [-]
x	coordinate, [m]
Y_i	mass fraction of species i, [-]
Y_s	soot mass fraction, [-]
Z	mixture fraction, [-]
z	axial coordinate, [m]

Greek

β	thermal expansion factor, [K^{-1}]
χ	scalar dissipation rate, [s^{-1}]
$\Delta\nu$	narrow band interval, [m^{-1}]
δ	Dirac-delta function, [-]
$\overline{\delta}$	SNB parameters
ϵ	emissivity, [-]
ϵ	turbulent kinetic energy dissipation
φ	output variable for error analysis
φ	oxidation efficiency factor
Φ	transported quantity
$\underline{\phi}$	composition variable vector (T, p, x_i, f_v)
Γ	diffusion coefficient
$\overline{\gamma}$	SNB parameter
κ	absorption coefficient, [m^{-1}]
κ	Boltzmann constant (=1.38×10^{-23} J.K^{-1})
$\overline{\kappa}$	SNB parameter
κ_P	Planck absorption coefficient, [m^{-1}]
λ	thermal conductivity, [W m^{-1} K^{-1}]
μ	dynamic viscosity, [kg m^{-1} s^{-1}]
ν	wavenumber, [m^{-1}]
Ω	solid angle, [sr]
ρ	density, [kg m^{-3}]
σ	Stephan-Boltzmann constant (=5.67×10-8 W m^{-2} K^{-4})
τ	transmissivity, [-]

$\widetilde{\xi''^2}$	mixture fraction variance

Subscript

0	reference state
∞	ambient condition
ad	adiabatic
ag	agglomeration
e	effective
inj	injection
g	gas, or at a given cumulative k-distribution value
mix	mixture
p	Planck
ref	reference solution
rms	root mean square
s	soot
sg	surface growth
t	turbulent
u	unburned
w	wall
ν	wavenumber

Superscript

0	tabulated value
fl	flamelet
$\overline{}$	Reynolds average
$\sim$	Favre average

Acronyms

AFM	Algebraic Flux Model
ASM	Algebraic Stress Model
CF	Continuous Flame
CK	Correlated k-distribution
CFD	Computational Fluid Dynamics
CPU	Central Processing Unit
DOM	Discrete Ordinate Method
DTM	Discrete Transfer Method
ETIC	ETude de l'Incendie en milieu Confiné
EVM	Eddy-Viscosity Model
FANS	Favre-averaged Navier–Stokes
FDS	Fire Dynamic Simulator
FDSgg	GWB model, in its grey formulation with l based on the global domain
FDSgl	GWB model, in its grey formulation with l based on the local control volume
FS	Full-Spectrum
FSCK	Full-Spectrum Correlated-k
FSK	Full-Spectrum k-distribution
FSSK	Full-Spectrum Scaled-k
FVM	Finite Volume Method
GNB	Grey-Narrow-Band
GNBg	Grey-Narrow-Band with l based on the global domain
GNBl	Grey-Narrow-Band with l based on the local control volume
GWB	Grey Wide Band
GWBg	Grey Wide Band in its grey formulation
HACA	Hydrogen Abstraction Carbon Addition
HRR	Heat Release Rate
IF	Intermittent Flame
IDF	Inverse Diffusion Flame

IRSN	Institut de Radioprotection et de Sûreté Nucléaire
IUSTI	Institut Universitaire des Systèmes Thermiques Industriels
LBL	Line by line
LES	Large Eddy Simulation
LRC	Laboratoire de Recherche Commun
MFS	Mixed Full Spectrum
MNB	Mixed Narrow Band
M&R	Modest and Riazzi
NB	Narrow Band
NS flame	Non-Smoking flame
NSC	Nagle and Strickland-Constable
OTA	Optically Thin Approximation
OTFA	Optically Thin Fluctuation Approximation
PAH	Poly-Aromatic Hydrocarbons
pdf	probability density function
rms	root mean square
RT	Ray Tracing
RTE	Radiative Transfer Equation
S flame	Smoking flame
SLF	Steady Laminar Flamelet
SLW	Spectral-Line-Based Weighted-Sum-of-Grey-Gases
SNB	Statistical Narrow Band
SNBCK	Statistical Narrow Band Correlated-k
SNBCKgs	SNBCK model considering grey soot
TDMA	Tridiagonal Matrix Algorithm
TRI	Turbulence - Radiation Interactions
WSGG	Weighted-Sum-of-Grey-Gases
WSGGgg	Weighted-Sum-of-Grey-Gases, grey formulation, l based on the global domain
WSGGgl	Weighted-Sum-of-Grey-Gases, grey formulation, l based on the local control volume

1 Introduction

This chapter is the global introduction of the manuscript. The context of the study as well as the main objectives will be described firstly. Secondly, a bibliographical study of the different physical phenomena encountered will be addressed. Finally, an overview of the manuscript will be given.

1.1 Contexts and objectives of the study

1.1.1 Fire growth mechanisms

In unwanted fires, the gaseous combustible required to sustain the flames is released from the thermal degradation of solid and/or liquid fuels. This process, known as pyrolysis, is the main responsible of the heat release rate of the fire and its growth rate.

Figure 1.1 shows the main interactions which control the combustion of a liquid fuel. Although this description is oversimplified since it is limited to liquid, for which the pyrolysis processes are less complex than for solids, it allows drawing a large amount of insights concerning the interactions between the gas phase and the condensed materials. The flame depicted in this figure is a diffusion flame characteristic of unwanted fires. The word diffusion means that fuel and oxidant are not initially premixed. The flow is controlled by buoyancy, the Froude number, $Fr = u_{inj}^2/gL$, being typically in the range 10^{-6}-10^{-2}. In the previous expression u_{inj} is the injection velocity of the pyrolysis products (gaseous products released from the condensed material), g is the gravitational acceleration and L is a characteristic length of the problem, typically the flame length or the diameter of the burner in the present example. The combustion occurs in a self-sustained regime. The liquid is vaporized under the influence of the convective and radiative fluxes transferred by the flame. Gaseous combustible products are then transported by convection and diffusion toward the reaction zone where they mix with the oxygen of air to react. For well-ventilated medium, the chemistry can generally be assumed to be fast as compared to the mixing which allows simplifying the description of the gas phase combustion.

The dominant mode of heat transfer between the flame and the condensed material depends on the size of the pool: at small-scale the heat transfer is dominated by convection whereas for pool fires with diameter greater than 1m thermal radiation prevails. Let us consider the energy balance at the surface of a liquid fuel:

$$\dot{m}''_{pyr} L_v = \dot{q}''_{fl,rad} + \dot{q}''_{fl,conv} - \dot{q}''_{rr} - \dot{q}''_{cond} \quad (1)$$

where $\dot{m}''_{pyr}$ is the pyrolysis mass flow rate. $\dot{q}''_{fl,rad}$, $\dot{q}''_{fl,conv}$, $\dot{q}''_{rr}$ and $\dot{q}''_{cond}$ represent the heat flux transferred from the flame by radiation and convection, the heat flux emitted by the fuel surface and the heat flux transferred in the material by conduction. L_v is the latent heat of vaporization. This expression can be simplified for large-scale fires on the basis of the analysis carried out previously:

$$\dot{m}''_{pyr} L_v \cong \dot{q}''_{fl,rad} \quad (2)$$

On the other hand the heat release rate can be written as:

$$\dot{Q} = \dot{m}''_{pyr} S_{burn} \Delta h_c \quad (3)$$

where S_{burn} represents the pyrolysing surface and Δh_c is the heat of combustion. As a consequence, it appears that for large-scale fires the radiative flux transferred from the flame toward the condensed material play a crucial role in the determination of the heat release rate. Gaseous combustion products (CO_2, H_2O, CO) and soot are responsible of the radiative heat flux from the flame. Gaseous species emit radiation in some discrete bands, whereas the radiation from soot is continuous, covering the entire thermal spectrum. The contribution of soot depends widely on the combustible. Nevertheless, in "real" fires, their contribution usually prevails [26].

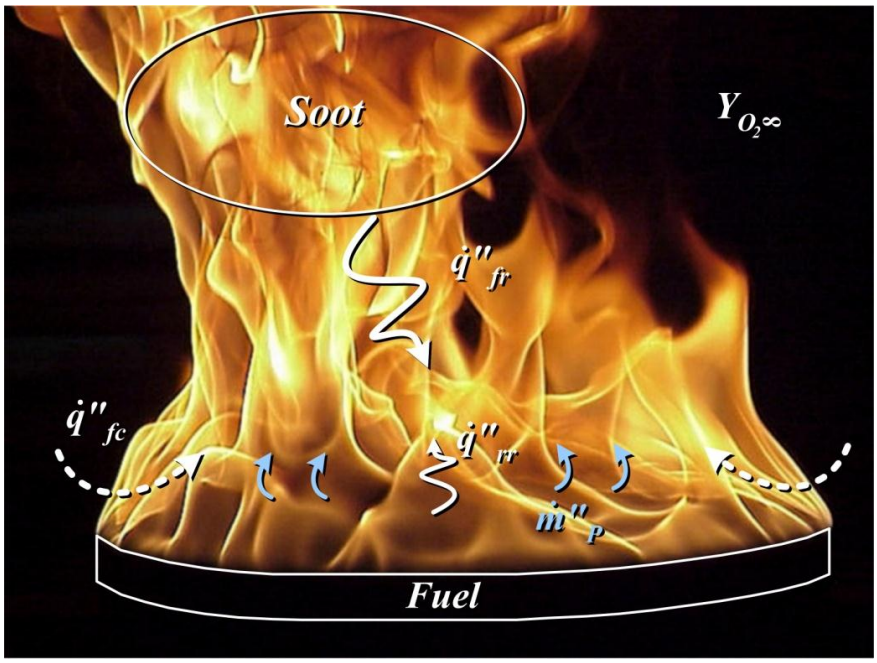

Figure 1.1. Scheme of a pool fire

The pyrolysis process, which results from the interactions between the flame and the burning condensed fuel, controls the heat release rate. The interaction between the flame and the not-yet ignited condensed material controls the flame spread and the fire growth. This process can be viewed as a succession of piloted ignitions, the flame usually acting as both a heater and a pilot. The not-yet ignited condensed material, located ahead of the fire front, is heated by the flame. When its temperature becomes sufficiently high it starts releasing gaseous combustible products, which mix with the ambient air to form a flammable mixture. This latter can be ignited by the flame, ensuring the spread process. In large-scale fires, the heat transfer from the flame to the surface of material to be ignited is dominated by radiative heat transfer.

It appears that radiative flux, emitted by the gaseous combustion products and soot but also by the hot walls in the case of confined fires, play an important role in fire growth [26]. It is then essential to predict correctly the soot concentrations as well as the corresponding radiative heat transfer.

1.1.2 Influence of under-ventilation

Fires in nuclear plants are characterized by a high level of enclosure, leading to conditions for combustion generally different from those encountered in well-ventilated fires. Air feeding the flame becomes rapidly vitiated, which leads to incomplete combustion. Gaseous combustibles, soot, carbon monoxide and other pollutants escape then from the fire and are released in the surroundings. This can lead to extremely dangerous hazards, especially if the gaseous combustibles mix with air and encounter points with a sufficiently high temperature to ignite this mixture.

If we restrict our analysis to the interactions gas/condensed material, the vitiation of air should lead to a reduction in flame temperature, implying a decrease in the radiative heat transfers and pyrolysis mass flow rates. These trends appear clearly in the evolution of the pyrolysis mass flow rates measured during the PRISME experiments performed at the IRSN for different levels of vitiation [106]. On the other hand, the high temperature of the enclosure wall surrounding the fire should produce a supplementary source of heating for the pyrolysis and growth processes. The soot production should be also considerably affected [76]: on one hand the decrease in flame temperature should reduce the soot formation rates, leading to lower soot concentrations. On the other hand, decreasing the oxidation process should lead to higher soot concentration. As a consequence, it is difficult to determine a priori how the total amount of soot will evolve when the oxygen concentration will decrease.

1.1.3 Objectives

This PhD thesis is included in the second theme of the LRC ETIC (ETude de l'incendie en milieu Confiné). This project is a virtual laboratory between the IUSTI and the IRSN with duration of 4 years. The objective of this theme is to provide a better understanding of the phenomena involved during under-oxygenated fires. One of the main issues is to predict the heat release rate in this kind of configuration. As seen previously, an accurate modelling of the processes occurring at the level of the condensed material is then required: the thermal degradation processes of the condensed material have to be accurately modelled [75], but also (and above all??) "boundary conditions" have to be correctly described. These boundary conditions are expressed in terms of heat flux transferred from the flame, dominated as mentioned previously by the radiative heat flux from soot.

The objective of this work is to provide the basis for a radiative model and a soot formation/destruction model designed to be used to study under-ventilated fires. In view of numerical applications, it is necessary to consider some considerations in numerical resources in the formulation of the model. A permanent concern will be to find a compromise between accuracy and CPU time. Once these models developed and validated in well-defined configurations (benchmarks, laminar flames …), they will be applied to scenarios directly related to unwanted fires, especially buoyant turbulent diffusion flames.

1.2 Bibliographic survey

1.2.1 Radiative transfer modelling

An accurate prediction of radiative heat transfer in turbulent flames is a difficult task since it requires a precise solution of the Radiative Transfer Equation (RTE), a proper modelling of the spectral dependence of radiating species (radiatively participating gases and soot particles) and a proper evaluation of the Turbulence-Radiation Interactions (TRI). The different radiative property models used in this study are described in the second chapter. Here a brief description of the works of the

literature is provided. The section 1.2.1.1 will concern a literature review of the radiative property models, whereas the section 1.2.1.2 will address the interactions between radiation and turbulence.

1.2.1.1 Radiative property models

The determination of accurate solutions for radiative heat transfer is difficult in media involving combustion products due to the strong dependence of the absorption coefficient of gases on the wavenumber. For example, the line-by-line method (LBL) requires about 10^6 resolutions of the RTE to consider this effect [109], involving computation requirements which are too large for practical applications. Various alternative gas property models have been developed or extended in recent decades to overcome this difficulty.

Narrow Band (NB) models, such as the Statistical Narrow Band (SNB) and the Correlated *k*-distribution (CK), have retained attention [48,72,109,146,152]. In particular, studies were conducted to establish new databases for these methods [146,152]. The accuracy of the SNB model, which gives the spectral transmissivity over a NB, is well recognized. However, this method suffers from two drawbacks. Firstly it cannot be easily coupled with differential solution methods of the RTE, such as the Discrete Ordinates Method (DOM) [43], the Finite Volume Method (FVM) [131] or the P1 [136], without the introduction of approximations leading to a loss in accuracy [81,162]. In order to keep its accuracy the SNB model is generally coupled with the Ray Tracing (RT) method. As the RT method is time consuming, the SNB model is often limited to determining radiative intensity along a line of sight [66,67,137] or to providing benchmark solutions when LBL solutions are not available [17,50,83]. Secondly it is not a feasible way to account for scattering unless the Monte Carlo method is used, which increases even more the computational time. The CK method, on the other hand, gives the absorption coefficient, so it can be coupled with arbitrary RTE solvers and can account for scattering. This method consists in reordering the absorption coefficient in a NB into a smooth, monotonically increasing function called the *k*-distribution. Integration over numerous wavenumbers can then be replaced by a simple quadrature scheme with few points. The CK method is accurate but very demanding computationally, especially when dealing with a gas mixture due to overlapping bands [50]. Several ways have been found to reduce its computational cost [84,85,86,96,114,144].

Global models are generally limited to problems with grey walls and/or particles. The Weighted-Sum-of-Grey-Gases (WSGG) model, initially developed by Hottel and Sarofim [60], can be applied to any method for solving the RTE [110]. It consists in replacing the non-grey gas by a number of grey gases, for which the radiative rates are computed independently. The Spectral-Line-Based Weighted-Sum-of-Grey-Gases (SLW) [32,34,35] and the Full-Spectrum *k*-distribution model (FSK) [111] can be viewed as improvements of the WSGG. The basic idea of these methods consists in reordering the absorption coefficient over the entire spectrum into a smooth, monotonically increasing function called the full-spectrum (FS) *k*-distribution. The integration over about 10^6 lines is then reduced to the integration of a single smooth function. As shown by Modest [109], the SLW and FSK models differ in the methodology employed to perform this integration. The SLW uses a simple trapezoidal scheme, defining N_G grey gases, whereas the FSK uses a quadrature scheme. Solovjov and Webb [144,145] and Modest and Riazzi [114] developed models to generate a single FS *k*-distribution for a mixture of gases and soot.

The accuracy and the computational efficiency of some of these models were assessed by considering 1D [9,31], 2D [50], 2D axisymmetric [17] and 3D radiative benchmarks [16]. Goutiere *et*

al. [50] and Coelho [16] found that SNB and SNBCK models are the most accurate models to predict radiative heat transfer in medium containing CO_2 and H_2O but are too time consuming to be used for engineering applications. They also found that the SLW is the best compromise in terms of accuracy and computational efficiency. In another work dealing with axisymmetric enclosures with non-grey sooting media, Coelho *et al.* [17] showed that the DOM combined with the CK method provides less accurate solutions than the RT method used together with the SNB model, but is more adapted for practical applications. Very recently Porter *et al.* [127] applied the FSCK to model radiative heat transfer in 3D enclosures containing CO_2 and H_2O, confirming the reliability of this method by comparisons with SNB solutions.

Simplified radiative property models, such as the WSGG [8,14,123] or grey models [143,150,155], are often used in computational fluid dynamics (CFD) simulations of fire problems. The main reason is that implementing more sophisticated models may become extremely time consuming when fluid flow/combustion/radiative heat transfer are coupled. The use of simplified radiative property models is then justified on the basis that the continuous radiation of soot dominates the radiative heat transfer. A Planck-mean absorption coefficient is generally applied to model the radiative contribution of non-grey soot particles [14,143]. Band models were also implemented in CFD models. Yan and Holmstedt [159,160] and Zhang *et al.* [165] applied the SNB model coupled with the Discrete Transfer Method (DTM). Simulations with Fire Dynamics Simulator (FDS) can be achieved by using a grey wide band (GWB) model [99]. This model is based on the computation of a Planck-mean absorption coefficient on each wide band from RADCAL [51].

1.2.1.2 Turbulence – Radiation interactions

TRI are an important issue in problems involving turbulent flames, their modelling being fundamental if accurate predictions of temperature, radiative fluxes [19] and production of pollutants such as NO [55] or soot [105] are desired.

Taking TRI into account requires the modelling of two terms. The first term, known as “absorption TRI”, represents the nonlinear coupling between incident radiation and the local absorption coefficient. It is the consequence of property fluctuations across the domain and its modelling requires having a detailed knowledge of the instantaneous fields of temperature and species. Absorption TRI is generally neglected by considering the Optically Thin Fluctuation Approximation (OTFA), i.e. assuming that the local intensity is weakly correlated with the local absorption coefficient. This approximation was found to be valid over a wide range of conditions [19], with the exception of large-scale sooting flames [103]. The second term, referred to as “emission TRI”, is determined on the basis of local properties only and can be evaluated by using either presumed probability density function (pdf) approaches [18] or pdf composition methods [78,79,103,104,105,153]. Li and Modest [78,79] and Habibi *et al*. [55] isolate and quantify different levels of closure for emission TRI in turbulent methane jet flames and showed that the complete absorption coefficient-Planck function correlation must be considered to obtain a reliable evaluation.

A significant amount of studies considered decoupled fluid flow/radiative transfer calculations by specifying both the temperature and the species concentrations as input data [49,66,67]. The methodology initiated by Faeth and co-workers consisted in solving the instantaneous RTE along a line of sight by using stochastic methods to prescribe the instantaneous scalar data. This model was systematically applied to a vast quantity of fuels burning in still air, considering both non-luminous

and luminous flames. The authors established that radiative emission from a flame may be as much as 50 to 300% higher than would be expected based on mean values of temperature and absorption coefficient. Coupled fluid flow/radiative transfer calculations were also carried out. Modest and co-workers [103,104,105,153] proposed a comprehensive formulation, combining a photon Monte Carlo method with a composition pdf method, which allows an accurate description of both absorption and emission TRI. This model was applied to investigate the influence of TRI in non-sooting and sooting jet flames. They showed that the absorption TRI is negligible in lab-scale flames as long as soot levels are of the order of few ppm. Supplementary calculations [103] showed that this conclusion does not hold in large-scale flames where absorption TRI can always be neglected in the gas-phase radiation but is of the order of 10% in soot radiation. In addition, the emission TRI in soot radiation was found to be reduced as compared to lab-scale flames, this being the possible consequence of negative temperature-soot volume fraction correlations.

Among the above-mentioned studies very few were dedicated to the influence of TRI on turbulent buoyant diffusion flames representative of unwanted fires. Fischer *et al*. [42] and Klassen *et al*. [64] evidenced the importance of TRI on the prediction of radiative intensity in pool fires by carrying out decoupled fluid flow/radiative calculations. The computations of Fischer *et al*. [42] were based on the measured mean temperature, root mean square (rms) values of temperature fluctuations and species concentration coupled with a prescribed pdf of the temperature. Mean radiation intensities along the axis of a 0.5m ethanol pool fire were found to be 25-80% higher when TRI are considered. Klassen *et al*. [60] carried out calculations of radiative intensities and radiative fluxes in heavily sooting toluene pool fires by using time series of emission soot volume fractions and temperatures. They concluded that the use of mean values of soot volume fraction and temperature may result in an underestimation of one order of magnitude of the radiative intensities and radiative fluxes. Nevertheless, despite these early works, the simulations of buoyant flames traditionally ignored the couplings between radiation and turbulence. A notable exception is the work of Snegirev [143] who model TRI in a simplified manner: the fluctuations of species concentration were ignored and the grey absorption coefficient and the emission term were expanded into Taylor series around mean temperatures. High order fluctuations were truncated and the truncation error was estimated from two constants adjusted to match experimental radiant fractions and radiative fluxes on remote targets. However, no information was reported about the effects of TRI on flame structure.

1.2.2 Modelling of soot formation/destruction processes

Soot is an agglomerate of particles, which vary in structure and size [73]. The main constituent of soot is carbon and some minor amounts of hydrogen and oxygen. Depending on the surrounding gas, other species may adsorb onto the surface of soot. Although many properties of soot have been identified, it has not been possible to uniquely define the chemical composition of soot.

The size of the smallest soot particle follows the limits of experimental research. The size of the smallest primary particle is detected with an electron microscope and has a size of 20*nm* [80]. Soot is produced during the combustion of hydrocarbons under fuel-rich conditions at high temperatures. The emission of soot from a flame is determined by its formation and oxidation processes.

Two difficulties exist in the modelling of soot concentrations:

- The first difficulty can be analysed from Figure 1.2 which shows the characteristic time scales for the different physical and chemical processes. When the chemistry is sufficiently fast, i.e.

characteristic times for chemical processes are much faster than those of the flow, the chemical reactions occur in a quasi-steady state and adjust immediately to the flow conditions. In this case, the chemistry and the mixing can be decoupled. This is the basis concept of the flamelet. We can then generate state relationships for the different reactive scalars, such as the temperature or the species mass fraction, as a function of a reduced number of parameters describing the local flow conditions (mixture fraction, scalar dissipation rate, radiative loss). Figure 1.2 shows that the chemistry associated to soot, and more generally to pollutants, is slow. As a consequence, the simplifications described previously cannot be rigorously applied.

- The second difficulty comes from the fact that, contrary to NO and other pollutants, the soot acts on the flow through the radiative losses that they produce. As a consequence, the formation of soot cannot be considered a posteriori, i.e. once the flow field has been predicted. This implies that reduced or simplified soot models must be developed in view of applications. It is also required to take into account for radiative heat transfer in an accurate manner, soot formation/oxidation processes being sensitive to temperature. The effects of the coupling between soot formation and radiative heat transfer will be analysed in chapter 4 in the case of laminar coflow diffusion flames.

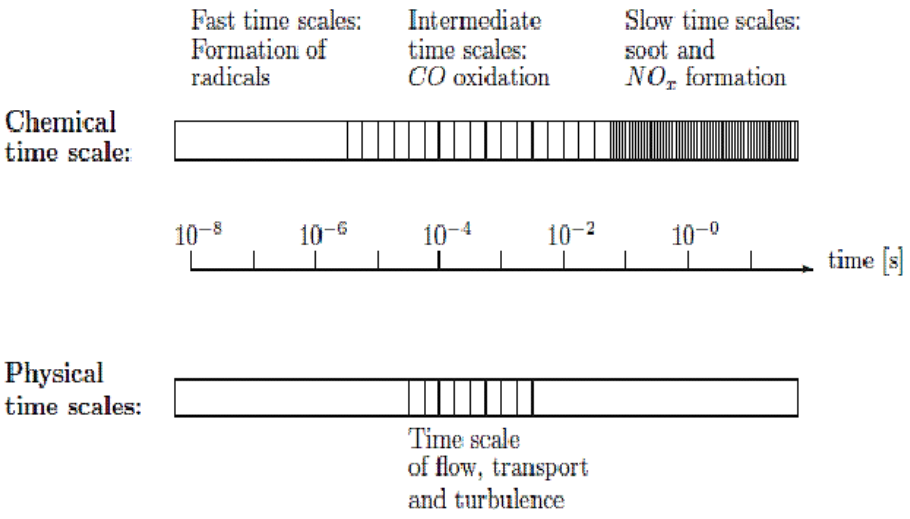

Figure 1.2. Characteristic times for the chemical and physical processes (according to Maas and Pope [94]).

The more-detailed soot models of today describe the formation of soot in eight steps [2,4,5,38] (see Figure 1.3):

1. Gas phase reactions: the first step in soot formation is the formation of benzene (C_6H_6) and phenyl (C_6H_5).

2. Poly-aromatic Hydrocarbons (PAH) grow in two-dimension through the HACA (Hydrogen Abstraction Carbon Addition) mechanism and condensation of PAH.
3. The nucleation of soot particles: this is the first step where two-dimensional PAH merge into three-dimensional soot particles.
4. Condensation: The particles grow via condensation of a two-dimensional PAH on a three-dimensional PAH.
5. Surface growth: soot particles grow in mass through reactions between the gaseous species and the surface of soot particle. Acetylene (C_2H_2) is the dominant species in this step.
6. Coagulation: two soot particles merge.
7. Agglomeration: large chains of primary particles are formed.
8. Oxidation: The soot particle loses mass in reactions with gas phase molecules O_2 and OH.

As a consequence, detailed soot models require describing the following mechanisms:

1. A gas phase kinetic mechanism sufficiently large to predict the concentrations of the chemical species involved in the soot production mechanism (C_2H_2, C_6H_5, C_6H_6, PAH …).
2. A soot kinetic model (interactions between soot particle and surrounding gas) including nucleation, mass growth and oxidation.
3. A dynamic of soot particles (interactions between soot particles). Including coagulation and agglomeration. The dynamic of the soot particles can be treated by three different ways:
    - By using a moment method where the moments of the size distribution of soot particles are solved [2,3,4,5,44].
    - By using a sectional method where the size distribution of soot particles is divided into discrete sections [46].
    - By using stochastic methods [5].

Detailed models were applied to laminar [4,38] and turbulent [3] flames. However, they are too much expensive to be applied to turbulent flames, especially if the flamelet laminar concept cannot be considered as it is probably the case for under-ventilated fires. It is then interesting to use semi-detailed models, although these latter are less general. Semi-detailed models were used with success to predict soot formation in laminar [1,88,89,90,92] and turbulent [39,65,71] flames. The model derived initially by Leung and Lindstedt [77], and further improved by other authors belongs to this category. This semi-detailed model will be presented in details in Chapter 4. As compared to detailed models, some simplifications are introduced:

- Gaseous species involved in the nucleation step of soot particles are limited to acetylene and/or benzene and phenyl. This simplification is based on the fact that acetylene and benzene are key species in the formation of large PAH. It allows reducing the size of the gas phase kinetic mechanism and to avoid modelling the lumping process for large PAH, this latter being expensive on the computational point of view.
- Growth of soot particles due to the condensation of PAH is neglected. The growth step is usually dominated by surface growth which justifies this assumption.
- The dynamic of soot particles is simplified by considering only the two first moments of the size distribution, i.e. the soot number density and the soot volume fraction.

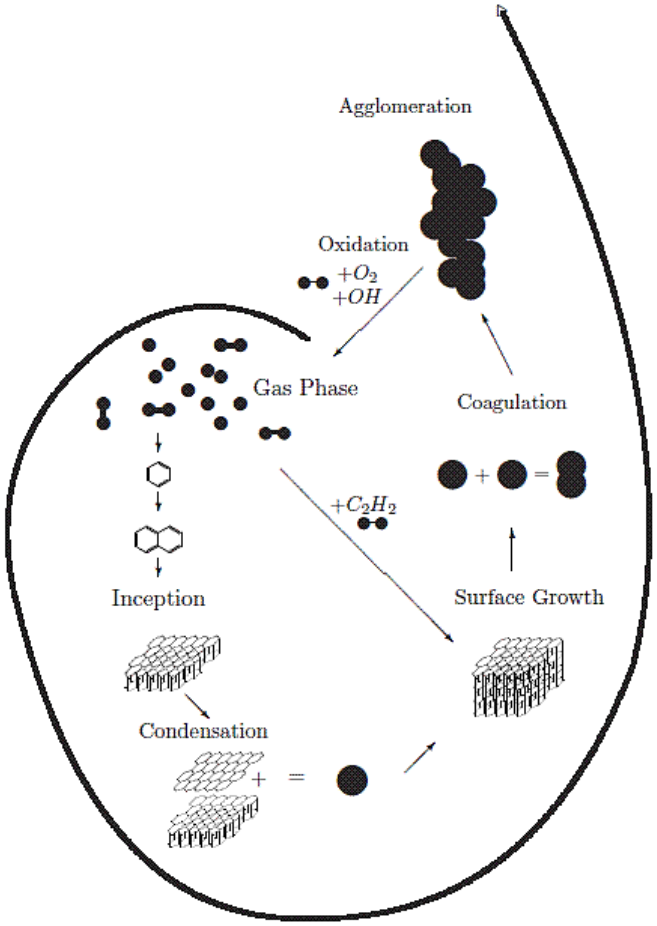

Figure 1.3. Soot formation/oxidation processes.

1.3 Overview of the manuscript

The manuscript is organized as follows: the second chapter is devoted to the presentation of the different radiative property models considered in this work. A non-exhaustive list of models will be presented and discussed.

These models will be compared in benchmark configurations in Chapter 3. Decoupled radiative calculations, using prescribed temperature and species concentration fields, will be carried out in order to determine the radiative property model to be implemented in turbulent flame calculations. The optimal model will be chosen by considering accuracy and computational efficiency as criteria.

In Chapter 4 soot models, derived from that of Leung et Lindstedt [77], will be presented and validated over a large number of laminar coflow flames by considering several hydrocarbons (methane, ethylene, propane and propylene) and several configurations. These models have been chosen from a bibliographic study. During this work, they have been found to be sufficiently complete to describe correctly soot formation/oxidation processes for usual hydrocarbons and sufficiently simple to be easily implemented in a turbulent code. The choice of laminar flames for validation is justified by the fact that they allow avoiding the difficulty introduced by the turbulence. The generalization to turbulent flames is directly based on the laminar “flamelet” concept (c.f. [39] and the work performed in Chapter 5). Moreover, these standard flames were subjected to

numerous experimental studies and, as a consequence, a large amount of data such as temperature, gaseous species concentrations and soot characteristics (volume fraction, number density …) are available for comparisons. Before performing the validations, a detailed study of the radiative heat transfer in this kind of flames and of the radiative modelling to be considered will be performed.

Chapter 5 will be devoted to the simulations of seven buoyant turbulent diffusion flames generated by porous burners. Laboratory-scale flames, i.e. flames generated by a burner of about 30cm, and intermediate-scale, i.e. flames generated by burners of the order of one meter, will be considered. Two fuels, methane, which is weakly sooting, and propane, which is moderately sooting, will be considered. The radiative property model and the soot model determined from the studies carried out in the previous chapters will be used. Model results will be compared with experimental data concerning the flame structure (temperature, velocity, species concentrations,..), the radiant fraction and the radiative flux transferred to remote surfaces. Moreover, a quantification of the interactions between radiation and turbulence will be presented.

Finally, chapter 6 will summarize the main conclusions drawn from the present work, as well as the perspectives for future works.

2 Radiative property models

As mentioned in the introduction, the spread and growth of fires is mainly controlled by the heat transferred from the flame to the surrounding combustible materials through conduction, convection and radiation. It is well established that, in most practical applications, radiative heat transfer is the dominant mode of transfer [26]. The participating radiative species involve generally gaseous combustion products (CO_2, H_2O, CO, CH_4) and soot, the concentration of soot varying widely from one combustible to another. As a result, the implementation of accurate radiative models in fire simulators is of fundamental interest.

Several radiative property models are used and compared in the present study. The objective is to determine the best compromise in terms of accuracy and computational requirement to be implemented in CFD simulators. A brief description of every model is presented in this chapter. More extended and detailed explanations can be found in [109].

The radiative transfer equation is presented in the first section. Afterward the different radiative property models used in this study are briefly described. Finally, the radiative transfer equation solvers used in this work are presented.

2.1 Radiative transfer equation

The radiative transfer equation (RTE) in an emitting/absorbing non-scattering medium may be written as

$$\frac{dI_\nu}{ds} = \kappa_\nu\left(\nu, \underline{\phi}\right)\left[I_{b\nu}(T) - I_\nu\right] \tag{4}$$

where I_ν is the spectral radiative intensity varying along a path s, $I_{b\nu}$ is the Planck function and κ_ν is the spectral absorption coefficient, which depends on the wavenumber ν and in local conditions: $\underline{\phi}$ is an array of state variables of the medium properties (T, p, x_i, f_v).

The boundary condition for a grey surface that emits and reflects diffusely is given by

$$I_{w\nu}(\vec{s}) = \epsilon_w I_{b\nu}(T_w) + \frac{1-\epsilon_w}{\pi}\int_{\vec{n}\cdot\vec{s}'<0} |\vec{n}\cdot\vec{s}'| I_\nu(\vec{s}')d\Omega' \tag{5}$$

where ϵ_w is the emissivity of the surface. $\vec{n}$ is the unit normal vector, $\vec{s}$ is the direction of the outgoing radiation intensity and $\vec{s}'$ is the incoming direction associated with the elementary solid angle $d\Omega'$.

Soot particles are assumed to be spherical and small compared to the wavelength. Rayleigh's theory is then applied to obtain the soot absorption coefficient. Scattering is ignored since it is negligible as compared to absorption within the limit of small particles. The spectral absorption coefficient of the soot is then expressed as:

$$\kappa_{\nu,s} = C f_s \nu \tag{6}$$

with $C = 5.5$. Depending on the radiative property model considered, a grey formulation for the soot absorption coefficient is required. For these cases a Planck-mean absorption coefficient is used. This coefficient is given by the following expression [109].

$$\kappa_{s,\text{Planck}} = \text{C}\,(3.83/14388 \times 10^{-6}) f_s T \tag{7}$$

2.2 SNB

The Statistical Narrow Band (SNB) model is based on the assumption that the spectrum can be subdivided into narrow bands, $\Delta\nu_i$, in which the Planck function and the soot properties can be considered as constant. The SNB model provides on each of these narrow bands the averaged transmissivity $\overline{\tau}_{\Delta\nu}$ for a homogeneous and isothermal column of length l (in cm), total pressure p (in atm) and molar fraction x_i (for the considered absorbing gases), which by using the Malkmus formulation, can be defined as:

$$\overline{\tau}_{\Delta\nu,i} = \exp\left[-2\frac{\overline{\gamma}}{\overline{\delta}}\left(\sqrt{1+x_i\, pl\overline{\kappa}\,\frac{\overline{\delta}}{\overline{\gamma}}}-1\right)\right] \tag{8}$$

The SNB parameters, $\overline{\kappa}$ (in cm^{-1} atm^{-1}), $\overline{\delta}$ (in cm^{-1}) and $\overline{\gamma}$ (in cm^{-1}), are taken from the 367 narrow bands database developed by Soufiani and Taine [146] for CO, CO_2 and H_2O with a constant interval of 25cm^{-1} in width. The Curtis-Godson approximation is used to deal with non-isothermal and/or non-homogeneous media. The transmissivity of the medium is the product of the transmissivities of the gases and soot.

This model estimates the transmissivity of the medium and thus is not appropriated to be used with differential solution methods of the RTE. The SNB model is generally coupled with the Ray Tracing (RT) method, in which each ray is followed and discretized. This implies to follow a lot of rays in order to obtain acceptable results, making this method vary time consuming and computationally expensive, so the SNB model is often limited to determining radiative intensity along a line of sight [66-137] or to provide benchmark solutions when LBL solutions are not available [83-50].

2.3 SNBCK

The Statistical Narrow Band Correlated-k (SNBCK) model is also based on subdividing the entire spectrum into narrow bands. The erratic spectral absorption coefficient is then reordered on each NB to form a monotonically increasing function, called the k-distribution, which can be easily integrated. This process produces the so-called Narrow Band Radiative Transfer Equation (NB RTE), which considerably decreases the number of RTE evaluations to be solved for a particular problem. A detailed explanation of the NB RTE development can be found in [112]. This method introduces two new variables, namely the distribution function $f\left(\underline{\phi_0}, k\right)$ and its cumulative distribution function $g\left(\underline{\phi_0}, k\right)$, given by:

$$f\left(\underline{\phi_0}, k\right) = \frac{1}{\Delta\nu}\int_{\Delta\nu}\delta\left(k-\kappa_\nu\left(\underline{\phi_0}, k\right)\right)d\nu \tag{9}$$

$$g\left(\underline{\phi_0},k\right)=\int_0^k f\left(\underline{\phi_0},k'\right)dk' \tag{10}$$

where δ is the Dirac delta function, $\kappa_\nu\left(\underline{\phi_0},k\right)$ is the spectral absorption coefficient of the medium evaluated at a reference state $\underline{\phi_0}$ and k is an absorption coefficient variable. In the case of non-homogeneous and/or non-isothermal media, the method is based on the assumption that the absorption coefficient is correlated. This means that for every wavenumber, wherever $\kappa_\nu\left(\nu,\underline{\phi_0}\right)$ has one and the same value k, $\kappa_\nu\left(\nu,\underline{\phi}\right)$ also always has one single value $k^*\left(\underline{\phi},k\right)$. The Narrow Band RTE can be expressed as:

$$\frac{dI_g}{ds}=\left(k^*\left(\underline{\phi},g\right)+\kappa_{\nu,s}\right)\left[I_{b\nu}(T)-I_g\right] \tag{11}$$

Since the function $g(k)$ increases monotonically, integration over the g-space can be performed by using a Gauss quadrature scheme. Several Gauss-Legendre quadrature are used and compared in this study, however a 7-point Gauss-Legendre quadrature scheme is usually used for the calculations. The average narrow band intensity and the total intensity can therefore be estimated as

$$\bar{I}_{\Delta\nu}=\sum_{i=1}^{N_G}w_i I_{g_i} \tag{12}$$

$$I=\sum_{\Delta\nu}\bar{I}_{\Delta\nu}\Delta\nu \tag{13}$$

where g_i and w_i are the quadrature points and the weights respectively, and N_G is the quadrature order.

For a k-distribution based on the Malkmus model the cumulative k-distribution can be determined analytically as [72]:

$$g\left(k\right)=\frac{1}{2}erfc\left[\sqrt{\frac{\bar{\gamma}}{\bar{\delta}}}\left(\sqrt{\frac{\bar{\kappa}}{k}}-\sqrt{\frac{k}{\bar{\kappa}}}\right)\right]+\frac{1}{2}\exp\left(4\frac{\bar{\gamma}}{\bar{\delta}}\right)erfc\left[\sqrt{\frac{\bar{\gamma}}{\bar{\delta}}}\left(\sqrt{\frac{\bar{\kappa}}{k}}+\sqrt{\frac{k}{\bar{\kappa}}}\right)\right] \tag{14}$$

where the SNB parameters $\bar{\kappa}$, $\bar{\delta}$ and $\bar{\gamma}$ are taken from the 367 and 43 NB databases of Soufiani and Taine [146]. The function $erfc$ corresponds to the complementary error function.

2.3.1 Treatment of gas mixtures

2.3.1.1 Correlated

For gas mixtures the classical formulation of the SNBCK model is based on a correlated treatment of the overlapping narrow bands of the different gas species. At an overlapping band (hereafter we consider an overlapping band of CO_2 and H_2O, but the methods described are applicable to other gases), the transmissivity of the mixture, $\bar{\tau}_{\Delta\nu,mix}$, obeys the multiplication property, i.e.:

$$\begin{aligned}\bar{\tau}_{\Delta\nu,mix}(l)&=\bar{\tau}_{\Delta\nu,CO_2}(l)\bar{\tau}_{\Delta\nu,H_2O}(l)\\&=\left[\sum_{i=1}^{N_G}w_i\exp\left(-k_{CO_2,i}l\right)\right]\left[\sum_{j=1}^{N_G}w_j\exp\left(-k_{H_2O,j}l\right)\right]\end{aligned} \tag{15}$$

where w_i and w_j are the weights associated with the quadrature scheme. The NB RTE for the mixture of two participating gases and soot becomes:

$$\frac{dI_{g_{i,j}}}{ds} = \left(k^*_{CO_2}\left(\underline{\phi}, g_i\right) + k^*_{H_2O}\left(\underline{\phi}, g_j\right) + \kappa_{\nu,s}\right)\left[I_{b\nu}(T) - I_{g_{i,j}}\right] \tag{16}$$

where the absorption coefficient of the mixture is the addition of the values obtained for each gas independently. The average radiation intensity of the band is then calculated as

$$\bar{I}_{\Delta\nu} = \sum_{i=1}^{N_G}\sum_{j=1}^{N_G} w_i w_j I_{g_{i,j}} \tag{17}$$

For a mixture of N_S gaseous species, this formulation, referred to as the "correlated" SNBCK model in the following, requires $(N_G)^{Ns}$ RTE to be solved on each narrow band as compared to the N_G necessary for a single gas. This drastically increases the computational time [16,50]. Simplified models for overlapping bands were then developed in order to reduce the number of RTE to be solved on each narrow band to only N_G.

2.3.1.2 Uncorrelated

The uncorrelated method assumes that, at each overlapping band, CO_2 and H_2O have the same shape of absorption coefficient distribution, but their magnitude can be different [86]. Therefore, the total absorption coefficient at the *i*-th quadrature point is simply the sum of $k_{CO_2,i}$ and $k_{H_2O,i}$, leading to

$$\bar{\tau}_{\Delta\nu,mix}(l) = \sum_{i=1}^{N_G} w_i \exp\left[-\left(k_{CO_2,i} + k_{H_2O,i}\right)l\right] \tag{18}$$

The following RTE is thus solved at each overlapping NB:

$$\begin{gathered}\frac{dI_{g_i}}{ds} = \left(k^*_{CO_2}\left(\underline{\phi}, g_i\right) + k^*_{H_2O}\left(\underline{\phi}, g_i\right) + \kappa_{\nu,s}\right)\left[I_{b\nu}(T) - I_{g_i}\right] \\ \bar{I}_{\Delta\nu} = \sum_{i=1}^{N_G} w_i I_{g_i}\end{gathered} \tag{19}$$

2.3.1.3 Mixing methods

When a mixing scheme is applied the following RTE formulation is obtained over each overlapping NB:

$$\begin{gathered}\frac{dI_{g_i}}{ds} = \left(k^*_{mix,i} + \kappa_{\nu,s}\right)\left[I_{b\nu}(T) - I_{g_i}\right] \\ \bar{I}_{\Delta\nu} = \sum_{i=1}^{N_G} w_i I_{g_i}\end{gathered} \tag{20}$$

- ***Multiplication scheme***: This model was developed by Solovjov and Webb [144] and relies on the assumption of uncorrelated absorption coefficients between gas species, through the multiplication property of the probability of independent events.

$$g_{mix}(k_{mix}) = \prod_{i=1}^{N_S} g_i(k_{mix}) \tag{21}$$

- ***Superposition scheme***: This method, also developed by Solovjov and Webb [144], relies on the assumption that the spectral lines of the component species do not significantly overlap, leading to additive values for the mixture. Solovjov and Webb noted that this model presents good results for high k values, where spectral lines are extremely narrow and spectra of different species do not significantly overlap.

$$g_{mix}(k_{mix}) = 1 - N_S + \sum_{i=1}^{N_S} g_i(k_{mix}) \tag{22}$$

- ***Scheme of Modest and Riazzi***: This model, proposed by Modest and Riazzi [114], is an extension of the concept of the multiplication of transmissivities. This model uses the concept that the transmissivity, in terms of the k-distribution for a single absorbing species, is also the definition of the Laplace transform of $f(k)$. Considering a binary mixture composed of CO_2 and H_2O, the following final expression for the gas mixture is obtained (*H* denotes the Heaviside step function):

$$\begin{aligned} g_{mix}(k_{mix}) &= \int_{g_{H_2O}=0}^{1} \int_{g_{CO_2}=0}^{1} H\left[k_{mix} - \left(k_{CO_2} + k_{H_2O}\right)\right] dg_{CO_2}\, dg_{H_2O} \\ &= \int_{g_{H_2O}=0}^{1} g_{CO_2}\left(k_{mix} - k_{H_2O}\right) dg_{H_2O} \end{aligned} \tag{23}$$

2.3.1.4 MNB database

In the cases where coupled fluid flow/combustion/radiative heat transfer calculations are performed, calculations with the SNBCK model are extremely time consuming, becoming impracticable. In order to overcome this difficulty a Mixed Narrow Band (MNB) database of k-distribution was pre-generated for 15 values of $R = X_{CO_2}/{X_{H_2O}}^0$, between 0.01 and 2.2 (0.01, 0.1, 0.2, 0.3, 0.4, 0.5, 0.6, 0.8, 1.0, 1.2, 1.4, 1.6, 1.8, 2.0, 2.2), and 23 temperatures in the range between 300 and 2500 K (every 100 K). This database was generated by considering a fixed H_2O concentration of ${X_{H_2O}}^0 = 0.1$. This procedure implies that the weak dependence of the spectral line broadening on the species mole fraction is neglected [151], allowing to express the absorption coefficient of the mixture as:

$$\kappa_{mix}(R, T, X_{H_2O}) = \frac{X_{H_2O}}{{X_{H_2O}}^0} {\kappa_{mix}}^0(R, T) \tag{24}$$

where

$${\kappa_{mix}}^0(R_i, T_j) = {\kappa_{mix}}^0\left(\kappa_{H_2O}({X_{H_2O}}^0, T_j), \kappa_{co_2}(R_i * {X_{H_2O}}^0, T_j)\right)\Big|_{i=1,15; j=1,23} \tag{25}$$

are the tabulated values calculated with the mixing model of Modest and Riazzi. For mixtures of arbitrary species mole fraction ratios and temperature, the absorption coefficient is computed from the database by carrying out linear interpolations on *R* and spline interpolations on *T*. Introducing this database has a minor influence as compared to direct SNBCK calculations.

2.4 GNB

The Grey-Narrow-Band (GNB) model assumes that the radiating gases behave like a grey gas in each NB. The following form of the RTE is solved:

$$\frac{d\bar{I}_{\Delta\nu}}{ds} = \left(\bar{\kappa}_{\Delta\nu} + \kappa_{\nu,s}\right)\left[I_{b\nu}(T) - \bar{I}_{\Delta\nu}\right] \tag{26}$$

where the grey narrow band absorption coefficient is estimated from the mixture transmissivity using the following relationship:

$$\bar{\kappa}_{\Delta\nu} = -\frac{\ln\left[\bar{\tau}_{\Delta\nu}(l)\right]}{l} \tag{27}$$

The transmissivity of the medium is taken as the product of the transmissivities of the gases and soot. The transmissivity of each gas is calculated using the 367 NB database of Soufiani and Taine [146]. The mean path-length parameter l, defined as $l = 3.6\,V/S$, may be based on the local computational control volume [83] or in a global manner, taking the mean beam length for the whole domain. In the following these two models will be referred to as GNBl and GNBg respectively.

2.5 GWB

The Grey-Wide-Band (GWB) model considers that the spectrum can be divided into 6 bands and in each one a Planck-mean absorption coefficient is considered. This model is implemented in the CFD code Fire Dynamic Simulator (FDS) [99]. For a mixture composed of CO_2, H_2O and soot this model consists in solving the RTE on each wide band:

$$\begin{gathered}\frac{dI_j}{ds} = \kappa_{Pj}\left[I_{bj}(T) - I_j\right] \qquad j = 1{,}6 \\ I = \sum_{j=1}^{6} I_j\end{gathered} \tag{28}$$

As in FDS, the Planck-mean absorption coefficient of each wide band, κ_{Pj}, is computed from the RADCAL database [51]:

$$\kappa_{Pj} = \int_{\nu_{\min,j}}^{\nu_{\max,j}} \kappa_\nu I_{b\nu}\, d\nu \Bigg/ \int_{\nu_{\min,j}}^{\nu_{\max,j}} I_{b\nu}\, d\nu \tag{29}$$

Zheng *et al.* [168] and Coelho [18] computed spectral radiative intensities in Sandia's D flame by using the SNB model. Zheng *et al.* determined the transmissivities from the RADCAL database whereas Coelho used the database of Soufiani and Taine [146]. Both predictions were in close agreement suggesting that gas radiative properties determined from both databases are consistent. As a consequence the use of these different databases to compute radiative properties should not be a great source of discrepancies. In addition the part of the spectrum considered in RADCAL has been restricted to be consistent with that of the database of Soufiani and Taine [146].

In FDS a grey formulation of this model is also implemented [99]. This radiative model was used for the calibration of new soot models based on the concept of the smoke point [7,74]. In this case the absorption coefficient is computed as $\kappa = \min(\kappa_e, \kappa_p)$, where κ_e is an effective absorption

coefficient and κ_p the Planck-mean absorption coefficient. κ_e is determined to match the total radiative intensity leaving a uniform medium of path length l bounded by black walls (at 0 K), this intensity being computed with the SNB model from RADCAL as:

$$I(l) = \frac{\sigma}{\pi}\left[\left(1-\exp\left(-\kappa_e l\right)\right)T^4 + \exp\left(-\kappa_e l\right)T_w^4\right] \tag{30}$$

Determining this path length l is a point that depends usually on the problem considered: for computation based on the mixture fraction, l is taken as 20% of the mean beam length for the whole domain whereas for computations based on finite reaction rates l is taken as the mean path length of the control volume considered [99]. These two considerations are tested in this study, denoting them as FDSgg and FDSgl respectively. In the case of considering the grey formulation of this model for diffusion flames (in the chapter 4), this path length is taken as $l = 2r_f = 8.13\left(D_\infty^2 l_f / g\right)^{1/4}$, where r_f, D_∞, l_f and g are the characteristic radius of the flame, the diffusion coefficient, the flame height and the acceleration of gravity, respectively. This model is denoted as GWBg hereafter.

2.6 WSGG

The Weighted-Sum-of-Gray-Gases (WSGG) is a model which is based on expressing the total gas emissivity as a weighted sum of grey gas emissivities. In this method the non-grey gas is replaced by a number of grey gases, for which the heat transfer rates are calculated independently by solving the RTE with weighted emissive powers for each of the grey gases. The total heat flux is then found by adding the fluxes of all grey gases. The emission weighted factors, $a_j(T)$, and the absorption coefficients, $\kappa_{j,}$ for the *j*-th grey gas were determined from the best fit of the total emissivity with the constraint that the a_j must sum to 1. From a more general point of view the WSGG can be applied as a non-grey gas model [110], solving the RTE for the $N_G = 3$ grey gases plus one $(j = 0)$ for a "clear" gas:

$$\begin{gathered}\frac{dI_j}{ds} = \left(\kappa_j + \kappa_{s,\text{Planck}}\right)\left[a_j(T)I_b(T) - I_j\right] \qquad j = 0, N_G \\ I = \sum_{j=0}^{N_G} I_j\end{gathered} \tag{31}$$

The functional dependence of the weighted factors on temperature is generally fitted by polynomials. The polynomial coefficients as well as the absorption coefficients for each grey gas are tabulated in the literature. For H_2O/ CO_2 mixtures, these coefficients were established for particular ratios of the partial pressure, p_{H_2O}/p_{CO_2}, which limits the application of the method [127]. In this study, the formulation of Smith [140] is considered for a partial pressure ratio of 1 or 2, depending on the stoichiometric ratio for the complete combustion of ethylene or methane in air, respectively. The contribution of soot is added by considering a Planck-mean absorption coefficient ("grey soot").

The WSGG can also be used in its grey formulation, the absorption coefficient being calculated from the total emissivity:

$$\kappa = \ln\left[1-\varepsilon(l)\right]/l$$
$$\varepsilon(l) = \sum_{j=1}^{N_G} a_j(T)\left[1-\exp\left(-\kappa_j l\right)\right] \tag{32}$$

where l can be determined as the mean path length of the control volume considered (referred to hereafter as the WSGGgl model) or as the mean beam length for the whole enclosure (referred to hereafter as the WSGGgg model) [16].

2.7 FSCK and FSSK (and SLW)

The Full Spectrum Correlated-k (FSCK) model, the Full Spectrum Scaled-k (FSSK) model and the Spectral-Line Weighted-Sum-of-Gray-Gases (SLW) model are models that are closely related. They can be viewed as improvements of the WSGG, as mentioned by Modest [109]. The SLW [32,34,35] and the Full Spectrum k-distribution models (FSCK and FSSK) [111] are extensions of the SNBCK model, in which the reordering is carried out into the entire spectrum at once. This allows an important decrease in the number of resolutions of the RTE and then in the computational resources. This task is accomplished by defining a Full Spectrum (FS) Planck function weighted-k-distribution and its cumulative distribution function:

$$f\left(T,\underline{\phi},k\right) = \frac{1}{I_b(T)}\int_0^{\infty} I_{b\nu}(T)\delta\left[k-\kappa_\nu\left(\nu,\underline{\phi}\right)\right]d\nu \tag{33}$$

$$g\left(T,\underline{\phi},k\right) = \int_0^{k} f\left(T,\underline{\phi},k\right)dk \tag{34}$$

Due to the smooth nature of the cumulative function, the integration of the reordered wavenumber can be easily achieved with a simple integration scheme. The major difference in the formulations of the SLW and the Full Spectrum k-distribution models lies in the integration of the k-distributions: the Full Spectrum k-distribution models involve a quadrature scheme whereas the SLW involves a less general trapezoidal scheme.

For homogeneous media, the methods are “exact” as long as the integration of the k-distributions is sufficiently accurate. In the case of non-homogeneous and/or non-isothermal media, as for SNBCK model, the assumption that the absorption coefficient is correlated or scaled is applied, introducing errors in the methods. In addition a reference state of the medium properties must be defined to achieve the derivation of the models. For a synthetic presentation of the methods the FSCK and the FSSK models are presented first, although the SLW model was developed well before.

2.7.1 The FSCK model

The FSCK leads to a reordered RTE in smoothly-varying g_0-space [112]:

$$\frac{dI_g}{ds} = k^*\left(T_0,\underline{\phi},g_0\right)\left[a(T,T_0,g_0)I_b(T)-I_g\right] \tag{35}$$

where

$$a(T,T_0,g_0)=\frac{f(T,\underline{\phi_0},k)}{f(T_0,\underline{\phi_0},k)}=\frac{dg(T,\underline{\phi_0},k)}{dg_0(T_0,\underline{\phi_0},k)} \tag{36}$$

The total intensity is then estimated as:

$$I=\int_0^1 I_g dg_0=\sum_{j=1}^{N_G} w_j I_{gj} \tag{37}$$

with N_G the quadrature points.

2.7.2 The FSSK model

The FSSK model considers that the k-distributions are scaled instead of correlated. This produces that equation **(35)** is now written as [112]:

$$\frac{dI_g}{ds}=k(T_0,\underline{\phi_0},g_0)u(\underline{\phi},\underline{\phi_0})\left[a(T,T_0,g_0)I_b(T)-I_g\right] \tag{38}$$

where $u(\underline{\phi},\underline{\phi_0})$ is the scaling function. In this case the absorption coefficient is evaluated at the reference conditions and multiplied to the scaling function. Equations (**36**) and (**37**) remain unchanged for this formulation.

2.7.3 The SLW model

The derivation of the SLW model can be obtained through the Full Spectrum k-distribution development [109]. Integrating equation (**35**) between $g_{0,i-1}<g_0<g_{0,i}$ leads to:

$$\begin{gathered}\frac{dI_j}{ds}=\bar{k}_j^*(T_0,\underline{\phi})\left[\bar{a}_j(T,\underline{\phi_0})I_b(T)-I_j\right],\quad j=1,N_G \\ I=\sum_j^{N_G} I_j\end{gathered} \tag{39}$$

where

$$I_j=\int_{g_{j-1}}^{g_j} I_g dg \tag{40}$$

$$\bar{a}_j=g_j(T,\underline{\phi_0},k)-g_{j-1}(T,\underline{\phi_0},k) \tag{41}$$

The integration follows the procedure proposed by Denison and Webb [32,34]. The variable absorption coefficient $k^*\left(T_0,\underline{\phi},g_0\right)$ from equation (**35**) is replaced by a single constant value $\bar{k}_j^*\left(T_0,\underline{\phi}\right)$, which is computed as $\sqrt{k_{j-1}\left(T_0,\underline{\phi}\right)k_j\left(T_0,\underline{\phi}\right)}$. In the present study the number of grey gases, N_G, is taken as equal to 10.

2.7.4 Reference state

The reference state is defined here by a simple volume average for the molar fractions of the gas species and the soot volume fraction, while an emission-weighted temperature is considered as the reference temperature [111]:

$$T_0 = \frac{\int_V T\left[4\sigma\kappa_P\left(\underline{\phi}\right)T^4\right]dV + \int_A T\left[\frac{\epsilon\sigma T^4}{\pi}\right]dA}{\int_V \left[4\sigma\kappa_P\left(\underline{\phi}\right)T^4\right]dV + \int_A \left[\frac{\epsilon\sigma T^4}{\pi}\right]dA} \tag{42}$$

In this last equation the effects of the boundary conditions are disregarded based on its low temperature, keeping only the volume integrals.

2.7.5 Assembly of the FS k-distributions

The Full Spectrum k-distributions can be computed in three different ways: i) from a high accuracy spectroscopic database such as HITRAN, HITEMP or CDSD-1000 [111]; ii) from NB databases [114]; iii) from engineering correlations [33,36,37,113,115]. In this study the Full Spectrum k-distributions were assembled from the 367 and 43 NB databases of Soufiani and Taine [146] in order to make direct comparisons with the SNB and SNBCK models.

The assembly scheme chosen in this study is the one proposed by Modest and Riazzi [114]. This scheme forms the Full Spectrum g-function, $g\left(T,\underline{\phi},k\right)$, combining the Narrow Band g-functions, $g_j\left(\underline{\phi},k\right)$, using the following relation:

$$g\left(T,\underline{\phi},k\right) = \sum_{j\in[all\ NBs]} \frac{I_{bj}(T)}{I_b(T)} g_j\left(\underline{\phi},k\right) \tag{43}$$

where

$$I_{bj}(T) = \int_{\Delta\nu_j} I_{b\nu}(T)d\nu \approx I_{b\nu_j}(T)\Delta\nu_j \tag{44}$$

2.7.6 MFS database

Following a procedure similar to the one previously done to the SNBCK model, a Mixed Full Spectrum (MFS) database was pre-generated in order to speed up the calculations. With this procedure the mixing and assembly of the k-distributions can be replaced by only interpolations. This database was generated considering the already calculated MNB database, applying the assembly process for 23 emissive temperatures between 300 and 2500 K (every 100 K). This temperature is called emissive because it only interacts in I_{bj} and in the Planck function, being independent of the gas temperatures (see equation (**43**)). The interpolation between the emissive temperatures is carried out considering a spline interpolation with 4 points (the closest tabulated values around the desired value). By using this database the soot particles can only be considered as grey. This drawback is assessed in this study in order to estimate its impact.

2.8 Planck and OTA

These two grey models are widely used as first approximation to estimate the divergence of the radiative flux. The Planck model considers a Planck-mean absorption coefficient. In this study the absorption coefficients of the combustion gases are evaluated from the correlations given by Zhang and Modest [164]. For the soot absorption coefficient equation **(7)** was used.

The Optically Thin Approximation (OTA) neglects the gas and soot reabsorption, assuming that the medium is optically thin. This indicates that no RTE is solved, making this the fastest model considered in this study. The mean absorption coefficients are computed as described for the Planck model.

2.9 RTE solvers and numerical methods

The Ray Tracing method is used for solving the RTE when the SNB model is used. The domain, in the 1-D cases, or the centreline of the domain, in the 2-D axisymmetric cases, is discretized. In the same way the angular space associated to each evaluation point is divided into control angles. For a given spatial point and a given angular direction, the radiative intensity is computed in two steps: first a line of sight is followed backwards until it intersects a boundary of the numerical domain. From this intersection the RTE, in terms of transmissivity, is solved in the forward direction until the point of interest is reached. This procedure is repeated for each angular direction and each spatial point of interest. The radiative source term at the point considered is calculated from the divergence of the radiative heat flux.

For the other radiative property models the RTE is solved in terms of the absorption coefficient using a Finite Volume Method (FVM). The exponential scheme proposed by Raithby and Chui [131] is used for 1-D calculations, while a first-order UPWIND spatial discretization scheme is used for the 2-D cases. For these cases the special mapping developed by Chui *et al*. for axisymmetric configurations [15] is also considered.

3 Assessment of the radiative property models in non-grey sooting media

In this chapter two series of comparisons are carried out to assess the different radiative property models presented in the previous chapter. The first set considers one-dimensional parallel-plate geometries while the second considers two-dimensional axisymmetric enclosures. The radiative participating species considered in both series are water vapour, carbon dioxide and soot. For all cases the reference solution was calculated considering the SNB model and the Ray Tracing method. This model is normally considered as reference solution in absence of LBL results [17,50]. All other models are resolved with the Finite Volume Method (FVM).

Between the different comparisons carried out in this chapter, different soot loadings are considered in order to see its impact on the radiative heat transfer. For the particular case of the SNBCK model it is also considered different number of bands, different mixing schemes and different number of quadrature points for the integration of the k-distributions. For the case of the FSCK model the number of quadrature points is also tested. Beside these models several other radiative property models are tested, some of them in its spectral and grey formulations.

The present work led to the publication in an international journal and in an international conference [27,28].

3.1 One-dimensional parallel-plate geometries

Media confined between two infinitely long parallel plates, separated by a distance of 1m (L) are considered. All the computations are conducted with a uniform grid composed of 300 control volumes and with a uniform angular mesh composed of 50 polar angles.

Two test cases are analysed: in the first homogeneous and isothermal media is considered, while in the second non-homogeneous and non-isothermal media is considered.

3.1.1 Test case 1: Homogeneous isothermal media

This test involves a hot medium comprising 10% CO_2, 20% H_2O and 70% N_2 at 1000K and at 1 atm. The walls are assumed to be black and cold (0K). Three different soot volume fractions of 10^{-8}, 10^{-7} and 10^{-6} are considered, covering a large range of soot loadings. In the following, the terms low ($f_v=10^{-8}$), high ($f_v=10^{-6}$) and moderate ($f_v=10^{-7}$) soot loadings will be used to characterize configurations where gas radiation dominates, where soot radiation prevails and where the contributions of gas and soot are comparable, respectively.

In order to quantify the difference obtained between the different radiative property models, relative errors are calculated following the relation:

$$RE_{i,model} = \frac{\varphi_{i,model} - \varphi_{i,ref}}{\varphi_{i,ref}} \times 100 \quad (45)$$

where φ_i represents the output data of the radiative model considered at every point *i* of the domain. Mean and maximum relative errors of the divergence of the radiative flux are summarized in Table 3.1. For this comparison the solutions calculated with the SNB model resolved via the Ray Tracing method are considered as reference (RT/SNB). This table also summarizes the ratio between the CPU time of the current model and the FVM/correlated SNBCK 367 (SNBCK model with the correlated method for the treatment of gases and 367 Narrow Bands). The FVM/correlated SNBCK 367 model was preferred to the RT/SNB to quantify computational efficiency since the RT method is not generally of practical interest for CFD applications. To facilitate the interpretation of Table 3.1, maximum and mean errors greater than 10% and 5% are shaded. This choice is somewhat arbitrary but serves to sort those models which do not perform well across a wide range of conditions.

As expected Table 3.1 shows that the predictions obtained with the correlated SNBCK 367 are very accurate, with maximum discrepancies lower than 2%. The first important result concerns the evaluation of the mixing models. Table 3.1 shows that these models lead to computational savings in the range of 30-40% as compared to the correlated approach. This table also shows that all the mixing models considered are very accurate. Comparisons involving the 367 NB database demonstrate that the Modest and Riazzi mixing model (SNBCK 367 M&R) [114] provides the best accuracy with maximum and mean deviations close to those obtained with the correlated SNBCK 367. The second important result involves that relatively small errors are induced by considering the 43 NB database instead of the 367 NB database. The GNB model, which is the most efficient NB model considered in this study (reduction in CPU time by a factor of 8.0) is far from having the same quality of predictions as the other NB models. Both versions of this model, i.e. GNBl and GNBg, provide poor predictions at low and moderate soot loadings because of the crude assumption of grey gas on each band. Similar conclusions were drawn by Goutiere *et al*. [50] from benchmarks involving gas mixtures without soot. Although its accuracy improves greatly as the soot volume fraction increases the results show that the GNB model is not a good candidate for practical situations. It is relatively demanding from a computational point of view and leads to erroneous predictions when soot radiation does not prevail.

Figure 3.1 shows the distributions of the radiative source term for both the reference solution and the Grey Models. These models are the most computationally efficient but are also the less accurate (see Table 3.1). The WSGGgl and the FDSgl models, which take l as the mean effective path length of the control volume under consideration, widely overestimate the radiative contribution of gases. This leads to very poor predictions. If the determination of l is based on the mean length for the whole enclosure (WSGGgg and FDSgg) the predictions are improved (see Table 3.1). However, very large discrepancies are still observed. At low and moderate soot loadings the WSGGgg and the FDSgg models predict flatter profiles than the reference solution, failing to reproduce the effects of the side walls. Figure 3.1 shows that this behaviour is improved for $f_v=10^{-6}$, leading to a better qualitative agreement with the reference solution. This simple test case shows that, although computationally fast, the use of the grey approximation should be avoided in practical applications even when soot concentrations are significant. The grey models will not be further investigated in this chapter.

Table 3.1. Relative error estimations on the radiative source term for test case 1. The RT/SNB model is used as reference. The first column represents the ratio between the CPU time of the current model and the correlated SNBCK with 367 narrow bands. Maximum and mean relative errors greater than 10% and 5% are shaded.

Kind of model	Model	CPU Ratio	Relative Error (%) Test case 1 $f_v=10^{-8}$ Max	$f_v=10^{-8}$ Mean	$f_v=10^{-7}$ Max	$f_v=10^{-7}$ Mean	$f_v=10^{-6}$ Max	$f_v=10^{-6}$ Mean
NB Models	SNBCK 367 Correlated	1	0.71	0.26	0.83	0.14	1.96	0.26
	SNBCK 367 M&R	1/1.4	1.10	0.30	1.33	0.27	2.26	0.34
	SNBCK 367 Superposition	1/1.6	1.90	0.78	2.05	0.53	2.62	0.52
	SNBCK 367 Multiplication	1/1.6	2.93	2.21	2.77	1.17	3.02	0.66
	SNBCK 367 Uncorrelated	1/1.5	1.88	1.43	1.38	0.78	2.16	0.38
	SNBCK 43 Correlated	1/5.0	4.52	1.95	3.15	1.17	2.65	0.47
	SNBCK 43 M&R	1/7.0	3.92	1.72	2.66	1.06	3.05	0.47
	SNBCK 43 Superposition	1/7.3	3.05	2.05	2.94	1.27	3.21	0.46
	SNBCK 43 Multiplication	1/7.5	3.87	0.54	3.83	0.27	3.67	0.47
	SNBCK 43 Uncorrelated	1/7.1	2.52	0.73	2.61	0.36	3.02	0.29
	GNBl	1/8.0	41.52	34.49	27.90	19.80	11.34	5.57
	GNBg	1/8.0	56.67	24.54	51.39	16.89	30.84	9.38
WB Model	GWB	1/210	80.50	74.22	52.26	41.00	22.11	9.02
Grey Models	FDSgl	1/690	243.05	149.77	174.00	79.80	63.48	37.60
	FDSgg	1/690	153.57	110.60	79.10	61.00	28.39	14.07
	WSGGgl	1/700	442.18	133.39	362.00	111.00	174.32	80.46
	WSGGgg	1/700	100.27	68.84	58.00	37.77	35.64	16.16
Global Models	FSCK M&R	1/160	1.30	0.69	0.66	0.46	1.34	0.29
	FSCK Multiplication	1/160	3.71	2.52	13.00	11.30	10.79	4.22
	SLW M&R	1/160	1.26	0.42	0.85	0.67	2.26	1.57
	WSGG	1/255	10.68	4.00	9.05	1.68	5.12	3.82

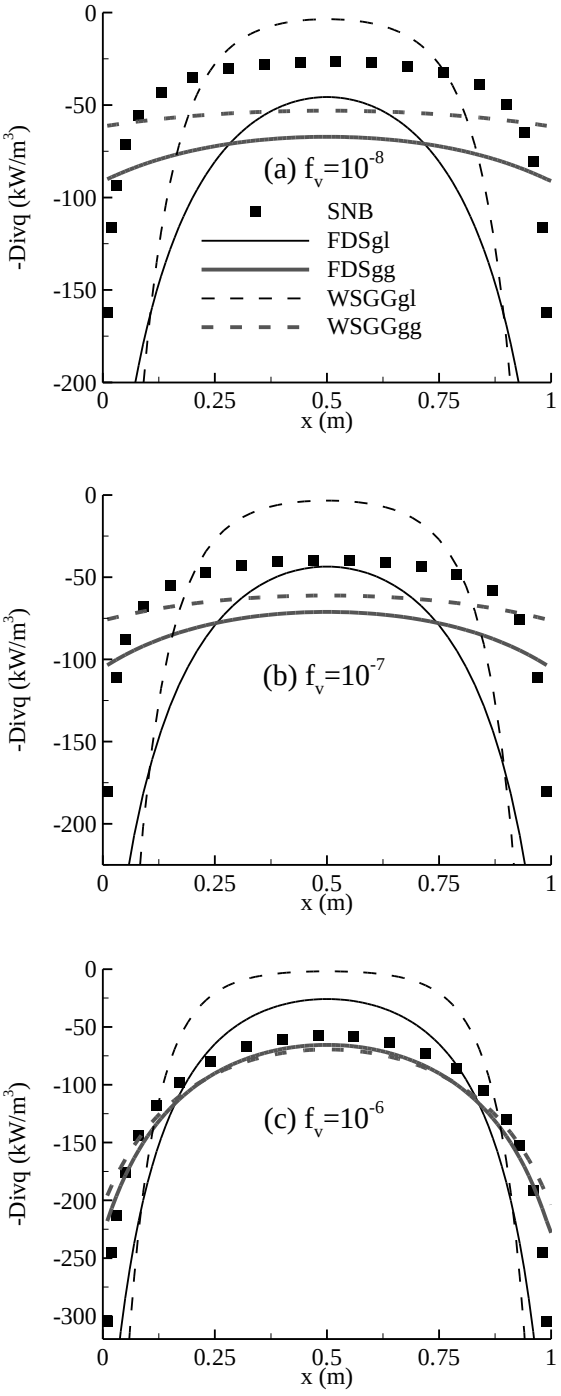

Figure 3.1. Predicted distributions of radiative source term using the RT/SNB model and Grey Models for test case 1: a) $f_v=10^{-8}$, b) $f_v=10^{-7}$ and c) $f_v=10^{-6}$.

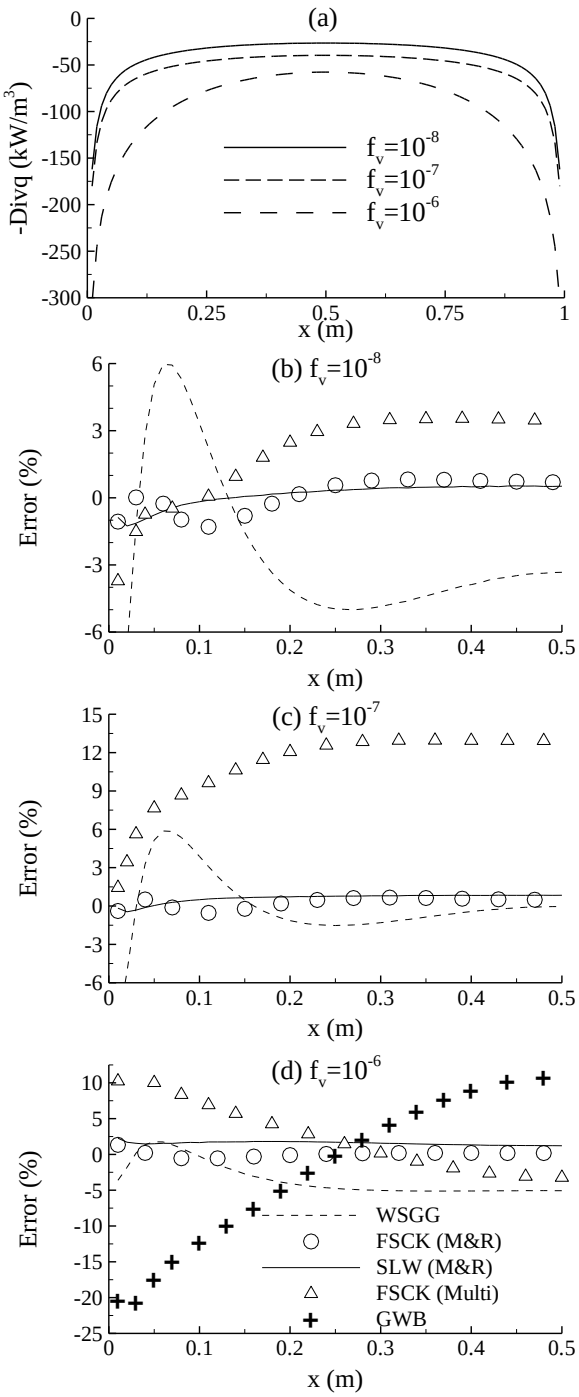

Figure 3.2. Test case 1: a) Predicted distributions of the radiative source term using the RT/SNB model. Relative errors for the GWB and Global Models for b) $f_v=10^{-8}$, c) $f_v=10^{-7}$ and d) $f_v=10^{-6}$. Relative errors concerning the GWB are not visible in diagrams b and c because they are beyond the limit of the graphics.

Figure 3.2 shows the relative error distributions for the Global Models and for the GWB model. The non-grey formulation of the WSGG is very efficient from a computational point of view and yields considerably improved predictions as compared to the Grey Models (see Table 3.1). Computed profiles using the WSGG model are rather satisfactory with a maximum discrepancy of the order of 10%. The GWB model also provides improved predictions as compared to the Grey Models but the solutions are far less accurate than those obtained with the WSGG. Erroneous predictions are still observed at low and moderate soot loadings because of the crude assumption of grey gas on each wide band. At high soot loadings a better agreement is obtained with maximum discrepancies of 22% near the walls (see Table 3.1 and Figure 3.2d).

The use of the Modest and Riazzi mixing model [114], used in the assembly process to form the Full Spectrum (FS) k-distributions from the 367 NB database, leads to accurate results for both the FSCK and the SLW. The maximum and mean discrepancies are comparable to those obtained with the correlated SNBCK 367 model with a reduction in CPU time by a factor of 160. The results obtained with the FSCK are generally slightly more accurate than those obtained with the SLW due to a more efficient integration of the FS k-distributions. The FSCK model was also run with FS k-distributions assembled with the multiplication mixing scheme. This means to carry out the mixing scheme of Solovjov and Webb [144] at a Narrow Band level for the gases, followed by the assembly process of the FS k-distributions and finally applying the mixing scheme at a Full Spectrum level for considering the soot. The results show that this mixing model is less accurate than that of Modest and Riazzi (see Figure 3.2 and Table 3.1). The multiplication mixing scheme is based on the assumption that the absorption coefficients of each species are statistically independent random variables [144]. This assumption is consistent for gaseous species but is less appropriate for the soot absorption coefficient [109]. At low soot loading gas radiation dominates, explaining the good accuracy observed. At moderate soot loading the discrepancies become relatively large with maximum and mean values of 13.0 and 11.3%. Predictions are improved at high soot loadings (maximum and mean deviations of 10.79 and 4.22%) as a consequence of the fact that soot k-distribution dominates the mixture in this case.

3.1.2 Test case 2: non-homogeneous non-isothermal media

This test considers a configuration previously studied by Bressloff [9] and by Solovjov and Webb [145]. The walls are assumed to be black. Temperature and gas species have the following parabolic distributions:

$$\begin{aligned} T(x) &= 800 + 4000x(L-x) \\ X_{CO_2}(x) &= 0.06 + 0.4x(L-x) \\ X_{H_2O}(x) &= 2X_{CO_2} \end{aligned} \tag{46}$$

Two parabolic distributions for soot volume fraction are also considered:

$$\begin{aligned} &\text{Configuration A: } f_S(x) = [40x(L-x)+6] \times 10^{-7} \\ &\text{Configuration B: } f_S(x) = [40x(L-x)+6] \times 10^{-8} \end{aligned} \tag{47}$$

Configurations A and B reach maximum soot volume fractions of 1.6×10^{-6} and 1.6×10^{-7} at $x = 0.5\ m$, respectively.

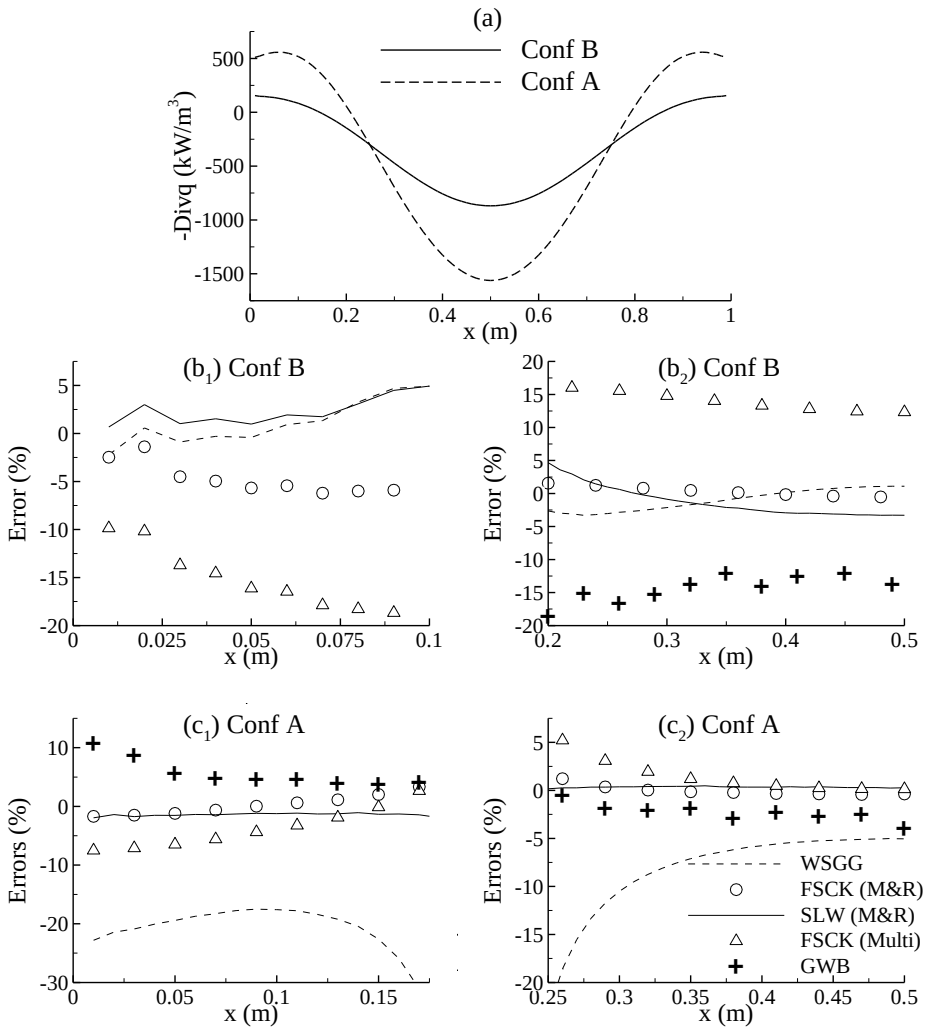

Figure 3.3. Test case 2: a) Predicted distributions of the radiative source term using the RT/SNB model. Relative errors for the GWB and Global Models for b) Configuration B and c) Configuration A. The index 1 is associated with the vicinity of the west wall (0 < x < 0.18m) while the index 2 with the vicinity of the centre of the domain (0.25m < *x* < 0.5m). For diagram b_1, the interval of *x* is restricted to 0 < *x* < 0.1m since the radiative source is insignificant for 0.1m < *z* < 0.18m. Abbreviations M&R and Multi denotes the Modest & Riazzi and the Multiplication mixing schemes respectively.

Figure 3.3 shows the radiative source term distributions for the SNB model and the relative errors for the Global Models and for the GWB model for both configurations. Relative errors are summarized in Table 3.2. From this figure and table can be observed that the conclusions established for the models in case 1 remain unaltered:

- The correlated SNBCK 367 model produces the most accurate solutions.
- Comparisons involving the 367 narrow band (NB) database confirm that the Modest and Riazzi mixing scheme provides the most accurate NB k-distributions for the gas mixture.
- The SNBCK solutions achieved with the 43 NB database are consistent with those obtained with the 367 NB database.
- The GWB model is far from having the same quality of predictions as the other band models. At a moderate soot volume fraction (Conf. B) it leads to large errors with mean and

maximum deviations larger than 20% and 70% respectively. At high soot loadings it provides a rather acceptable solution despite discrepancies of the order of 11% near the walls (see Figure 3.3c_1).

- The FSCK and SLW, coupled with FS k-distributions mixed and assembled from a NB database by using the Modest and Riazzi schemes, yield a good agreement with the reference solutions. The assumption of a correlated (or scaled) absorption coefficient, which is introduced for both NB and FS k-distributions in the case of a non-homogeneous/non-isothermal medium, is less restrictive on a NB basis than on a FS basis. This explains the relative increase in errors between the correlated SNBCK 367 model and the FSCK and SLW models as compared to case 1 (see Table 3.1 and Table 3.2).

Figure 3.3 also shows that solutions of the WSGG model are rather satisfactory with the exception of the region near the walls at relatively high soot loadings (Conf. A), where discrepancies are found to be as large as 40%.

Table 3.2. Error estimations on the radiative source term for test case 2. The SNB model is used as reference. Values where $\left|\vec{\nabla}\cdot\vec{q}\right|_{SNB,i} < 0.1 \times \left|\vec{\nabla}\cdot\vec{q}\right|_{SNB,max}$ are excluded from the error analysis. Maximum and mean errors greater than 10% and 5% are shaded.

Kind of model	Model	Relative Error (%)			
		Conf. B		Conf. A	
		Max	Mean	Max	Mean
NB Models	SNBCK 367 Correlated	1.83	0.46	0.46	0.13
	SNBCK 367 M&R	2.47	0.61	0.58	0.15
	SNBCK 367 Superposition	4.31	1.51	0.48	0.20
	SNBCK 367 Multiplication	6.17	2.15	0.79	0.28
	SNBCK 367 Uncorrelated	3.82	1.14	0.82	0.18
	SNBCK 43 Correlated	2.74	0.43	0.50	0.11
	SNBCK 43 M&R	1.72	0.40	0.39	0.10
	SNBCK 43 Superposition	2.94	0.69	0.54	0.17
	SNBCK 43 Multiplication	3.23	1.34	0.46	0.18
	SNBCK 43 Uncorrelated	2.35	0.59	0.62	0.11
WB Model	GWB	70.2	23.2	10.99	3.88
Global Models	FSCK M&R	6.14	1.31	3.56	0.84
	FSCK Multiplication	20.00	14.40	11.73	2.98
	SLW M&R	8.33	2.47	1.95	0.75
	WSGG	4.69	1.57	45.93	14.88

3.2 Two-dimensional axisymmetric enclosures

Some radiative property models are selected based on the results of the previous section. The SNBCK model calculated with 43 narrow bands is here coupled with the mixing scheme of Modest and Riazzi [114], this model being referred to as the SNBCK 43 M&R. The FSCK model, using the k-distributions

mixed with the Modest and Riazzi mixing scheme and assembled from the 367 NB database is also selected. The GWB model and the WSGG model are also considered owing to their importance in the modelling of fire and combustion problems. These models are assessed by comparison with the SNB model.

Three different tests are carried out in this section, considering two-dimensional axisymmetric enclosures surrounded by black walls. The first considers a homogeneous and isothermal medium, the second a homogeneous and non-isothermal medium while the last considers a non-homogeneous and non-isothermal medium. For the three cases the temperature, the CO_2 and H_2O molar concentrations fractions and the soot volume fractions are prescribed.

For tests cases 1 and 3 additional bands are added to the radiative calculations to account for the soot radiation near the visible region of the spectrum (between wavelengths 9312.5 – 14285 cm^{-1}), where gas radiation is negligible but soot radiation is still present if the temperature is high enough. This consideration agrees with the solution reported by Coelho *et al*. [17].

For the three cases the RTE is solved by using the FVM. For the tests cases 1 and 3 a uniform grid with 81×60 control volumes is considered, while for test case 2 a non-uniform grid with 38×48 control volumes is used. A uniform angular mesh with 12×16 control angles is considered for the three cases.

3.2.1 Test case 1: homogeneous and isothermal medium

The first case involves an enclosure with a length (*L*) of 3 m and a radius (*R*) of 0.5 m. The volumetric composition of the medium is 20% H_2O, 10% CO_2 and 70% N_2 (molar fractions). The temperatures of the medium and of the walls are 1200K and 300K, respectively. An atmospheric pressure and a soot volume fraction of 10^{-7} are considered.

Figure 3.4 shows the incident heat flux on the boundary wall ($r = R$) and the divergence of the radiative flux along the centreline of the domain calculated with the SNB model, using the Ray Tracing method by Coelho *et al*. [17], and the solution obtained with the SNBCK model considering the correlated method for the treatment of gases and 367 narrow bands (NB). It is important to mention that for a homogeneous and isothermal medium the SNBCK does not introduce any approximation. Since both SNB and SNBCK parameters are taken from the same database, the discrepancies between the two solutions result from the use of different RTE solvers, namely the RT and the FVM. The agreement between the two solutions is satisfactory with mean relative errors lower than 1% for both the incident heat flux and the radiative source (see Table 3.3).

For the evaluation of the radiative property models the FVM/correlated SNBCK 367 is considered as the reference solution (instead of the RT/SNB) in order to avoid the introduction of errors related to the RTE solver. The mean and maximum relative errors for each model for the incident heat flux and for the divergence of the radiative flux along the centreline are reported in Table 3.3. This table summarizes also the ratio of CPU time between the reference solution and the current model in order to quantify the reduction in computational requirements.

Table 3.3 shows clearly that the main drawback of the SNBCK for gas mixture, i.e. its computational efficiency, can be circumvented by using the SNBCK with only 43 narrow bands, mixed with the

Modest and Riazzi scheme. This provides accurate solutions (maximum relative error of 1.72%, see also Figure 3.5) with a reduction in CPU time by a factor of about 30.

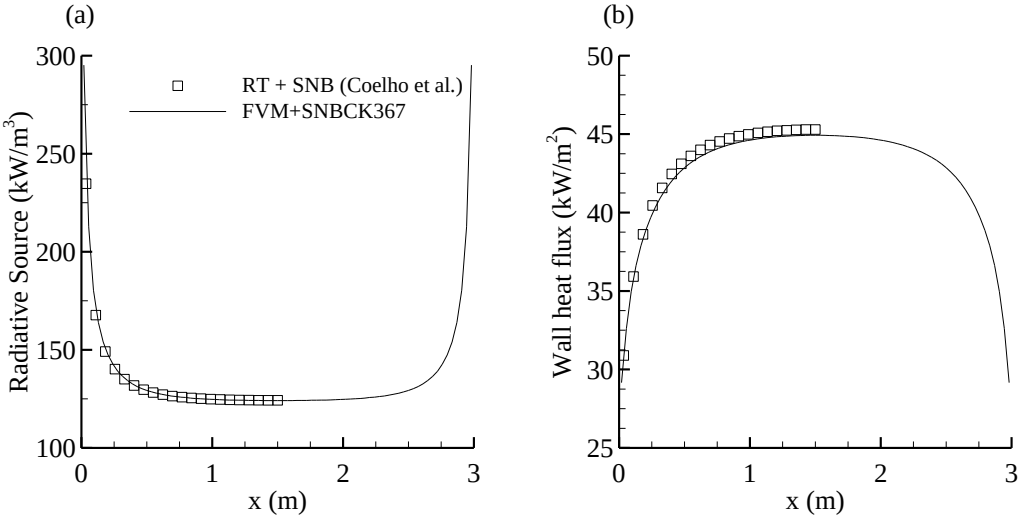

Figure 3.4. Comparison between the RT/SNB and the FVM/correlated SNBCK 367 narrow bands for test case 1: (a) Divergence of the radiative heat flux along the centreline ($r = 0$), and (b) incident heat flux on the wall ($r = R$). RT/SNB results from [17].

Table 3.3. Error estimations for test case 1. The SNBCK 367 Correlated is compared to RT/SNB, while the rest of the models are compared to SNBCK 367 Correlated. Computational requirements, expressed as the CPU time ratio, are compared to the SNBCK 367 Correlated solution. Maximum and mean errors greater than 10% and 5% are shaded.

Model	Relative Error (%)				$\frac{t_{CPU,model}}{t_{CPU,ref}}$
	Divergence of the radiative flux		Incident heat flux on the wall (r = R)		
	Max	Mean	Max	Mean	
SNBCK 367 Correlated	9.21	0.77	1.23	0.83	--
SNBCK 43 M&R	1.72	0.33	1.06	0.97	1/29.9
GWB	42.03	39.48	38.15	37.83	1/631.1
WSGG	16.10	15.50	5.87	5.42	1/677.1
FSCK M&R	1.27	1.02	0.29	0.25	1/619.0

The relative errors produced by the GWB, the WSGG and the FSCK are presented in Table 3.3. All three models present an important gain in CPU time, but the precision widely varies. The GWB present the worst result between the three, with mean relative errors higher than 37%. The WSGG, even though it provides results 677 times faster than the reference solution, it does not yield to really accurate solutions, with a mean underestimation of the divergence of the radiative flux of more than 15% (see Figure 3.5). The FSCK is the best compromise in terms of accuracy and

computational efficiency. This model, coupled to the Full Spectrum k-distribution assembled from the same narrow band database as the SNBCK models, leads to solutions with a maximum relative error lower than 1.3% in the case of a homogeneous and isothermal medium.

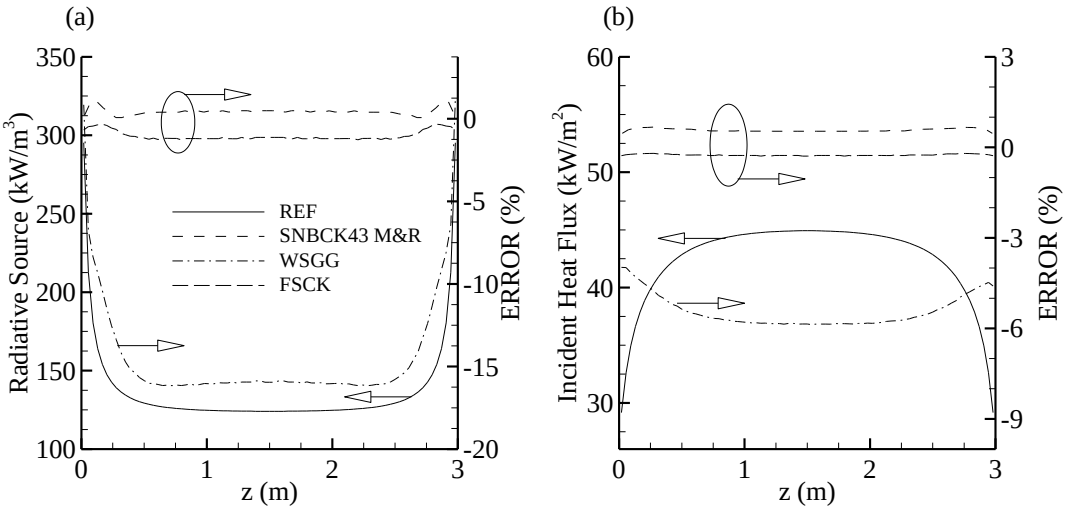

Figure 3.5. Comparisons for test case 1: (a) Relative errors on the divergence of the radiative flux (radiative source) along the centreline ($r = 0$), and (b) on the incident heat flux at $r = R$. Reference: SNBCK 367 correlated. GWB solution is not presented because it is out of range.

3.2.2 Test case 2: homogeneous and non-isotherm

The numerical configuration of this test is inspired from the works of Liu [83]. A domain 2 m in radius (*R*) and 4 m in height with black walls at 300 K is modelled. The concentrations of CO_2 and H_2O in the medium are set to 10% and 20% by mole fraction respectively. The temperature field is prescribed by:

$$T(r,z) = (T_c(z) - T_e)\left[1 - 3\left(\frac{r}{R_1}\right)^2 + 2\left(\frac{r}{R_1}\right)^3\right] + T_e$$
$$T(r,z) = T_e \quad \text{for} \quad r > R_1 \tag{48}$$

where R_1 is taken as being equal to 1 m, T_c is the centreline temperature and T_e the temperature at $z = 4\ m$. The centreline temperature varies throughout the enclosure: at $z = 0\ m$, T_c is 400 K, rising linearly to 1800 K at $z = 0.375\ m$; then T_c decreases linearly from $z = 0.375$ to $4\ m$, at which point reaches 800 K (T_e). Two soot volume fractions of 10^{-6} (configuration A) and 10^{-7} (configuration B) are considered. In configuration A the soot radiation dominates, whereas in configuration B the contribution of soot and gas are comparable.

The radiative source term along the axis of the domain and the incident heat flux at the wall ($r = R$) are presented in Figure 3.6 and Figure 3.7 respectively. The corresponding relative errors and CPU ratios are summarized in Table 3.4. The SNB model is used as reference, calculated through a Ray Tracing method especially implemented for this problem.

Results show that the GWB leads to large discrepancies for both tested quantities in configuration B. For configuration A the predicted distribution of the radiative source term becomes acceptable with

discrepancies of less than 5% in the region located between the peak and the north wall ($z = 4m$). Nevertheless, maximum errors of about 34% and 9% are still observed on the radiative source term near the south wall ($z = 0$) (see Figure 3.6b$_1$) and on the wall heat flux (see Figure 3.7b and Table 3.4) respectively.

The WSGG is computationally more efficient than the GWB and yields much more satisfactory predictions for f_v=10^{-7} (Conf. B). In this configuration relative errors on the radiative source term are within 7% in the region located between the peak and the north wall (see Figure 3.6a$_2$), whereas larger discrepancies of about 15% are observed in the vicinity of the south wall (see Figure 3.6a$_1$). The incident wall heat flux is also well predicted with maximum discrepancies of less than 3.5% (see Figure 3.7a and Table 3.4). For configuration A the agreement on the divergence of the radiative flux is globally satisfactory, with the exception of the zone near the south wall where the relative error reaches a local value of about 40% (see Figure 3.6b$_1$). Figure 3.7b and Table 3.4 show that the incident heat flux at the wall is not really well predicted in this configuration.

The FSCK model is slower than the WSGG and the GWB models with an increase in CPU time by factors of 1.5 and 1.2 respectively. Nevertheless, it provides much more accurate solutions with maximum discrepancies lower than 4.2%, with the exception of the radiative source term in configuration B. In this case Figure 3.6a$_1$ shows that the largest discrepancies (about 9%) are localized in the region of $0.2\ m < z < 0.4\ m$, the overall agreement being excellent with a mean deviation of about 2%. The SNBCK model calculated with 43 bands and the mixing scheme of Modest and Riazzi (MRSNBCK43) yields the most accurate solutions for both the radiative source and the wall heat flux in the two configurations. A substantial gain in CPU time is observed with a reduction factor of 25 as compared to the correlated SNBCK 367.

Table 3.4. Error estimations on the radiative source term along the centreline and on the incident heat flux at the wall for test case 2. The SNB model is used as reference. Values where $\left|\vec{\nabla}\cdot\vec{q}\right|_{\mathrm{SNB,i}} < 0.1 \times \left|\vec{\nabla}\cdot\vec{q}\right|_{\mathrm{SNB,max}}$ are excluded from the error analysis. The first column represents the CPU time ratio between the current model and the SNBCK 367 correlated. Maximum and mean errors greater than 10% and 5% are shaded.

		Relative Error (%)							
		Conf. B (f_v=10^{-7})				Conf. A (f_v=10^{-6})			
Model	CPU Ratio	Source Term		Wall Flux		Source Term		Wall Flux	
		max	mean	max	mean	max	mean	max	mean
SNBCK 43 M&R	1/25	1.33	0.66	0.59	0.37	0.75	0.19	0.14	0.06
GWB	1/273	61.22	21.81	37.48	27.77	33.81	6.48	9.02	4.61
WSGG	1/350	14.74	7.71	3.47	2.68	40.63	11.14	8.12	5.78
FSCK	1/235	8.51	2.14	2.00	1.53	4.21	1.40	0.09	0.05

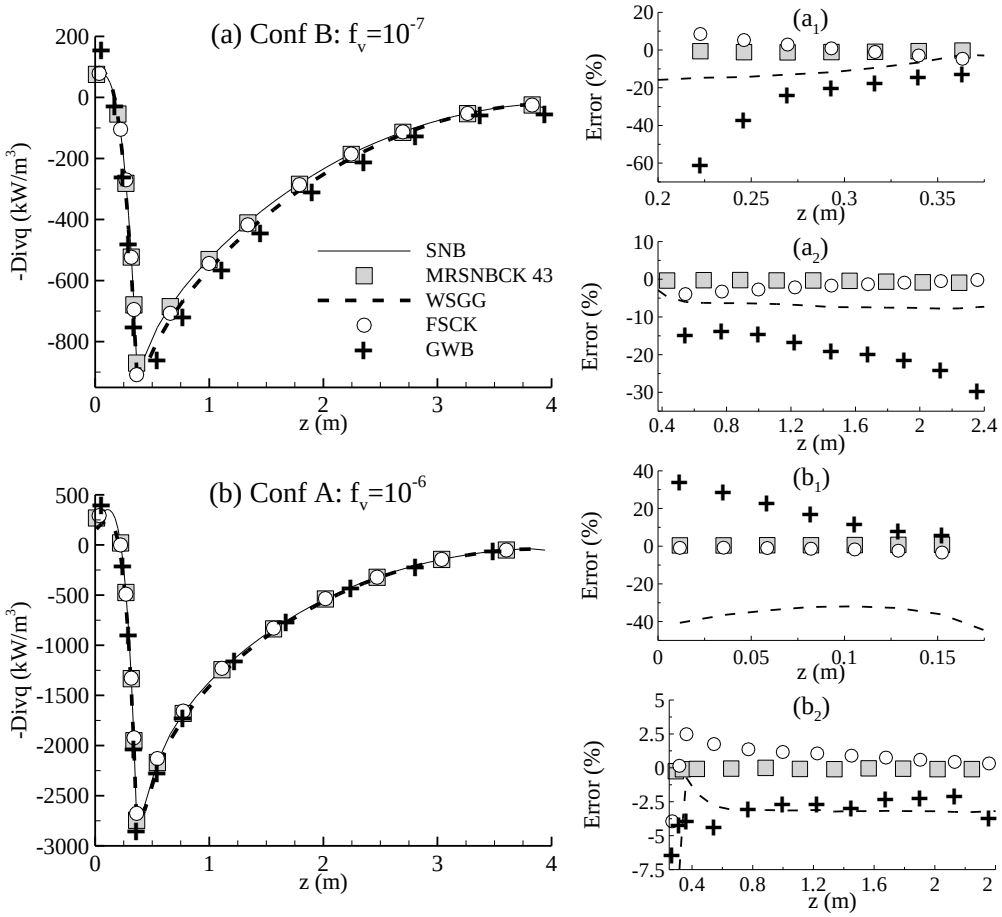

Figure 3.6. Distributions of the radiative source term along the axis for test case 2: (a) Conf. B, and (b) Conf. A. SNB solution is used as reference for the estimation of the relative error. Subindex indicate: (1) for 0.2m<z<0.4m in Conf. B and for 0<z<0.15m in Conf. A and (2) for 0.4m<z<2.4m in Conf. B and for 0.25m<z<2.4m in Conf. A.

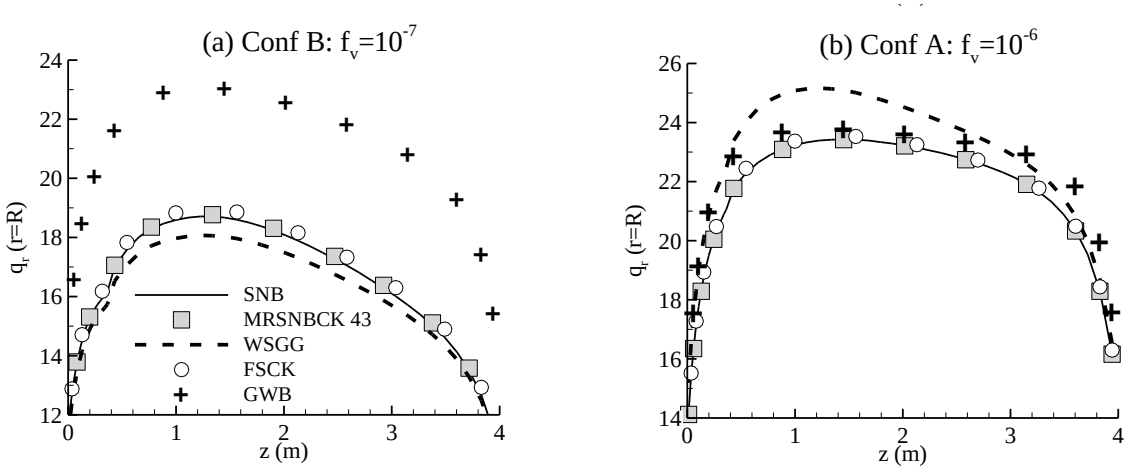

Figure 3.7. Incident heat flux at the wall ($r = R$) for test case 2: (a) Conf. B, and (b) Conf. A.

3.2.3 Test case 3: non-homogeneous and non-isothermal medium

This case considers a non-homogeneous and non-isothermal medium with $L = 1.2\,m$ and $R = 0.3\,m$. The walls are at 800 K except the wall located at $z = L$, which is maintained at 300 K. The distributions of the temperature and of the molar fractions of H_2O and CO_2 are given by:

$$\begin{aligned} T(r,z) &= 800 + 1200(1 - r/R)(z/L) \\ X_{H_2O}(r,z) &= 0.05[1 - 2(z/L - 0.5)^2](2.0 - r/R) \\ X_{CO_2}(r,z) &= 0.04[1 - 3(z/L - 0.5)^2](2.5 - r/R) \\ f_S &= 10^{-7} \end{aligned} \tag{49}$$

Figure 3.8 compares the FVM/correlated SNBCK 367 and the RT/SNB obtained by Coelho *et al*. [17]. The agreement between the two solutions is very satisfactory with mean and maximum relative errors of 0.33% and 1.68% and of 2.26% and 13.6% for the incident heat flux at the wall ($r = R$) and for the divergence of the radiative flux along the centreline, respectively.

As for the test case 1, the FVM/correlated SNBCK 367 is considered as the reference solution in order to assess the gas property models. The error estimations and the gain in computational requirements for each model are listed in Table 3.5.

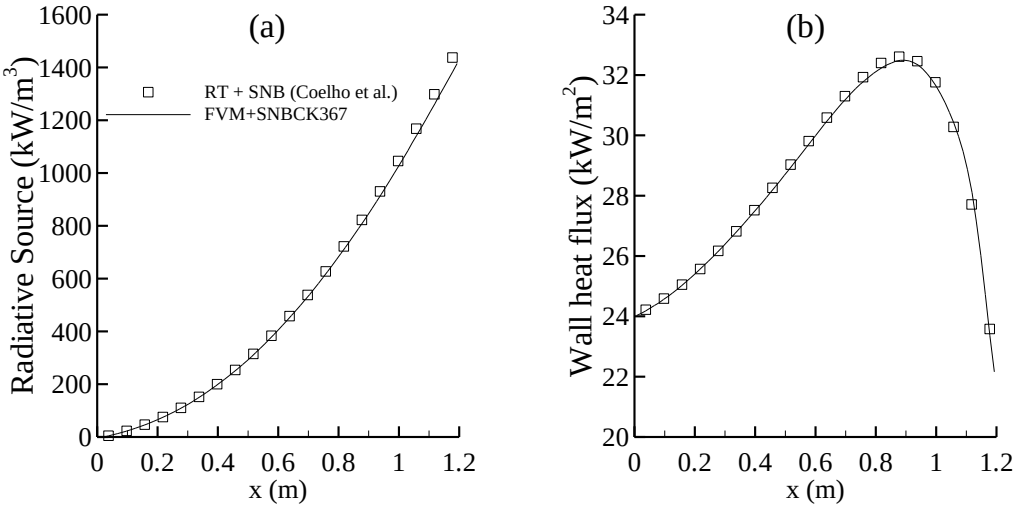

Figure 3.8. Comparison between the RT/SNB and the FVM/correlated SNBCK 367 narrow bands for test case 3: (a) Divergence of the radiative heat flux along the centreline, and (b) incident heat flux at the wall ($r = R$). RT/SNB results from [17].

Reductions in CPU times as well as the accuracy of the different models are in close agreement with those obtained for test cases 1 and 2: the solutions obtained with the 43NB database and mixed with the Modest and Riazzi scheme are in close agreement with the reference (Table 3.5). The GWB model continues to predict poor results, with significant local errors. As mentioned in the preceding chapter, the parameters of the WSGG have been derived for a fixed partial pressure ratio, $p_{H_2O} = 2p_{CO_2}$, however for the present problem the fields of molar fractions of H_2O and CO_2 do not satisfy this condition. As a consequence it is difficult to draw conclusions on the good agreement obtained with this model for both the divergence of the radiative flux and the wall incident heat flux

(see also Table 3.5). The large value of the maximum deviations observed on both emission and absorption terms confirm that this agreement is rather fortuitous. Finally, the FSCK provides accurate solutions with an important gain in the CPU time required.

Table 3.5. Error estimations of the incident wall heat flux (r=R), divergence of the radiative flux, emission and absorption terms for test case 3. The SNBCK367 correlated is compared to RT/SNB, while the rest of the models are compared to SNBCK 367 Correlated. Computational requirements, expressed as the CPU time ratio of several radiative property models, are compared to the SNBCK 367 Correlated solution. Maximum and mean errors greater than 10% and 5% are shaded.

Model	CPU Ratio	Relative Error (%)							
		Incident wall heat flux		Divergence of the radiative flux		Emission term		Absorption term	
		Max	Mean	Max	Mean	Max	Mean	Max	Mean
SNBCK 367 Correlated	--	1.68	0.33	13.6	2.26	--	--	--	--
SNBCK 43 M&R	1/30.2	0.75	0.44	0.77	0.16	0.75	0.40	1.98	0.86
GWB	1/564	37.51	21.08	49.86	13.97	12.1	9.03	28.52	6.57
WSGG	1/598	2.31	1.32	15.5	2.41	41.39	6.72	63.72	10.71
FSCK M&R	1/525	0.94	0.45	7.70	0.51	6.87	2.17	8.73	3.74

3.3 Influence of the number of quadrature points on SNBCK and FSCK predictions

The objective of this section is to optimize the number of quadrature points for the SNBCK and FSCK models in order to obtain the best compromise in terms of accuracy and computational efficiency. Following the conclusions of previous studies, Gauss-Legendre quadrature schemes are used for both methods [84,111]. For the SNBCK model calculated with 43 narrow bands and coupled with the mixing scheme of Modest and Riazzi [114] (SNBCK 43 M&R) a 7-points, 4-points, 2-points and 1-point of quadrature are considered whereas 10-points, 7-points, 5-points and 4-points of quadrature are used for the FSCK. Table 3.6 and Table 3.7 summarize the loss in accuracy and the gain in CPU time for the two one-dimensional cases and test case number 2 of the two-dimensional axisymmetric cases.

For the 2-D axisymmetric test case, the use of the SNBCK 43 M&R model with 4, 2 and 1-point of quadrature allows a decrease in CPU time by factors of 1.8, 3.6 and 6.0 as compared to the 7-point quadrature scheme. Predictions made with this model are not altered by reducing the number of quadrature points until to 4, which is consistent with the observations of Liu *et al.* [84] for gas mixtures without soot. Acceptable results are also obtained with only 2 quadrature point although larger relative errors on the predictions of the radiative source term are observed, especially for the homogeneous/isothermal test case (test case 1, Table 3.6). The use of 1 quadrature point may lead to significant errors. Concerning the FSCK model, results show that accurate predictions can be made by reducing the number of quadrature points until to 7. In this case the number of RTE to solve is reduced to 7 as compared to 4 for the WSGG and 6 for the GWB.

Table 3.6. Influence of the number of Gauss-Legendre quadrature points on the predictions of the Source term for both the SNBCK with 43 bands and the mixing scheme of Modest and Riazzi (SNBCK 43 M&R), and of the FSCK models for both one-dimensional test cases. Errors are estimated by considering the SNB model as reference. The ratios of CPU time are evaluated by considering the SNBCK 43 M&R with 7 quadrature points and the FSCK with 10 quadrature points. Maximum and mean errors greater than 5% and 2.5% are shaded.

		Relative Errors (%)									
		Test case 1						Test case 2			
N_G	CPU Ratio	$f_v=10^{-8}$		$f_v=10^{-7}$		$f_v=10^{-6}$		Conf. B		Conf. A	
		max	mean	max	mean	max	mean	max	mean	max	mean
SNBCK 43 M&R											
7	1/1	3.92	1.72	2.66	1.06	3.05	0.47	1.72	0.40	0.39	0.10
4	1/1.57	4.16	2.31	3.16	1.42	3.34	0.47	1.99	0.34	0.36	0.13
2	1/2.86	13.43	2.67	12.40	2.14	8.54	1.68	5.16	1.19	1.44	0.44
1	1/4.57	35.22	15.46	32.00	10.90	19.80	6.20	15.60	5.39	1.08	0.53
FSCK M&R											
10	1/1	1.30	0.69	0.66	0.46	1.34	0.29	6.14	1.31	3.56	0.84
7	1/1.15	6.26	2.04	5.02	1.66	2.06	1.16	8.39	1.97	4.29	0.99
5	1/1.25	17.26	4.67	14.50	3.34	6.51	1.92	6.26	1.87	12.08	2.32
4	1/1.32	22.33	10.94	18.00	6.88	7.55	3.40	14.80	4.30	4.10	2.21

Table 3.7. Influence of the number of Gauss-Legendre quadrature points on the predictions of both the SNBCK with 43 bands and the mixing scheme of Modest and Riazzi (SNBCK 43 M&R), and of the FSCK models for test case number 2 of the two-dimensional axisymmetric cases. Errors are estimated by considering the SNB model as reference. The ratios of CPU time are evaluated by considering the SNBCK 43 M&R with 7 quadrature points and the FSCK with 10 quadrature points. Maximum and mean errors greater than 5% and 2.5% are shaded.

		Relative Error (%)							
		Conf. B				Conf. A			
N_G	CPU Ratio	Source Term		Wall Flux		Source Term		Wall Flux	
		max	mean	max	mean	max	mean	max	mean
SNBCK 43 M&R									
7	1/1	1.33	0.66	0.59	0.37	0.75	0.19	0.14	0.06
4	1/1.80	1.35	0.74	1.03	0.80	0.65	0.21	0.14	0.02
2	1/3.60	5.87	0.83	0.87	0.50	1.69	0.57	0.65	0.17
1	1/6.00	14.03	2.37	3.57	1.93	4.68	1.85	2.59	0.75
FSCK M&R									
10	1/1	8.51	2.14	2.00	1.53	4.21	1.40	0.09	0.05
7	1/1.11	6.67	2.16	4.20	3.20	2.16	0.42	0.80	0.52
5	1/1.28	10.53	1.69	7.35	6.34	5.76	1.51	1.03	0.26
4	1/1.32	7.37	2.30	6.60	6.22	15.64	5.05	0.98	0.45

3.4 Concluding remarks

A comprehensive comparison was carried out to assess the accuracy and the computational efficiency of several radiative property models in one-dimensional parallel-plate enclosures and two-dimensional axisymmetric enclosures containing prescribed mixtures of CO_2, H_2O and soot. Model results are compared with accurate benchmarks obtained using the RT method together with the SNB model. The following conclusions can be drawn:

- The SNBCK model is recommended if solutions with a high degree of accuracy are required. The correlated SNBCK 367 model is the most accurate model but is very time consuming. Its computational efficiency can be considerably improved without altering the quality of the solutions by using both the 43 NB database and the accurate gas mixing scheme of Modest and Riazzi [114]. If only spectrally integrated quantities are of interest, a 2-point Gauss-Legendre quadrature scheme offers acceptably good accuracy with much less computational effort as compared to the 7-point quadrature scheme.
- Grey Models lead to very poor predictions despite they require low CPU time to run. The use of these models should be avoided if precise results are desired.
- The WSGG and the GWB models improve the predictions of Grey Models. However they cannot be used with confidence over a wide range of soot loadings. The WSGG produces generally rather satisfactory solutions but can lead to significant discrepancies in some situations. The GWB model yields unsatisfactory results at low and moderate soot loadings. As soot radiation prevails, it provides acceptable solutions despite large local discrepancies.
- The FSCK and the SLW, using FS k-distribution generated from an accurate NB database with the mixing scheme of Modest and Riazzi [114], are found to be the best compromise in terms of accuracy and computational efficiency. This mixing scheme is found to be more accurate than the multiplication scheme of Solovjov and Webb [144]. The FSCK is generally slightly more accurate than the SLW, leading to high quality solutions with only 7 Gauss-Legendre quadrature points for the cases investigated.

4 Modelling radiative heat transfer and soot formation in laminar coflow diffusion flames

The main objective of this chapter is to evaluate the capability of simplified soot models to provide reliable predictions over a wide range of conditions and fuels, keeping in mind subsequent applications to turbulent flames.

In order to accomplish this task, laminar coflow diffusion flames are considered. This buoyancy dominated configuration presents several advantages: (i) it allows investigating soot formation in a well-defined configuration, avoiding the complications related to turbulence, (ii) exhaustive experimental studies, including measurements of velocity, temperature, gaseous species and soot characteristics can be found in the literature for a wide range of fuels and conditions, allowing the creation of a benchmark database for soot models.

As mentioned in the introduction, the continuum radiation of soot plays an important role in the radiative loss of flames, affecting the temperature field and consequently the formation/oxidation processes of soot particles themselves. Coupled flow field/combustion/radiative heat transfer calculations are then required, raising the question about the radiative model to be used in order to keep the computational requirement compatible with an exhaustive study. The small dimensions of the laminar coflow diffusion flames considered in the present study suggest that the optically thin approximation (OTA) may be used. However, previous studies have shown that this approximation, valid for weakly sooting methane flames [90], can be deficient in the upper part of moderately sooting ethylene flames [89]. In particular the amount of soot released from the flame in the case of smoking flames can be widely affected by the soot model [89]. As a consequence, before evaluating the soot model, a study involving smoking and non-smoking ethylene flames [101,102,135] is carried out in order to find an adequate radiative model.

The chapter is organized as follow: It begins with a brief description of the soot models used in this study. Only semi-empirical models are considered since more complex models introduce too much computational requirements making them impractical for applications to turbulent flames. Initially the global formulation of the model is presented, indicating its principal equations and concepts. Modifications to this formulation are then presented, considered to improve its generality.

The soot models are followed by a synthetic description of the CFD model in which the soot and the radiation models are implemented. Combustion is modelled considering the Steady Laminar Flamelet (SLF) concept. This means that each portion of the flame front can be considered as a little steady flame, also called flamelet. This kind of model is widely used in coupled flow/combustion CFD codes since all chemical processes can be pre-databased, in what are generally called flamelet libraries. This

allows considering a detailed chemistry without excessive computational costs. Finally, the transport equations resolved by the CFD code and the numerical procedure are presented.

Results are then presented and discussed: the first part is dedicated to the assessment of the radiative models. As mentioned above two laminar ethylene coflow diffusion flames, one non-smoking and the other smoking, are considered. The conclusions drawn from preliminary decoupled radiative calculations, carried out on a flow-field computed with a simple radiative property model, are briefly described. Fully coupled calculations are then carried out in order to assess the impact of the radiative property models in the soot predictions. Finally, the soot model is evaluated by considering the optimal radiative model. Four different fuels are considered, besides the ethylene used in the previous comparisons, testing methane, propane and propylene flames. Two inverse ethylene-air flames are also considered in order to test the capability of the soot model to reproduce a sooting behaviour quite different from that observed in normal coflow diffusion flames.

The present work led to the publication in some international conferences and in an open access journal [29,30].

4.1 Soot models

4.1.1 Brief overview on soot models

Soot is an agglomerated structure formed by particles containing millions of carbon atoms as result of high temperature fuel combustion. It is the main emission of combustion devises, produced by incomplete hydrocarbon combustion under non-ideal local conditions. A great effort has been made in order to understand the processes of soot formation and oxidation, but there are still too many unknowns that need to be addressed. Soot modelling constitutes a challenging problem involving a large set of highly coupled partial differential equations describing physical and chemical processes. This makes the task of modelling soot formation and oxidation extremely complex. To overcome the inherent difficulty of soot modelling different kinds of models have been proposed: empirical models, semi-empirical models and detailed models [62].

Empirical models use correlations of experimental data to predict trends in soot loadings. This kind of model is usually used by engineers in the engine community, adopting empirical correlations of soot production as function of engine operating conditions. As with all correlations, the method is only useful as an extrapolation for conditions close to those under which the original data were first obtained.

Detailed soot models consider full chemistry for the gas-phase, the formation of the soot precursors such as acetylene (C_2H_2) and polycyclic aromatic hydrocarbons (PAH), and a detailed description of soot surface processes. For this kind of model very detailed descriptions of soot physics and chemistry are considered. Various models have been presented in order to mathematically predict the soot particle size distribution function, as for example the method of moments [44], the sectional method [46] and the stochastic method [5]. Detailed models are a promising tool for soot predictions, but they still have some limitations. The complexity of the model itself and the difficulty of adjusting all the parameters of the submodels are some of its drawbacks.

Semi-empirical models are somewhat between these two limits. They solve rate equations for the formation of soot nuclei, soot particle growth and oxidation with more or less simple models that are

calibrated against experimental data. Examples of these models are the Leung *et al.* [77] soot model considering only the first two moments of the soot particle size distribution function and a reduced soot mechanism, the model suggested by Moss *et al.* [116] which relates the soot formation to a specific fuel, or the model proposed by Garo *et al.* [45] which relates the soot formation to an intermediate imaginary species.

The three classes of models have demonstrated success in predicting soot concentrations, however in almost all cases after some adjustment to the model parameters [62].

4.1.2 Lindstedt and co-workers model

The soot model considered in the present study is based on the concepts introduced by Leung *et al*. [77]. This model is based on a simplified reaction mechanism for the inception, growth and combustion of soot particles and was validated in laminar counterflow non-premixed flames. This model or variants of this model [10,40,80,88] were subsequently applied with success to predict the soot volume fraction in both laminar [6,13,53,92] and turbulent configurations [10,71].

Two transport equations need to be resolved, one for the soot number density (N_s), defined as the number of particles per unit mass of mixture, and another for the soot mass fraction (Y_s). The reaction mechanism considered in this model involves nucleation, surface growth, particle coagulation and oxidation. The soot nucleation and surface growth reactions are related to the gas phase by presuming that pyrolysis products, in the present case acetylene and/or benzene, and not the fuel itself, are of primary importance in the soot formation process.

The transport equations for the soot mass fraction and the soot number density are given as:

$$\rho u_r \frac{\partial Y_s}{\partial r} + \rho u_z \frac{\partial Y_s}{\partial z} = -\frac{1}{r}\frac{\partial}{\partial r}\left(r\rho V_{T,r} Y_s\right) - \frac{\partial}{\partial z}\left(\rho V_{T,z} Y_s\right) + S_m \tag{50}$$

$$\rho u_r \frac{\partial N_s}{\partial r} + \rho u_z \frac{\partial N_s}{\partial z} = -\frac{1}{r}\frac{\partial}{\partial r}\left(r\rho V_{T,r} N_s\right) - \frac{\partial}{\partial z}\left(\rho V_{T,z} N_s\right) + S_N \tag{51}$$

where the variables u_r and u_z represent the velocities in the r– and z–directions respectively, ρ represents the mixture density. Quantities $V_{T,r}$ and $V_{T,z}$ are the thermophoretic velocities of soot in the r– and z–directions, and are calculated as [77]:

$$V_{T,i} = -0.55\frac{\mu}{(\rho T)}\frac{\partial T}{\partial x_i}, \qquad x_i = r, z \tag{52}$$

The source term S_m in equation (**50**) accounts for the contribution of soot nucleation, surface growth, coagulation and oxidation. Acetylene ($\mathrm{C_2H_2}$) is assumed to be the main gaseous species involved in the nucleation (r_1) and surface growth (r_2) processes. These reactions and their reaction rates are assumed as follows:

$$\mathrm{C_2H_2} \rightarrow 2\mathrm{C(S)} + \mathrm{H_2} \qquad \text{with} \quad r_1 = 2k_1(T)[C_2H_2] \qquad (kmol\ m^{-3}\ s^{-1}) \tag{53}$$

$$\mathrm{C_2H_2} + n\mathrm{C(S)} \rightarrow (n+2)\mathrm{C(S)} + \mathrm{H_2} \qquad \text{with} \quad r_2 = 2k_2(T)f(A_s)[C_2H_2] \quad (kmol\ m^{-3}\ s^{-1}) \tag{54}$$

In these reactions $\mathrm{C(S)}$ represents carbon in its solid form. The terms $f(A_S)$ and $[C_2H_2]$ represent the functional dependence of soot surface growth on soot surface area per unit of volume and the molar concentration of acetylene. Leung *et al.* [77] proposed that the number of active sites present

locally in the flame is proportional to the square root of the total surface area available locally in the flame. This takes account in an approximated way the reduced reactivity of soot particles due to the effect of aging throughout the flame. This produces that the surface growth reaction (r_2) can be written as:

$$r_2 = 2k_2(T)\sqrt{A_s}[C_2H_2] = 2k_2(T)[C_2H_2]\sqrt{\pi\left(\frac{6\,M_c}{\pi\rho_s}\right)^{2/3}\left(\frac{\rho Y_s}{M_c}\right)^{1/3}(\rho N_s)^{1/6}} \qquad (kmol\,m^{-3}\,s^{-1}) \tag{55}$$

where the surface area per unit volume is calculated as $A_s = \pi d_s^2(\rho N_S)$, the diameter of the (assumed) spherical soot particles is taken as $d_S = (6Y_S/\pi N_S\rho_s)^{1/3}$, $\rho_S = 2000\ kg\ m^{-3}$ is the soot density and $M_c = 12.011\ kg\ kmol^{-1}$ is the soot molecular weight. The kinetic constants for the nucleation and growth rates proposed by Leung *et al.* [77] are:

$$\begin{aligned} k_1(T) &= 0.1 \times 10^5 \exp\left(-21100/T\right) \qquad (s^{-1}) \\ k_2(T) &= 0.6 \times 10^4 \exp\left(-12100/T\right) \qquad (m^{0.5}\,s^{-1}) \end{aligned} \tag{56}$$

Soot oxidation by O_2 is accounted by considering the following reaction and reaction rate:

$$\mathrm{C(S)} + 0.5\mathrm{O_2} \rightarrow \mathrm{CO} \qquad \text{with} \qquad r_3 = k_3(T)A_s[\mathrm{O_2}] \qquad (kmol\,m^{-3}\,s^{-1}) \tag{57}$$

with the corresponding rate given by:

$$k_3(T) = 0.1 \times 10^5\ T^{0.5} \exp\left(-19680/T\right) \qquad (m\,s^{-1}) \tag{58}$$

Finally, the source terms of the transport equations for the soot number density (S_N) and soot mass fraction (S_m) are defined as:

$$S_N = \frac{N_A}{C_{min}} r_1 - 2C_a\left(\frac{6\,M_c}{\pi\rho_s}\right)^{1/6}\left(\frac{6\,\kappa T}{\rho_s}\right)^{1/2}\left(\frac{\rho Y_s}{M_c}\right)^{1/6}(\rho N_s)^{11/6} \tag{59}$$

$$S_m = (r_1 + r_2 - r_3)M_c \tag{60}$$

where $N_A = 6.022 \times 10^{26}\ part\ kmol^{-1}$ is the Avogadro's number, $C_{min} = 100$ is the number of carbon atoms in the incipient soot particle, $\kappa = 1.38 \times 10^{-23}\ J\ K^{-1}$ is the Boltzmann constant and $C_a = 9.0$ is the agglomeration rate constant.

This set of equations describes the soot formation processes. One consequence of this simple formulation is that soot oxidation results in a reduction in the soot mass fraction and the particular diameter, but does not affect the particle number density equations directly. It is, however, considered sufficiently accurate for the present state of model development as the above rate expressions are not strong functions of the particle number density [77].

4.1.3 Liu's modification

Liu *et al.* [89] considered the model of Leung, Lindstedt and Jones and introduce modifications in order to apply it to smoking and non-smoking laminar coflow ethylene diffusion flames. Liu and coworkers assumed that the functional dependence of the soot surface growth on soot surface area

as linear, i.e. $f(A_s) = A_s$. This produces that the surface growth reaction can be written as (in place of equation (**55**)):

$$r_2 = 2k_2(T)A_s[C_2H_2] \\ = 2k_2(T)[C_2H_2]\pi\left(\frac{6\,M_c}{\pi\rho_s}\right)^{2/3}\left(\frac{\rho Y_c}{M_c}\right)^{2/3}(\rho N_s)^{1/3} \qquad (kmol\ m^{-3}\ s^{-1}) \tag{61}$$

The kinetic constant in the nucleation and growth rates used by this author are:

$$k_1(T) = 1.7\exp\left(-7548/T\right) \qquad (s^{-1}) \\ k_2(T) = 6.0\exp\left(-6038/T\right) \qquad (m\ s^{-1}) \tag{62}$$

The oxidation model considered originally by Leung *et al*. [77] was limited, although sufficient for applications in conterflow configurations. The oxidation model was extended by Liu *et al*. to be more adapted to treat coflow configurations. The reaction rate considered to take account of the O_2 oxidation is changed for one based on the Nagle and Strickland-Constable (NSC) model [120]. The reaction rate is written as:

$$r_3 = 120\left[\frac{k_a X_{O_2}\chi_1}{1+k_z X_{O_2}} + k_b X_{O_2}(1-\chi_1)\right]A_S f_{O_2} \qquad (kg\ m^{-3}s^{-1}) \\ \chi_1 = \left(1+\frac{k_t}{k_b X_{O_2}}\right)^{-1} \tag{63}$$

where X_{O_2} represents the O_2 molar fraction, with k_a, k_b, k_z and k_t defined from [117]:

$$k_a = 20\exp\left(-15098/T\right) \\ k_b = 4.46\times10^{-3}\exp\left(-7650/T\right) \\ k_t = 1.51\times10^{5}\exp\left(-48817/T\right) \\ k_z = 21.3\exp\left(2063/T\right) \tag{64}$$

They also incorporated the soot oxidation by OH, considering a reaction rate based on the Fenimore and Jones model [41]:

$$\mathrm{C(S)} + \mathrm{OH} \rightarrow \mathrm{CO} + \mathrm{H} \qquad \text{with} \qquad r_4 = \varphi_{OH}k_4 X_{OH} A_S f_{OH} \qquad (kg\ m^{-3}s^{-1}) \\ k_4 = 1.27\times10^{3}\,T^{-0.5} \tag{65}$$

with a collision efficiency factor of $\varphi_{OH} = 0.2$, which is higher than the experimental values of about 0.1–0.13 to partially compensate the neglected soot oxidation by the oxygen radical [89]. Liu *et al.* modified the commonly used NSC and OH soot oxidation rates by introducing two temperature-dependent correction factors f_{O_2} and f_{OH} in equations (63) and (65).

$$f_{O_2} = (1 + \exp[-(T - 1650)/80])^{-1}$$
$$f_{OH} = \begin{cases} 0.1824(1 + \exp[-(T - 1600)/85])^{-1}, & T \leq 1600\ \text{K} \\ (1 + \exp[-(T - 1675)/50])^{-1}, & 1600\ \text{K} < T < 1675\ \text{K} \\ (1 + \exp[-(T - 1650)/80])^{-1}, & T \geq 1675\ \text{K} \end{cases} \quad (66)$$

These correction factors were tuned numerically to match the amount of emitted soot in Santoro's non-smoking and smoking flame [135]. The authors also indicated that the transition from a non-smoking to a smoking flame and the amount of emitted soot were very sensitive to these correction values at temperatures below about 1650K, indicating the strong coupling between soot radiation and soot oxidation kinetics.

The primary soot particle coalescence is neglected in this model based on the experimental conclusions of Megaridis and Dobbins [101,102], who established that soot aggregates consist of more or less identical primary particles and who measured an almost constant primary soot particle density in the soot growth region. Using these considerations, the source terms of the transport equations should be written as (replacing equations (**59**) and (**60**)):

$$S_N = \frac{N_A}{C_{min}} r_1 \quad (67)$$

$$S_m = (r_1 + r_2)M_c - r_3 - r_4 \quad (68)$$

with $C_{min} = 700$. Liu *et al.* [89] used a thermophoretic velocity coefficient of 0.67 instead of the 0.55 used by Leung [77].

Liu and coworkers [52,88], in earlier articles, also included the effect of the soot oxidation by the O radical. They considered a reaction and a reaction rate given by:

$$\mathrm{C(S)} + \mathrm{O} \rightarrow \mathrm{CO} \qquad \text{with} \qquad r_5 = \varphi_O k_5 X_O A_S \quad (kg\ m^{-3} s^{-1}), \quad k_5 = 6.648 \times 10^2\ T^{-0.5} \quad (69)$$

with $\varphi_O = 0.2$. By including this oxidation process the soot mass fraction source term is now given by:

$$S_m = (r_1 + r_2)M_c - r_3 - r_4 - r_5 \quad (70)$$

4.1.4 Lindstedt modification

In order to improve the generality of the model, Lindstedt [80] modified the soot inception model, based on acetylene as the only soot precursor species in the pioneering work of Leung *et al.*, by considering that soot nucleation can be also attributed to benzene (C_6H_6). This model was subsequently applied by Fairweather and colleagues to methane, ethylene and propane turbulent jet flames [156,161].

This consideration is based on observations that the original nucleation model provides good agreement for simple fuels, but is less satisfactory for more complex cases. This means that besides the reaction expressed in equation (**53**), the following soot inception reaction is considered:

$$\mathrm{C_6H_6} \rightarrow 6\mathrm{C(S)} + 3\mathrm{H_2} \quad (71)$$

The nucleation reaction rate is now given by first-order acetylene and benzene reactions:

$$r_1 = 2k_1(T)[C_2H_2] + 6k_{1'}(T)[C_6H_6] \qquad (kmol\ m^{-3}\ s^{-1}) \tag{72}$$

Lindstedt [80], as well as Liu *et al.* [89], considered a linear functional dependence of the soot surface growth on soot surface area ($f(A_s) = A_s$). Therefore the surface growth reaction rate (r_2) is considered as in equation (**61**). The kinetic constants used by Lindstedt are:

$$\begin{aligned} k_1(T) &= 0.63 \times 10^4 \exp\left(-21000/T\right) \quad (s^{-1}) \\ k_{1'}(T) &= 0.75 \times 10^5 \exp\left(-21000/T\right) \quad (s^{-1}) \\ k_2(T) &= 0.75 \times 10^3 \exp\left(-12100/T\right) \quad (m\ s^{-1}) \end{aligned} \tag{73}$$

The soot particle number density source term is given by equation (**59**), with $C_{min} = 60$ and $C_a = 9$.

4.2 Flow field models

The radiative property models and the soot models have been implemented into a CFD code previously developed at the University of Provence for research purposes. This code has been used for predicting firespread through fuel beds [128] and to model the fire-water mist interactions [20,121] in order to characterize/understand their complex relation. These and several other applications have proven that the CFD code is well designed to incorporate detailed chemistry, semi-empirical soot models and advanced radiative property models.

The overall continuity equation, the Navier-Stokes equations in a low Mach number formulation and transport equations for the mixture fraction (Z) and the total enthalpy (h) are solved. The source term in the enthalpy transport equation is determined from the radiative model, while the soot model implies the resolution of two extra transport equations, one for the soot mass fraction (Y_s) and another for the soot number density (N_s). The combustion model requires the resolution of an extra transport equation for the adiabatic enthalpy (h_{ad}). All gas related magnitudes (Y_i, ρ, μ, D_{th}) and temperature are interpolated from state relationships.

4.2.1 Combustion model

Talking into account the large number of chemical species and chemical reactions involved in the soot formation and oxidation processes is prohibitive when performing numerical simulation of soot formation within CFD codes. Under the assumption of widely separated time scales for chemical reactions and transport processes, the combustion chemistry attains a quasi-steady state and immediately adjusts to local flow-field conditions. By this, the chemical kinetics can be decoupled from the mixing process. This idea is realized in the flamelet concept [122].

By using the Steady Laminar Flamelet Model (SLF) the gas mass fraction equations can be replaced by a single mixture fraction equation, (Z). This parameter is a good scalar for representing non-premixed flames since they are controlled by the mixing of fuel and oxidiser: It changes rapidly perpendicular to the flame front and tracks the mixing of the components ($Z = 0$ for pure air and $Z = 1$ for pure fuel). The flamelet equations are a simplified form of the species and energy transport equations, transforming these equations from a physical space into a mixture fraction space. In this transformation the tangential gradients with respect to the flame front are neglected in comparison to those normal to it. Therefore the flamelet formulation is reduced to a one-dimensional structure normal to the surface of the stoichiometric mixture. The parameter which takes into account the flow field into the flamelet structure is the scalar dissipation rate ($\chi = 2D_{th}\left(\overrightarrow{\nabla Z} \cdot \overrightarrow{\nabla Z}\right)$, with D_{th} the thermal diffusivity). This parameter measures the degree of departure from the equilibrium state,

taking the value χ_{st} at the flame surface. It can be interpreted as the inverse of a characteristic diffusion time or as a diffusivity in the mixture fraction space.

The flamelet solutions for a series of scalar dissipation rates ranging from a very small value (the equilibrium limit) to a large value (the quenching limit) form what is widely known as the flamelet library. An alternative way to establish the flamelet library, as considered in this study, is to solve the governing equations of counterflow diffusion flames (physical space) at a series of specified stretch rates. The link between the physical space and the mixture fraction coordinate is given by a properly defined mixture fraction. Once the solutions of these counterflow diffusion flames are obtained in the physical space, via the OPPDIF code [93], the mixture fraction distributions are obtained by solving transport equations for the mixture fraction, as suggested by Pitsch and Peters [125]. The flamelet library was generated from the counterflow configuration using CHEMKIN codes [93] and considering a series of stretch rates ranging from $0.2s^{-1}$ to extinction [91].

In order to incorporate heat losses in the flamelet description, an enthalpy defect parameter is introduced by using the methodology described by Carbonell *et al.* [11]. This parameter is defined as:

$$X_R = \frac{h - h_{ad}}{h_u - h_{ad}} \tag{74}$$

where h_{ad} and h_u are the adiabatic and the unburned enthalpies respectively. The unburned enthalpy is evaluated assuming that all energy released by combustion is lost and the gaseous mixture is cooled down to ambient temperature. The idea of this approach consists in generating flamelet profiles for each χ_{st} with different degrees of heat losses. The procedure can be described as follows: the flamelet profiles for every χ_{st} were first generated at adiabatic conditions. Then, the generation of the corresponding flamelet profiles for non-adiabatic conditions is carried out iteratively for several different radiative losses as indicated by Carbonell *et al.* [11] .

Two chemical reaction mechanism schemes are used in this study. Firstly the GRI-Mech 3.0 is chosen. This scheme was designed to model natural gas combustion, including NO formation and reburn chemistry. It considers 53 species and 325 elementary chemical reactions [139]. The second chemical mechanism scheme used in this study is the one developed by Qin *et al.* [129]. This scheme considers 70 species and 463 chemical reactions, being optimized for the oxidation of C3 hydrocarbon species.

The flamelet equations were solved in advance in a pre-processing task, generating the flamelet library (also called state relationships). Once the flamelet library is created, the only terms that are required to be calculated in the CFD code (physical space) are the mixture fraction, the scalar dissipation rate and the enthalpy defect. All gas related magnitudes and temperature can be evaluated in the physical space directly from the flamelet libraries. This process has the advantage that the number of equations to be solved is dramatically reduced, while the combustion mechanism is treated in the pre-processing task.

The parts of the soot reaction rates related to the gas phase are also stored in the flamelet library. It is important to mention that this procedure implies that the gas-phase species and soot mechanism are decoupled, since flamelet equation are not solved interactively with the CFD calculations.

The SLF provides only approximate solutions as compared to direct simulations [12,91] since the chemical kinetics and the mixing process are considered as decoupled and the gas-phase species and

soot mechanism are also decoupled. Despite these approximations previous studies found that this approach is suitable to model soot formation in laminar coflow diffusion flames [4,12,118].

4.2.2 Transport equations

The transport equations resolved in this study can be summarized as follows:

$$\frac{\partial}{\partial t}(\rho\Phi) + \frac{1}{r}\frac{\partial}{\partial r}(r\rho u_r\Phi) + \frac{\partial}{\partial z}(\rho u_z\Phi) = \frac{1}{r}\frac{\partial}{\partial r}\left(r\Gamma_{\Phi_r}\frac{\partial\Phi}{\partial r}\right) + \frac{\partial}{\partial z}\left(\Gamma_{\Phi_z}\frac{\partial\Phi}{\partial z}\right) + S_\Phi \quad (75)$$

where Φ is the transported quantity, Γ_{Φ_i} is the diffusion coefficient and S_Φ is the source term. These terms are listed for each transport equation in Table 4.1.

Table 4.1. Summary of the transport equations solved in the simulations.

Equation for:	Φ	Γ_{Φ_i}	S_Φ
Continuity	1	0	0
Axial Momentum	u_z	μ	$-\frac{\partial p_d}{\partial z} + (\rho-\rho_\infty)g_z + \frac{1}{r}\frac{\partial}{\partial r}\left(r\mu\frac{\partial u_r}{\partial z}\right) + \frac{\partial}{\partial z}\left(\mu\frac{\partial u_z}{\partial z}\right) - \frac{2}{3}\frac{\partial}{\partial z}\left[\mu\left(\frac{1}{r}\frac{\partial(ru_r)}{\partial r} + \frac{\partial u_z}{\partial z}\right)\right]$
Radial Momentum	u_r	μ	$-\frac{\partial p_d}{\partial r} + \frac{1}{r}\frac{\partial}{\partial r}\left(r\mu\frac{\partial u_r}{\partial r}\right) + \frac{\partial}{\partial z}\left(\mu\frac{\partial u_z}{\partial r}\right) - \frac{2}{3}\frac{\partial}{\partial r}\left[\mu\left(\frac{1}{r}\frac{\partial(ru_r)}{\partial r} + \frac{\partial u_z}{\partial z}\right)\right]$
Enthalpy	h	μ/Pr	$-\nabla\cdot q_R''$
Adiabatic Enthalpy	h_{ad}	μ/Pr	0
Mixture Fraction	Z	μ/Sc	0
Soot Mass Fraction	Y_s	$-\rho V_{T,i}$	S_m
Soot Number Density	N_s	$-\rho V_{T,i}$	S_N

$Pr = \mu C_p/\lambda$, $Sc = \mu/\rho D$

4.2.3 Numerical resolution

A time-dependant 2-D axisymmetric formulation is used for the resolution of the equations using a finite volume method in a staggered grid. A false time step technique is used. For the convective terms the ULTRASHARP approach is applied, while a second-order central difference scheme is used for the diffusion terms. The pressure-velocity coupling is solved using the Iterative PISO algorithm. The radiative transfer equation is solved by the finite volume method using the special mapping developed by Chui *et al*. for axisymmetric configurations [15], in which the 2 dimensional and the 2 angular coordinates are expressed in 3 dimensional and only one angular coordinate. These computations are carried out using the first-order UPWIND spatial discretization scheme and an

angular mesh with 12×16 control angles. The tridiagonal matrix algorithm (TDMA) is used to solve the transport equations. Convergence is achieved when the maximum relative error for all the computed variables is lower than 10^{-4}.

4.3 Modelling radiative heat transfer in sooting laminar coflow flames

The objective is to assess the different radiative property models in the case of coflow ethylene-air sooting diffusion flames. To do that CFD calculations are carried out, considering the soot model proposed by Liu *et al.* [89] (see section 4.1.3) and a simple radiative model. In this case a Planck-mean model is selected, considering CO_2, H_2O, CO as participating gaseous species and soot. Planck absorption coefficients are calculated from the Narrow Band database of Soufiani and Taine [146]. For the soot model a thermophoretic velocity coefficient of 0.55 is considered. Once the flames are calculated, temperature, species molar fractions and soot volume fraction are obtained and used to estimate de divergence of the radiative flux (radiative source) produced for every radiative model considered. This procedure allows quantifying the differences that produce each radiative model alone, taking out the possible differences that can introduce the rest of the models considered in the simulations.

4.3.1 Flame fields generation

The flames considered in this section are the Smoking (S) and Non-Smoking (NS) ethylene-air coflow diffusion flames studied experimentally by Santoro *et al.* [135], Megaridis and Dobbins [101,102] and Smyth [142], and numerically by Liu *et al.* [89] and Kennedy *et al.* [61], among others. Experiments used a burner consisting in two concentric tubes of 11.1 mm and 101.6 mm inner diameter respectively. Pure ethylene flows through the inner tube, while air passes through the annular region between the two tubes. The mean velocities for the fuel and air streams are of 3.98 cm s^{-1} and 8.9 cm s^{-1} for the NS flame and 5.05 cm s^{-1} and 13.3 cm s^{-1} for the S flame. A parabolic profile is imposed for the fuel injection zone while a flat profile is considered for the oxidant injection zone. A small solid wall of 0.55 mm separates both injection zones. Fuel and oxidizer are injected at ambient temperature neglecting the effects of preheating. Ambient temperature and pressure are fixed to 300 K and 1 atm.

The fields obtained for the S and the NS flame are presented in Figure 4.1 and Figure 4.2 respectively. A proper validation of the results obtained was carried out, but presented elsewhere [29] since the results are quite similar to those presented in the next section.

4.3.2 Assessment of the radiative models

With the flame fields shown in the last figures the divergence of the radiative flux is calculated with the SNBCK model, considering 43 Narrow Bands [146], 7 quadrature points and using the mixing scheme of Modest and Riazzi [114]. This model is considered as the reference for this assessment. Local relative errors between the current model and the reference are estimated as:

$$E_{r,i}(\phi) = \frac{\left(\phi_{model,i} - \phi_{ref,i}\right)}{\phi_{ref,i}} \tag{76}$$

where *i* represents the current mesh point and ϕ is the variable considered, $\nabla \cdot q_R''$ in this case. In order to avoid interpreting discrepancies encountered in regions where ϕ is close to zero, points where $\left|\phi_{ref,i}\right| < 0.1 \times \max_{i=1,N}\left|\phi_{ref,i}\right|$ are excluded from the error analysis. Mean and maximum errors are defined as $E_{mean} = 1/N\left(\sum_{i=1}^{N}\left|E_{r,i}\right|\right)$ and $E_{max} = \max_{i=1,N}\left|E_{r,i}\right|$, respectively. Mean and

maximum relative errors (in %) are summarized in Table 4.2. This table also summarizes the CPU ratio between the current model and the reference.

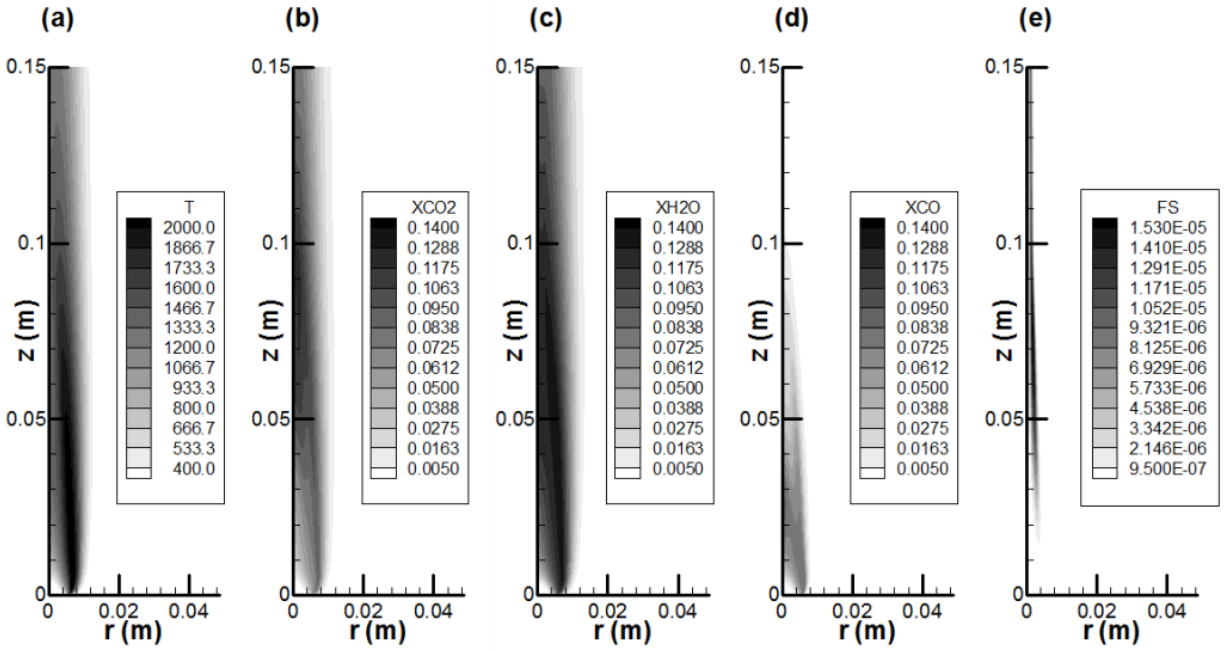

Figure 4.1. Fields obtained for the smoking (S) flame: (a) temperature, (b) CO_2 molar fraction, (c) H_2O molar fraction, (d) CO molar fraction and (e) soot volume fraction.

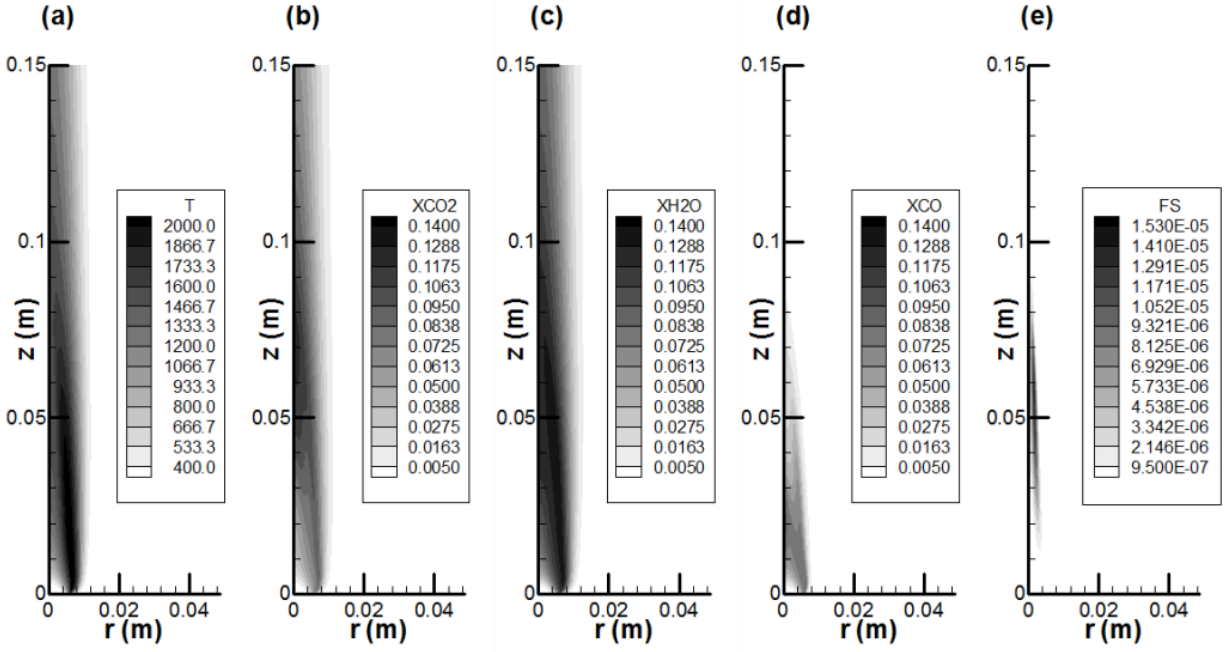

Figure 4.2. Fields obtained for the non-smoking (NS) flame: (a) temperature, (b) CO_2 molar fraction, (c) H_2O molar fraction, (d) CO molar fraction and (e) soot volume fraction.

Table 4.2. Error estimations on the radiative source term for the S flame. The SNBCK43 model is used as reference. The third column represents the CPU time ratio between the current model and the reference. Maximum and mean errors greater than 30% and 15% are shaded.

Kind of model	Models	CPU Ratio	$E_{max}(\%)$	E_{mean} (%)
Grey Model	OTA	--	43.2	15.53
	Planck	1/216	37.5	6.94
	FDSg	1/58	32.3	7.81
	WSGGg	1/66	60.5	16.78
WB Model	GWB	1/38	24.9	4.83
Global Models	WSGG	1/52	6.25	1.81
	FSCK	1/21	13.73	1.46
	FSSK	1/20	12.21	1.25
NB Models	SNBCK43 N_G=4	1/3.5	1.99	0.38
	SNBCK43 N_G=2	1/9.5	4.48	0.97

Figure 4.3 shows the divergence of the radiative flux predicted by the reference model for the S and NS flames. The fields of relative errors induced by the OTA and by solving the RTE with Planck absorption coefficients for gas and soot are also represented. These results show large discrepancies between the OTA and the SNBCK, with mean and maximum deviations of about 16% and 43% respectively (see Table 4.2). Predictions are widely improved by using the FVM with Planck absorption coefficients. In this case the mean discrepancy is reduced to about 7% but large local errors, greater than 30%, are still observed. Liu *et al.* [89] found bigger differences for the integrated soot volume fraction between the OTA and the DOM/SNBCK than those reported here by considering the OTA and the FVM with Planck-mean absorption coefficients. This suggests that the level of discrepancies introduced by considering the Planck-mean absorption coefficients are too large to predict accurately the temperature field, especially in the soot oxidation region where physical processes are very sensitive to temperature.

Due to their inherent nature or due to simplification, some of the other models considered in the present study treat soot as grey particles by using Planck mean-absorption coefficients (grey models, WSGG, ..) and/or ignore the contribution of CO (grey models, WSGG, GWB,..). It appears then important to quantify the discrepancies generated by these approximations. In order to accomplish this task, the SNBCK 43 is run by considering soot as grey particle and by ignoring the contribution of CO. These approximations are compared with the reference solution in the Figure 4.3d and Figure 4.3e. The results show that the contribution of CO is marginal, inducing discrepancies of less than 1.5% at the periphery of the region where soot particles are located. The assumption of grey soot influences the prediction in a more significant manner with errors of the order of 2% in regions where the soot volume fraction is the most important.

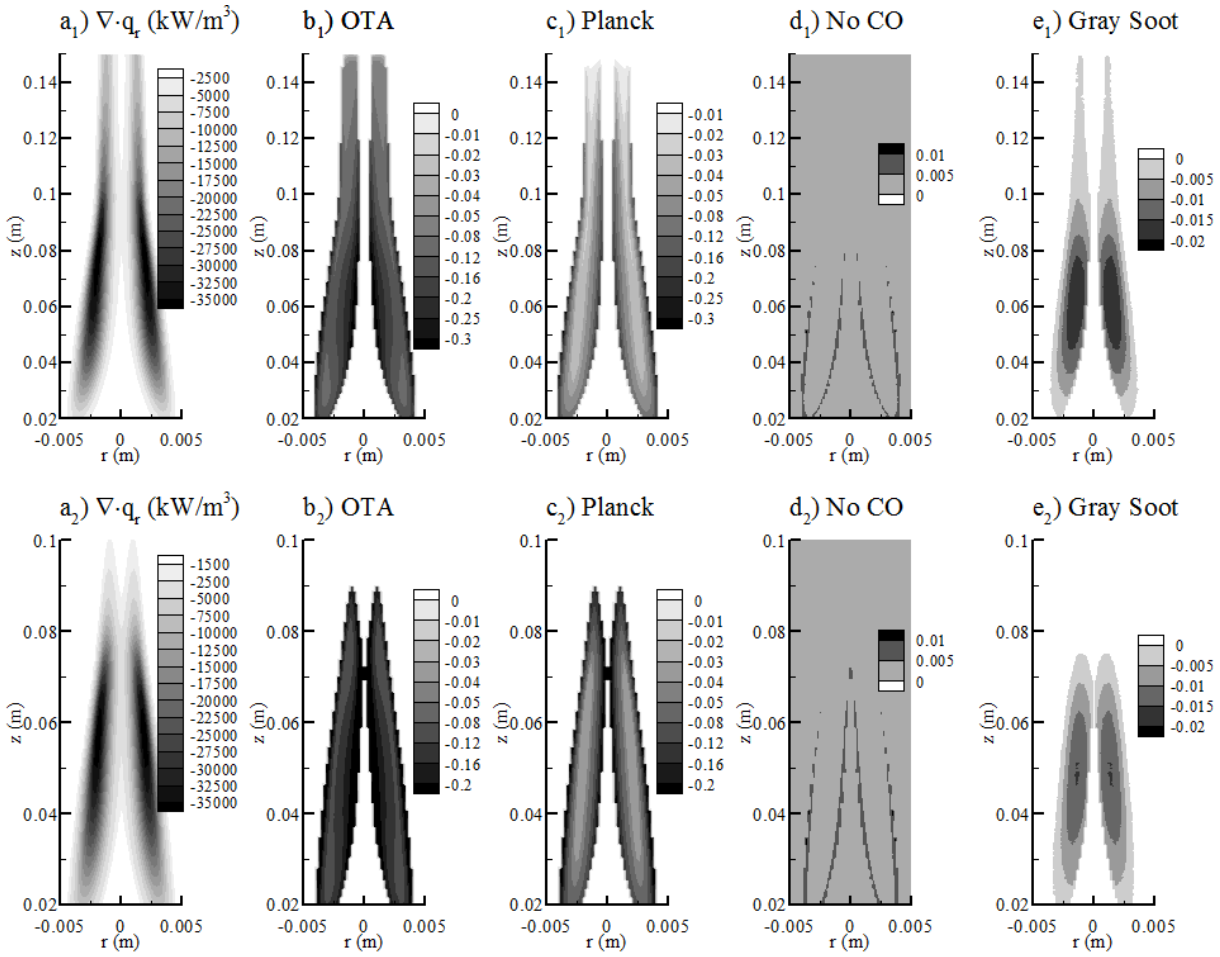

Figure 4.3. a)Divergence of the radiative flux, b) relative error ($E_{r,i}$) for the OTA, c) $E_{r,i}$ for the FVM + Planck-mean absorption coefficients, d) $E_{r,i}$ induced by ignoring the CO contribution and e) $E_{r,i}$ induced by using Planck-mean absorption coefficient for soot. Subindex 1 and 2 refer to the S and NS flames, respectively.

Figure 4.4 shows the fields of relative error for the different radiative property models in the case of the S flame. The first important result is that considering only two quadrature points for the SNBCK does not alter significantly the spectrally-integrated divergence of the radiative flux while reducing the computational efficiency by a factor of about 10. This result is in agreement with previous conclusions drawn from simulations of radiative benchmarks involving non-sooting and sooting media [90,28]. The second important result is that grey models, i.e. the FDSg and the WSGGg, present globally larger discrepancies than those reported for Planck-mean absorption coefficients. As a consequence, grey models, although being very efficient on the computational point of view, are not sufficiently accurate to be used in such simulations.

The predictions achieved with the GWB are more satisfactory than those obtained with the grey models with a moderate increase in CPU time. The mean error is of about 5% and acceptable discrepancies are observed along the annular region where soot is confined. However large local discrepancies greater than 20% are encountered at the periphery of the soot region.

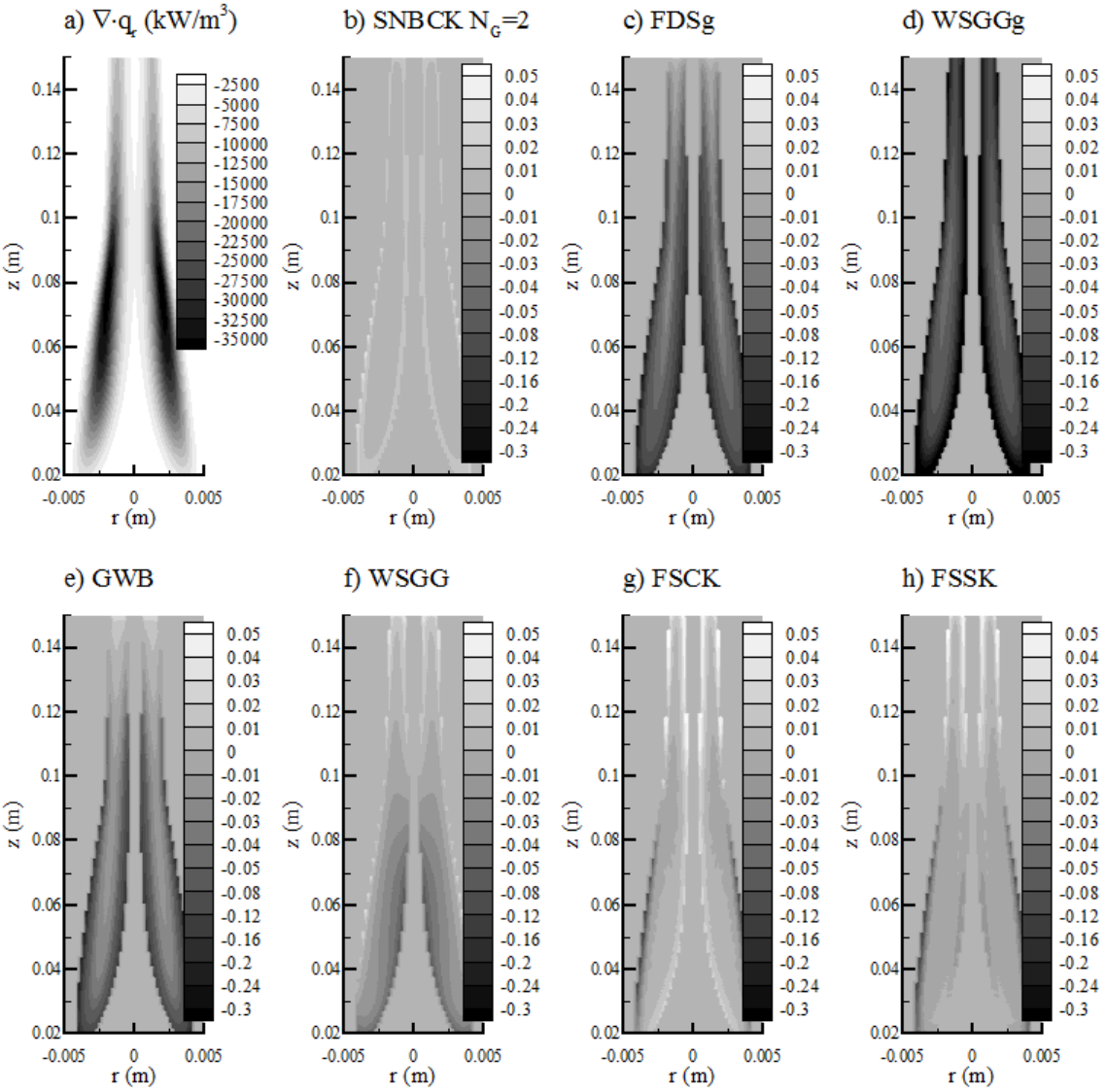

Figure 4.4. Relative errors for the different radiative property models for the S flame.

The results obtained with the WSGG are surprisingly good. Nevertheless they are somewhat fortuitous due to the fact that the parameters of the model, i.e. a_j and κ_j, are obtained for $p_{H_2O}/p_{CO_2} = 1$, this condition being never encountered in the computational domain as a consequence of incomplete combustion and differential diffusion.

The FSCK and the FSSK models are slower than the GWB model with increases in CPU time by factors of 1.8 and 1.9 respectively. Nevertheless they provide accurate solutions with mean discrepancies of less than 1.5%. Table 4.2 shows that the FSSK is slightly more accurate than the FSCK. This result is in agreement with the conclusions drawn by Modest [109]. Both model provide relatively accurate results with a reduction in CPU time by about a factor 2 as compared to the SNBCK43 with N_G=2. As a consequence, these methods seem to be a good alternative to the SNBCK model.

4.4 Influence of radiative property models on soot production

One of the characteristics observed in the previous comparisons is the high sensitivity of the results by considering different radiative property models. This implies that in a coupled simulation, i.e.

considering the radiative source calculated inside the CFD simulation, they may produce important changes in the solution, and in particular in the soot production. Several studies have shown that the relation between radiation and soot kinetics is important and complex.

This coupling is generally treated in a simple manner using the Optically Thin Approximation (OTA) [4,3,141], despite some studies which concluded that a detailed modelling of thermal radiation is necessary for accurately predict the flame structure, species concentrations and formation of soot [54,89,88,167]. In one of these studies, Liu *et al.* [89] showed that the use of the OTA induces significant temperature under-predictions in the upper part of coflow laminar ethylene diffusion flames, affecting directly the prediction of soot volume fractions. Despite these efforts, an extensive comparison of several radiative properly models on soot predictions has not been reported.

The aim of the present section is to assess the influence of different radiative property models over the soot formation/oxidation processes in axisymmetric laminar coflow ethylene flames. To accomplish this task Santoro's Smoking (S) and Non-Smoking (NS) flames [135], investigated in the previous section, are simulated by considering different radiative property models. These models are considered in a coupled way within the simulations.

The same soot model used in the previous section, and presented in section 4.1.3, is considered for this section. However some of the soot constants are slightly modified to improve the agreement with the experimental data. In this case the thermophoretic velocity coefficient is taken as 0.55 (as Leung *et al.* [77]). The soot growth pre-exponential constant is reduced to 5 instead of 6, and the collision efficiency factor φ_{OH} is reduced from 0.2 to 0.05. The oxidation by the O radical is also considered.

4.4.1 Comparison with experimental data

A first comparison is carried out in order to assess the main characteristics of the simulations and have an overall idea of the accuracy obtained. Computations carried out with the SNBCK model are compared to the experimental data of Santoro *et al.* [135] and Megaridis and Dobbins [101,102]. Figure 4.5a and Figure 4.5b present the radial profiles of temperature and soot volume fraction at three heights of the NS flame. Overall predictions present an acceptable agreement with the measurements, especially for the temperature. The locations of the temperature peaks as well as their magnitudes are well predicted at z = 7 mm and 20 mm. The preheating of the fuel caused by conduction with the pipe flow is disregarded in this study, which may explain the under-prediction observed for the centreline values (see Figure 4.5a).

Figure 4.5b shows that the predicted profiles of soot volume fraction at these two heights present wider peaks, with values slightly lower than the experiments. The results at z = 70 mm show that the numerical simulations still predict the peaks of soot volume fraction and temperature in an annular region whereas the experiments exhibit a maximum value along the centreline (see Figure 4.5a and Figure 4.5b).

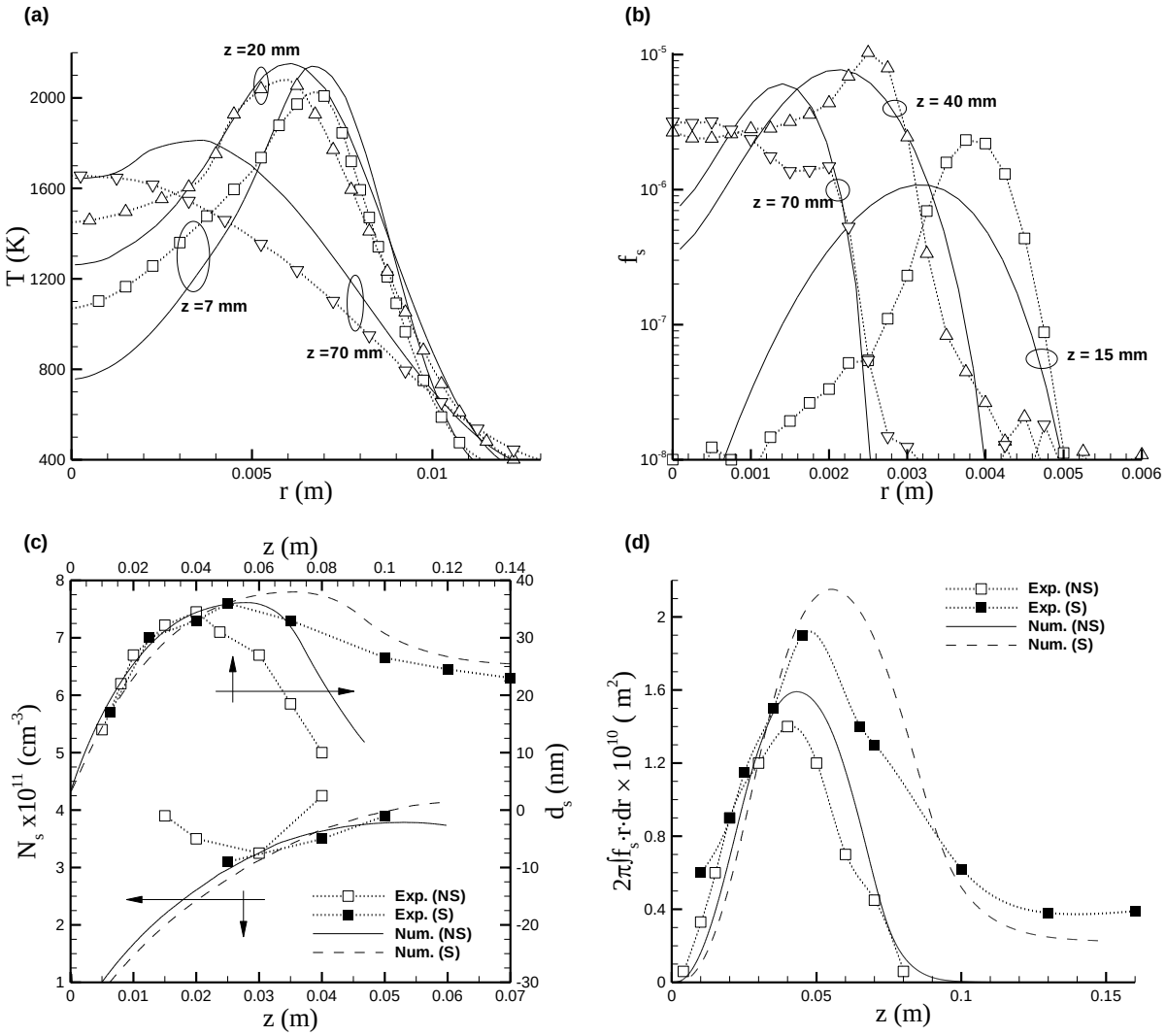

Figure 4.5. Comparisons between experimental data and predictions obtained with the SNBCK model. Radial profiles of (a) temperature and (b) soot volume fraction at different heights for the NS flame, experimental values from Santoro *et al.* [135]; (c) soot primary particle number density and soot primary particle diameter along the path line exhibiting the maximum soot volume fraction for the NS and S flames, experimental values from Megaridis and Dobbins [101,102]; and (d) integrated soot volume fraction along the flame height, experimental values from Santoro *et al*. [135].

Figure 4.5c presents the soot primary particle number density and the soot primary particle diameter along the path line exhibiting maximum soot volume fraction for both flames. The experimental data show that the values of soot primary particle number density in both flames are quite similar in most of the soot growth region. Numerical results are in reasonable agreement with the experimental data for both flames. The soot primary particle diameter also presents the same behaviour as observed experimentally. For both flames an excellent agreement between simulations and experiments is achieved within the first 4 cm. Above this height the diameter is somewhat over-predicted, showing that the model underestimate the oxidation process.

Figure 4.5d presents the integrated soot volume fraction along the flame height for both flames. Results show that two distinct regions are observed: in the first region, soot nucleation and surface

growth processes produce an important increase in the soot volume fraction with height. This is followed by an oxidative region where the overall soot volume fraction decreases until the soot is completely burned, as in the NS flame, or partially burned, as in the S flame. A comparison between the experiments and the numerical results shows that the integrated soot volume fraction is slightly underestimated in the lower part of both flames. At the peaks this tendency is inverted and a more important overestimation is observed. The predicted peak locations are shifted by a few millimetres away from the burner as compared with the experiments.

4.4.2 Influence of radiative models in soot predictions

The accuracy of the different radiative property models is assessed by using the SNBCK model (43 Narrow bands, 7 quadrature points and mixed with the scheme of Modest and Riazzi) as reference for the S flame. Local relative errors between the current model and the reference are estimated as in equation (**76**). In order to avoid interpreting discrepancies encountered in regions where ϕ is close to zero, points where $\left|\phi_{ref,i}\right| < 0.02 * \max_{i=1,N}\left|\phi_{ref,i}\right|$ are excluded from the error analysis.

Figure 4.6a, Figure 4.6b and Figure 4.6c present the temperature, the divergence of the radiative flux (radiation source term for the energy equation) and the soot volume fraction along the path of maximum soot volume fraction for the SNBCK model. In these figures the temperature difference and the local relative error are also presented for all the radiative property models studied. Figure 4.6a shows that along the path line exhibiting the maximum soot volume fraction the temperature increase rapidly in the first 3cm and then reaches an approximately constant value in the range of 1500-1600 K; at around z = 9.5 cm the temperature starts to decrease linearly until it attains a temperature of 1300 K at z = 15 cm. The zone of constant temperature is characterized by very large radiative losses (see Figure 4.6b); the large soot volume fraction observed in this region is the main factor responsible of this intense radiation (see Figure 4.6c). Figure 4.6b shows that the radiative source term decreases after this zone due to a reduction in both temperature and soot volume fraction (see Figure 4.6a and Figure 4.6c). Figure 4.6d shows the integrated soot volume fraction along the flame height for the SNBCK model and the relative errors obtained with the different radiative models considered. Between z = 6 cm to z = 12 cm the dominant mechanism is the soot oxidation. The results show that the oxidation process is quite sensitive to the radiative property model, more sensitive than the nucleation and the surface growth of the soot. This is directly related to the temperature attained for every model, conditioning the oxidation rates in each simulation. This effect produces important relative errors between the models for all the quantities analysed, especially in the oxidation region (see Figure 4.6). Therefore the choice of a radiative property model largely affects the amount of soot released by the flame.

Table 4.3 summarizes the mean and maximum relative error, or temperature difference, obtained for all the radiative models presented in Figure 4.6. The first important result is that the OTA leads to very poor predictions, with a maximum under-prediction of the temperature of about 139 K. Maximum errors are higher than 100% for all the variables considered and the amount of soot released from the flame is largely overestimated. In addition the OTA also affects significantly the soot production in the soot growth zone, where the soot volume fraction is around 15% lower as compared to the SNBCK (see Figure 4.6c). These comparisons show clearly that reabsorption by gas and soot should be considered. If reabsorption is taken into account by considering the simple grey model based on Planck-mean absorption coefficient (Planck model), Table 4.3 shows that

temperature differences and relative errors are similar to those obtained with the OTA. The grey model implemented in FDS (GWBg) improves the predictions but discrepancies are still high.

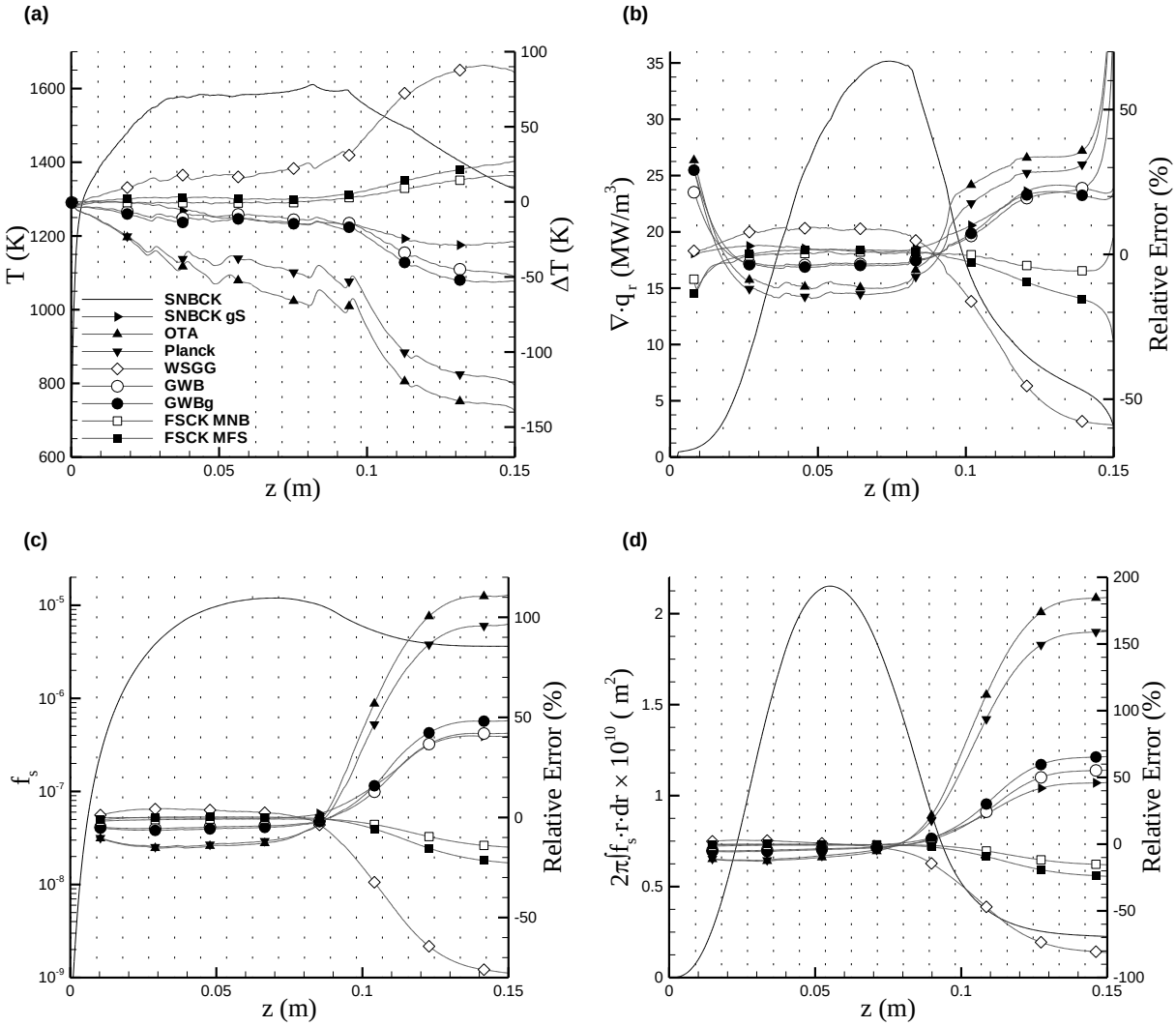

Figure 4.6. Comparisons between radiative property models for the S flame. The solution predicted by SNBCK model acts as reference. (a) Temperature and temperature differences, $\Delta T = T_{model} - T_{ref}$, (b) divergence of the radiative flux and (c) soot volume fraction along the path line exhibiting the maximum soot volume fraction; and (d) integrated soot volume fraction along the flame height. The reference curve is represented on the left axis whereas the relative errors for the other methods are represented on the right axis.

The influence of the grey approximation for soot can be isolated by considering non-grey gases, modelled by the SNBCK, and grey soot modelled by a Planck-mean absorption coefficient. Table 4.3 shows that this approximation (SNBCKgs) should also be avoided, demonstrating that the spectral nature of soot must be taken into account. Although temperature is relatively well predicted with a maximum difference of 29 K as compared to the reference, it produces substantial mean errors of about 8.5, 12.5 and 14.3% for the radiative source term, the soot volume fraction and the integrated soot volume fraction respectively.

GWB and WSGG take into account the spectral dependence of combustion gases and soot in a simplified manner. The GWB model presents similar discrepancies as the GWBg discussed previously with a maximum temperature difference of about 50 K. The parameters of the WSGG model, i.e. a_j and κ_j, are obtained for fixed ratios of $\mathrm{H_2O}$ and $\mathrm{CO_2}$ partial pressures. In the present study, a ratio of $P_{H_2O}/P_{CO_2} = 1$ is considered, resulting from the complete combustion of ethylene in air. It should be noted that this condition is never encountered in the computational domain as consequence of incomplete combustion and differential diffusion. This may explain the large discrepancies observed for this model.

The FSCK model using the mixed-NB database and spectral soot (FSCK MNB) predicts temperatures that are quite close to the reference, with only mean and maximum differences of around 5 and 18 K, respectively. This model also present the lowest relative errors among all the radiative models tested, with mean and maximum errors lower than 4.3 and 16%. These discrepancies may be explained by the assumption of a correlated absorption coefficient, which is introduced for both NB and FS k-distributions in the case of a non-homogeneous non-isothermal medium. This assumption is less restrictive on a NB basis than on a FS basis. By considering the mixed-FS database and grey soot (FSCK MFS) the solution are obviously less accurate. Nevertheless, the errors are globally lower than the SNBCKgs and closer to the FSCK MNB.

Table 4.3 also summarizes the CPU time ratio between the current model and the SNBCK ($CPU_{ratio} = t_{ref}/t_{model}$). It is important to mention that each calculation differs only by the radiative model considered. The FSCK MNB model, which present the best results compared to the SNBCK, provides a solution with a CPU time reduced by a factor of 4, making it attractive for this kind of calculation.

Table 4.3. Error estimations or temperature difference, for the temperature, the divergence of the radiative flux and the soot volume fraction along the path of maximum soot volume fraction, and the integrated soot volume fraction along the flame height calculated with different radiative property models for the S flame. The SNBCK model is used as reference. Last column presents the CPU time ratio between the reference and the other models. Maximum and mean errors greater than 30% and 15% are shaded. $CPU_{ratio} = t_{ref}/t_{model}$.

Model	T (K)		$\nabla \cdot \dot{q_r}''$ (%)		f_S (%)		Integ. (%)		*CPU ratio*
	ΔT_{mean}	ΔT_{max}	$E_{r,mean}$	$E_{r,max}$	$E_{r,mean}$	$E_{r,max}$	$E_{r,mean}$	$E_{r,max}$	
OTA	72.1	139.0	19.7	135.6	42.4	111.1	65.3	184.8	153.4
Planck	59.2	122.0	18.7	130.9	36.7	96.6	55.9	159.4	111.2
WSGG	37.8	91.0	20.2	59.2	24.7	77.7	27.6	81.2	52.9
GWBg	23.0	54.0	9.3	29.1	16.9	48.4	21.5	65.6	63.9
GWB	19.4	50.0	9.6	79.3	14.5	42.1	17.9	55.4	33.4
SNBCKgs	14.1	29.0	8.5	23.9	12.5	40.8	14.3	46.1	1.0
FSCK MNB	4.7	18.0	2.2	16.0	4.1	14.8	4.3	15.4	4.0
FSCK MFS	7.9	27.0	5.1	29.3	5.8	22.7	6.7	24.1	20.5

4.5 Evaluation of an acetylene/benzene-based semi-empirical soot model

In the previous sections comparisons were carried out by considering an ethylene-air diffusion flame. A set of parameters, especially calibrated to provide accurate soot volume fraction predictions, was applied in order to test the influence of different radiative models. However, this formulation was found to be limited to ethylene normal coflow diffusion flames.

In this section a more general formulation, considering acetylene and benzene as precursor of the soot nucleation process, is tested for a set of flames considering four different fuels: methane, CH_4, ethylene, C_2H_4, propane, C_3H_8, and propylene, C_3H_6. Two ethylene-air inverse diffusion flames are also tested. It is important to properly test this soot model for different fuels and configurations, which present different sooting characteristics, in view of applications to turbulent flames.

4.5.1 Soot model

The model presented in section 4.1.4 is considered for the soot formation processes, considering the influence of acetylene and benzene for the soot nucleation, and a linear functional dependence of the soot surface growth on soot surface area for the surface growth (equations (**72**) and (**61**) respectively).

Although this formulation is more general than acetylene-based empirical soot models, two different sets of parameters were necessary for providing reliable results for the four different fuels tested. These two sets are summarized in Table 4.4, indicating which set of parameters is used for each fuel. The surface growth pre-exponential constant (A_2) derived by Lindstedt [80] is used for C3 hydrocarbons (C_3H_8 and C_3H_6), whereas this value is divided by a factor of about 2 for C1-C2 hydrocarbons (CH_4 and C_2H_4). This consideration is consistent with the observations of Leung *et al.* [77], who doubled the pre-exponential constant derived for ethylene in order to obtain optimal predictions for propane flames.

The introduction of C_6H_6 as a precursor for nucleation was found to improve the model results for a particular set of hydrocarbons as compared to soot models based only on acetylene. In particular, predictions for methane flames were found to be in better agreement with the experimental data. The use of two sets of parameter can be explained from the simplifications of the soot model. A possible way to generalize the soot model would be to introduce a nucleation step based on the coagulation of large size PAH [2]. However, simple formulations are desirable in view of applications to turbulent flames, which explain the present choice. The parameters adopted for the nucleation and the surface growth processes are summarized in Table 4.4.

Table 4.4. Reaction rate constants for soot nucleation and surface growth processes, in the form of an Arrhenius expression, $k_j = A\,\exp(-T_a/T)$ (Units in K, m, s).

k_j	A	T_a	Fuel	Ref.
k_1	0.63×10^4	21000	C1-C3 hydrocarbons	[80]
$k_{1'}$	0.75×10^5	21100	C1-C3 hydrocarbons	[80]
k_2	0.40×10^3	12100	C1-C2 hydrocarbons	--
	0.75×10^3	12100	C3 hydrocarbons	[80]

Soot oxidation by O_2 is given by the NSC model [120] while soot oxidation by OH and O are based on the Fenimore and Jones model [41] (equations **(63)**, **(65)** and **(69)** respectively). No correction functions are applied for the O_2 and OH terms ($f_{O_2} = f_{OH} = 1$) and collision efficiency factors of $\varphi_{OH} = 0.13$ and $\varphi_O = 0.2$ are considered. For the present calculations the chemical mechanism of Qin *et al.* [129], optimized for C3 species combustion, is used.

4.5.2 Radiative property model

For carrying out this section the FSCK model is considered as the radiative property model based on the results obtained in the previous sections and in the previous chapter. This model provides results in very close agreement to the ones obtained with the SNBCK model with a significant gain in CPU time. For the present calculations the FSCK model is applied with the Mixed Narrow Band database (derived from the 43NB database, mixed and assembled with the schemes of Modest and Riazzi) considering 7 quadrature points for the integration of the k-distributions. This model allows considering the soot as non-grey (see chapter 2 section 2.7).

4.5.3 Description of the test cases

In this section 15 different flames are simulated for four different fuels. Normal and inverse coflow diffusion flames are considered. These flames were studied experimentally by Smyth [142] (methane, ethylene and propane), by Markstein and de Ris [97] (ethylene and propylene), Makel and Kennedy [95] (ethylene inverse diffusion flames) and Trottier *et al.* [149] (propane). The injection fluxes and burner dimensions are summarized in Table 4.5 for each flame. In every case the fuel and the oxidizer are considered as pure.

Two inverse diffusion flames (IDF) are simulated. The configuration of these flames is similar to that used to generate normal coflow diffusion flames, except that the relative positions of the fuel and oxidizer are inverted: the oxidizer and the fuel are injected through the central tube and the co-annular tube, respectively. In this type of flame the soot and polycyclic aromatic hydrocarbons (PAH) form on the outside of the flame, embedded in the fuel stream, changing radically the way they usually form in a normal diffusion flame. In the IDF the soot particles forms in an annular region outside and above the flame, escaping non-oxidized since they do not pass through the high-temperature reaction zone [107]. Due to its special characteristics, inverse flames are studied to gain insight into soot inception and growth, and to learn about soot formation in under-ventilated fires, since both have the potential to emit considerable quantities of soot [108]. Therefore, investigating these configurations is an exigent test for the soot model and an interesting case for studying soot formation in an idealized configuration representative of under-ventilated fire conditions.

One way to quantifying the sooting propensity of a hydrocarbon fuel is the smoke point height, i.e. the maximum height of a laminar flame of a certain fuel burning in air at which soot is not released from the flame tip. The smoke point height and the smoke point heat release rate for the fuels considered are summarized in Table 4.6. These data were obtained from [74]. From Table 4.6 it appears that the hydrocarbons considered cover a wide range of sooting propensity. Methane does not produce a significant amount of soot, whereas propylene can be considered as a heavily sooting hydrocarbon.

Table 4.5. Injection fluxes and burner dimensions for the 15 flames tested in this section.

Fuel	Flame	D (mm)	$Q_{fuel}(cm^3s^{-1})$	$Q_{air}(cm^3s^{-1})$	HRR (W)	Reference
Methane	CH4-S-78	11.1	7.53	633	--	Smyth[142]
	CH4-S-101	11.1	9.78	1170	--	Smyth[142]
Ethylene	C2H4-S-40	11.1	3.85	694	212	Smyth[142]
	C2H4-S-41	11.1	4.00	694	220	Smyth[142]
	C2H4-S-46	11.1	4.43	852	244	Smyth[142]
	C2H4-S-48	11.1	4.60	852	253	Smyth[142]
	C2H4-S-134	6.0	2.43	387	134	Markstein[97]
	C2H4-S-201	6.0	3.65	387	201	Markstein[97]
	C2H4-S-268	6.0	4.86	387	268	Markstein[97]
	C2H4-S-IDF1*	6.0	91.6	46.6	--	Makel[95]
	C2H4-S-IDF2*	6.0	45.0	23.3	--	Makel[95]
Propane	C3H8-S-27	11.1	2.57	694	213	Smyth[142]
	C3H8-S-21	11.1	1.98	4733	164	Trottier[149]
Propylene	C3H6-S-46	6.0	0.58	387	46	Markstein[97]
	C3H6-S-69	6.0	0.87	387	69	Markstein[97]

* inverse flames

Table 4.6. Laminar smoke point characteristics for methane, ethylene, propylene and propane.

Fuel	Formula	$l_s\ (m)$	$\dot{Q}_{sp}\ (W)$
Methane	CH_4	∞	--
Ethylene	C_2H_4	0.106	212
Propylene	C_3H_6	0.029	69
Propane	C_3H_8	0.162	303

4.5.4 Comparisons with experimental data

To analyse the performance of the soot model, the principal output data in coflow diffusion flames are the peak soot volume fraction and the peak integrated soot volume fraction, this latter being representative of the total soot production. It should be noted that, in IDF, these peaks are reached above the reaction zone. Ratios of computed to experimental values for the 15 flames are reported in Table 4.7.

From these results it can be observed that maximum deviations are of the order of (-)47% and (-)36% for the peak soot volume fraction and for the peak integrated soot volume fraction, respectively.

Nevertheless, the mean (absolute) deviation obtained for these values are around 27% and 11%, indicating that the numerical calculations are quite reasonable.

Table 4.7. Normalized soot volume fraction peaks and integrated soot volume fraction peaks for all the flames tested in this section. Results with more than 35% of discrepancy are shaded. (Predicted/Experiments)

Fuel	Flame	*fs* peak	Integ. peak
Methane	CH4-S-78	0.975	0.974
	CH4-S-101	0.735	0.723
Ethylene	C2H4-S-40	0.768	1.147
	C2H4-S-41	0.620	0.954
	C2H4-S-46	0.595	0.992
	C2H4-S-48	0.530	0.960
	C2H4-S-134	--	1.000
	C2H4-S-201	--	0.970
	C2H4-S-268	--	0.964
	C2H4-S-IDF1*	1.281	0.642
	C2H4-S-IDF2*	--	0.961
Propane	C3H8-S-27	0.883	1.147
	C3H8-S-21	0.706	0.688
Propylene	C3H6-S-46	--	0.987
	C3H6-S-69	--	0.809

* inverse flames

More detailed comparisons are presented hereafter, divided by each fuel used.

4.5.4.1 Methane

Figure 4.7 presents radial profiles at different heights of axial and radial velocity for the CH4-S-101 flame and temperature for both CH4-S-78 and CH4-S-101 flames. The overall predictions are in relatively good agreement with the experimental data. It can be observed that the temperature along the centreline is underestimated, especially in the lower part of the flames. In both cases the experimental "bell shape" for the upper profiles of temperature is not attained yet by the model, which suggests that the flame height is to some extend over-predicted. This trend is more pronounced for the CH4-S-101 flame.

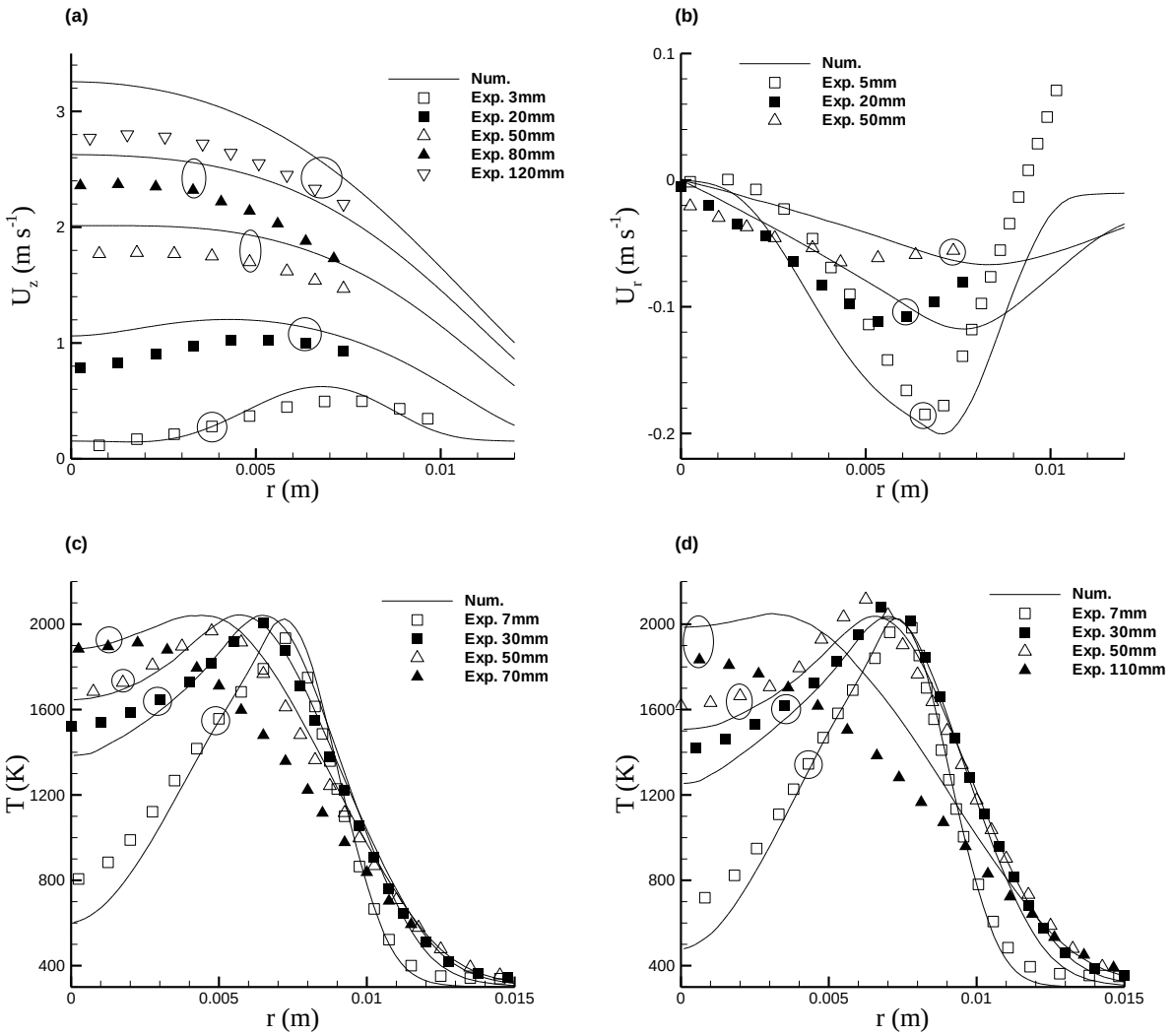

Figure 4.7. Results for the methane flames: radial profiles of the axial (a) and radial (b) velocities for the CH4-S-101 flame. Radial profiles of temperature for the CH4-S-78 flame (c) and CH4-S-101 flame (d). Experimental results from Santoro *et al.* [135].

Figure 4.8 presents the radial profiles of the soot volume fraction for both flames at different heights (Figure 4.8a and Figure 4.8b). Soot peaks are well reproduced in magnitude and in position, but they are slightly wider closer to the burner. The model fails to reproduce the soot concentration at the centreline of the flame. This behaviour was also observed in previous studies involving acetylene [88,89,54], benzene-phenyl [149] and large PAH inception models [54]. This zone is particularly low-sooting and inception-dominated, as stated by Dworkin *et al.* [38] who used an enhanced PAH growth model.

Figure 4.8 also presents the maximum soot volume fraction (Figure 4.8c) and the integrated soot volume fraction (Figure 4.8d) along the height of both methane flames. In both cases the predictions are in rather good agreement with the experiments. For the CH4-S-101 flame larger discrepancies are observed, the peak values of soot volume fraction and the integrated soot volume fraction being underestimated by factors of about 0.73 in both cases (see Table 4.7). The model does not reproduce the double peak observed experimentally for the maximum soot volume fraction, though (Figure 4.8c). This double peak is produced by a change in the radial profiles from an M-shape into a bell-

shape, in which the maximum soot volume concentration shifts from the sides of the flame to its centreline. This change in the behaviour of the soot volume fraction is observed in a more or less pronounced way in all the experimental flames. Numerically, the simulations fail to predict this double peak duo to an underestimation of the centreline values.

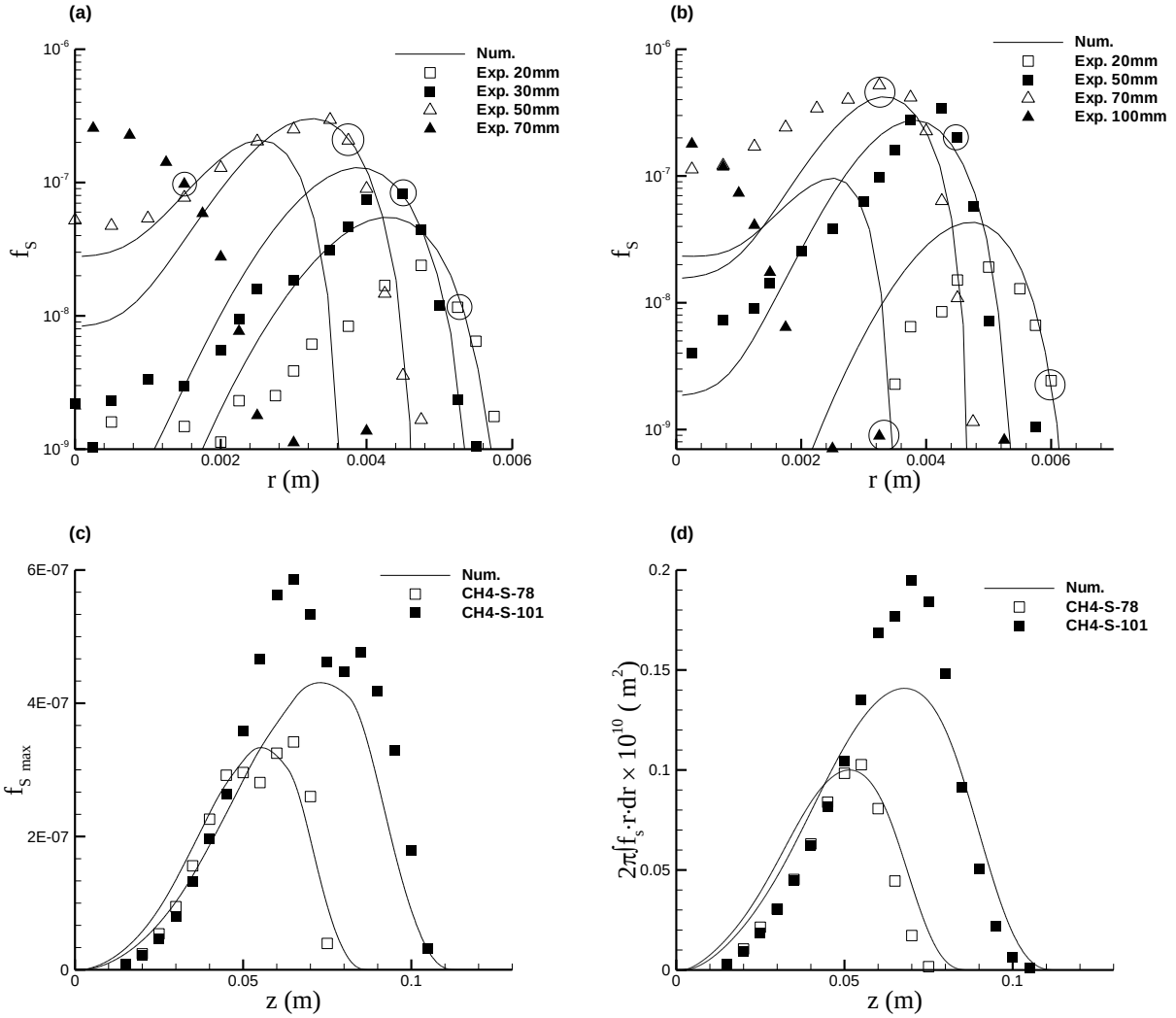

Figure 4.8. Results for the methane flames: radial profiles of the soot volume fraction for CH4-S-78 flame (a) and CH4-S-101 flame (b). Maximum soot volume fraction (c) and integrated soot volume fraction (d) along the height of both flames. Experimental results from Smyth [142].

4.5.4.2 Ethylene

Figure 4.9 presents the radial profiles of the axial and radial velocities and the radial temperature profiles for the C2H4-S-40 flame. The overall agreement between the calculations and the measurements is reasonable. The same trends as described for the methane flames are observed for the temperature profiles: the magnitude and the location of the peak are well reproduced, whereas the temperature along the centreline is under-predicted in the lower part of the flame and the flame height is slightly over-predicted.

Figure 4.10 presents the radial profiles of soot volume fraction for the flames C2H4-S-40, C2H4-S-41, C2H4-S-46 and C2H4-S-48. The predicted peaks as well as their locations are in good agreement with the experimental data. Similar to the methane flames, the soot volume fractions along the centreline are significantly under-predicted.

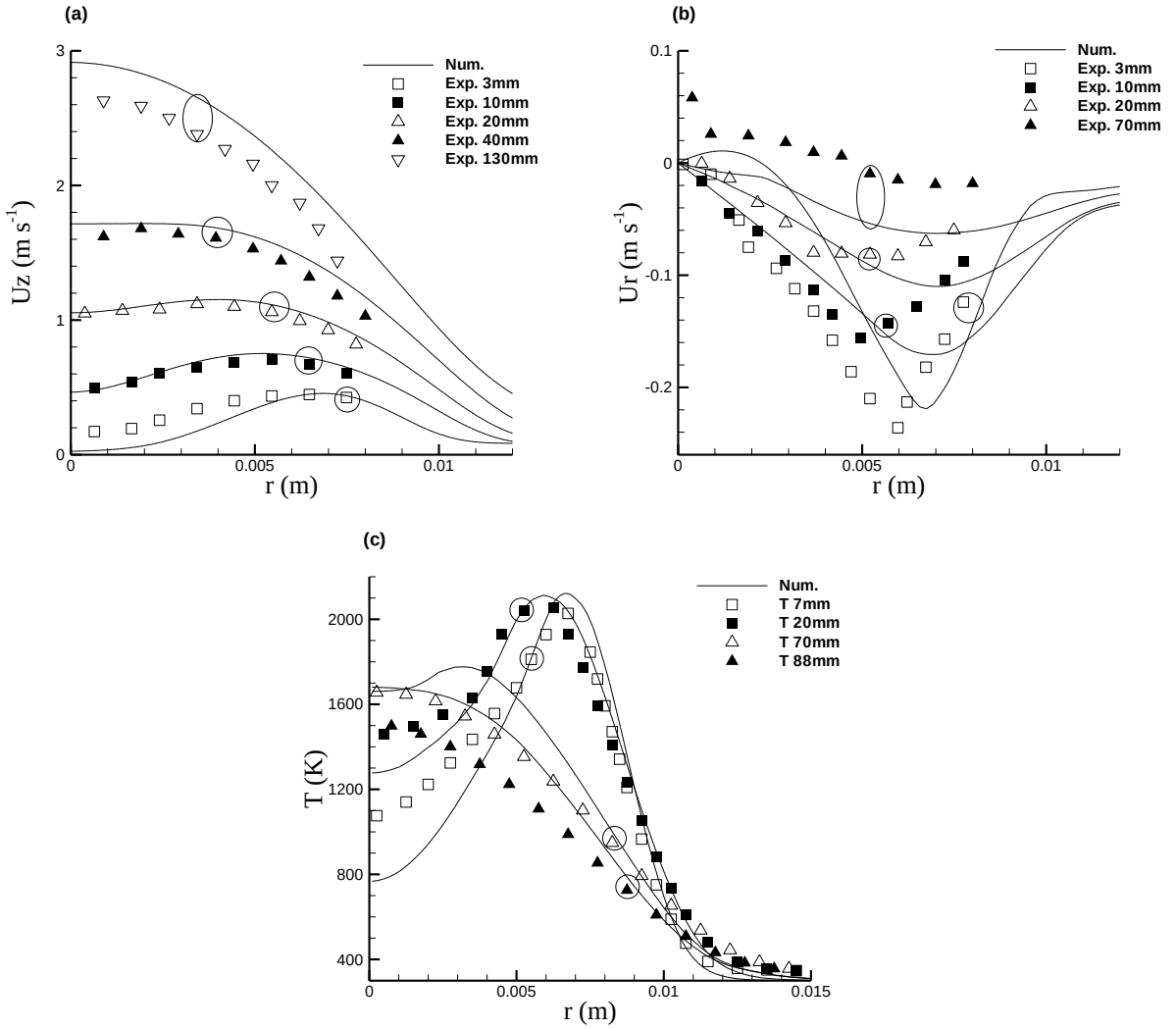

Figure 4.9. Results for the ethylene flames: radial profiles of the axial (a) and radial (b) velocity and temperature (c) for C2H4-S-40 flame. Experimental results from Santoro *et al.* [135].

Figure 4.11 presents the maximum soot volume fraction (Figure 4.11a) and the integrated soot volume fraction (Figure 4.11b) as a function of the height above the burner for the four Smyth's ethylene flames. Both of these quantities are normalized by $\dot{Q}/\dot{Q}_{sp}$ and plotted as a function of the height normalized by the flame height, $z/L_f = z/\left(l_{sp}\,\dot{Q}/\dot{Q}_{sp}\right)$; where $\dot{Q}$ is the heat release rate of the flame and $\dot{Q}_{sp}$ is the heat release rate at the smoke point. L_f is the flame height and l_s is the smoke point flame height. The heat release rates of the flames are summarized in Table 4.5, while the smoke point data is summarized in Table 4.6. This normalization is based on the fact that the flame height is proportional to the fuel flow rate [134]. This normalization allows to roughly collapse the measured maximum soot volume fraction and the integrated soot volume fraction profiles on a single curve independent of the fuel flow rate. The current predictions exhibit a scaling similar to that

of the experiments. The peak of normalized soot volume fraction is under-predicted (Figure 11a). The ratio between predicted and experimental peak of soot volume fraction ranges from 0.77 for the C2H4-S-40 flame to 0.53 for the C2H4-S-48 flame (see Table 4.7). Both computed and experimental normalized integrated soot volume fractions present an excellent agreement (see Figure 4.11b).

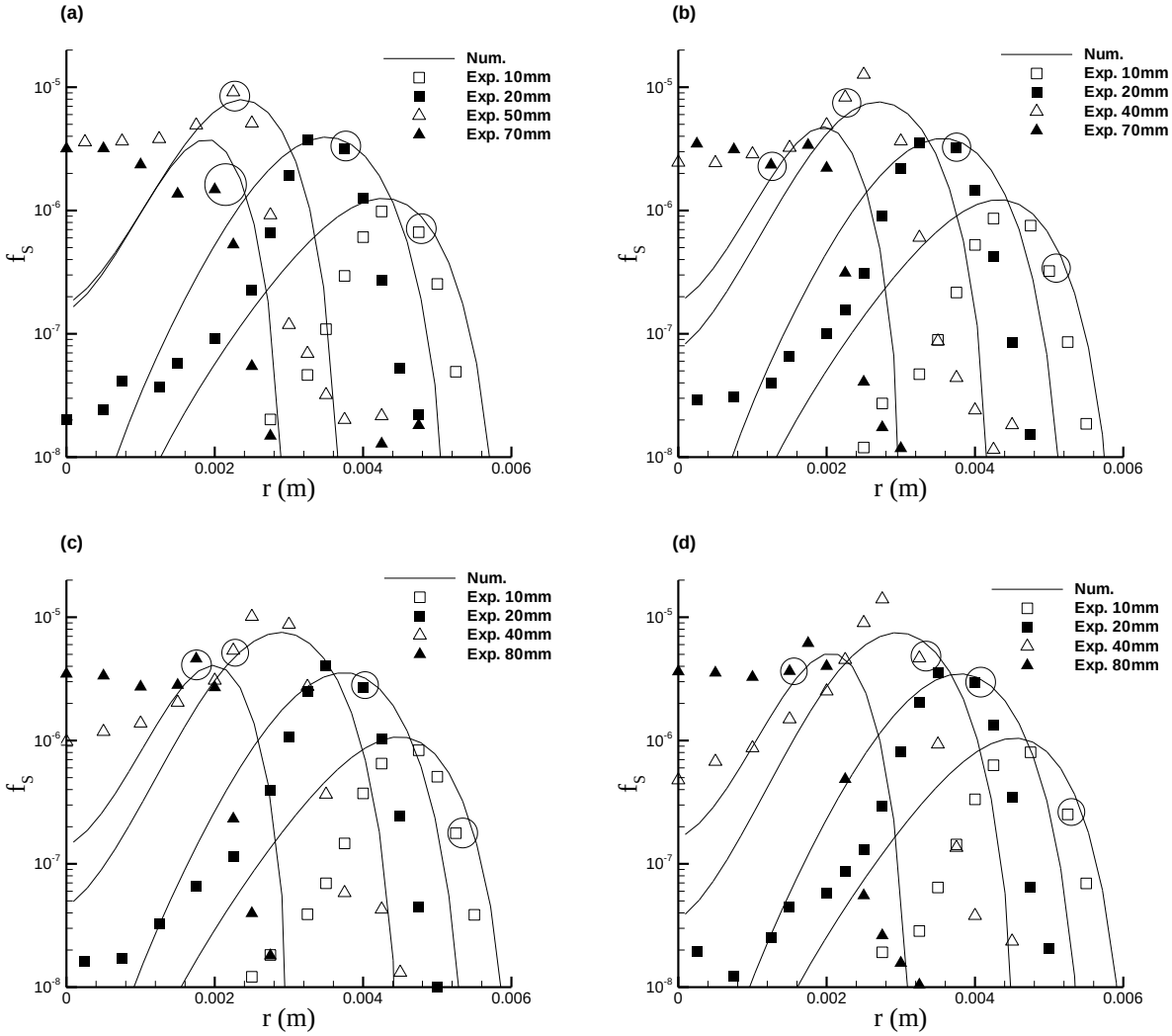

Figure 4.10. Results for the ethylene flames: radial profiles of the soot volume fraction for C2H4-S-40 (a), C2H4-S-41 (b), C2H4-S-46 (c) and C2H4-S-48 (d). Experimental results from Smyth [142].

The same analysis is carried out for the integrated soot volume fraction for the flames S-134, s-201 and S-268. For these flames the experimental values satisfy the same scaling as described before. It should be noticed that the S-268 flame deviates slightly from the collapsed results in the oxidation zone. Due to its higher fuel injection this flame is incipiently smoking, explaining the differences observed. This transition is not observed numerically, indicating that further developments should be taken for the soot oxidation process. Nevertheless, the simulations agree reasonably well to the experimental values. Peaks are in very good agreement, with ratios between predictions and measurements close to 1 (see Table 4.7).

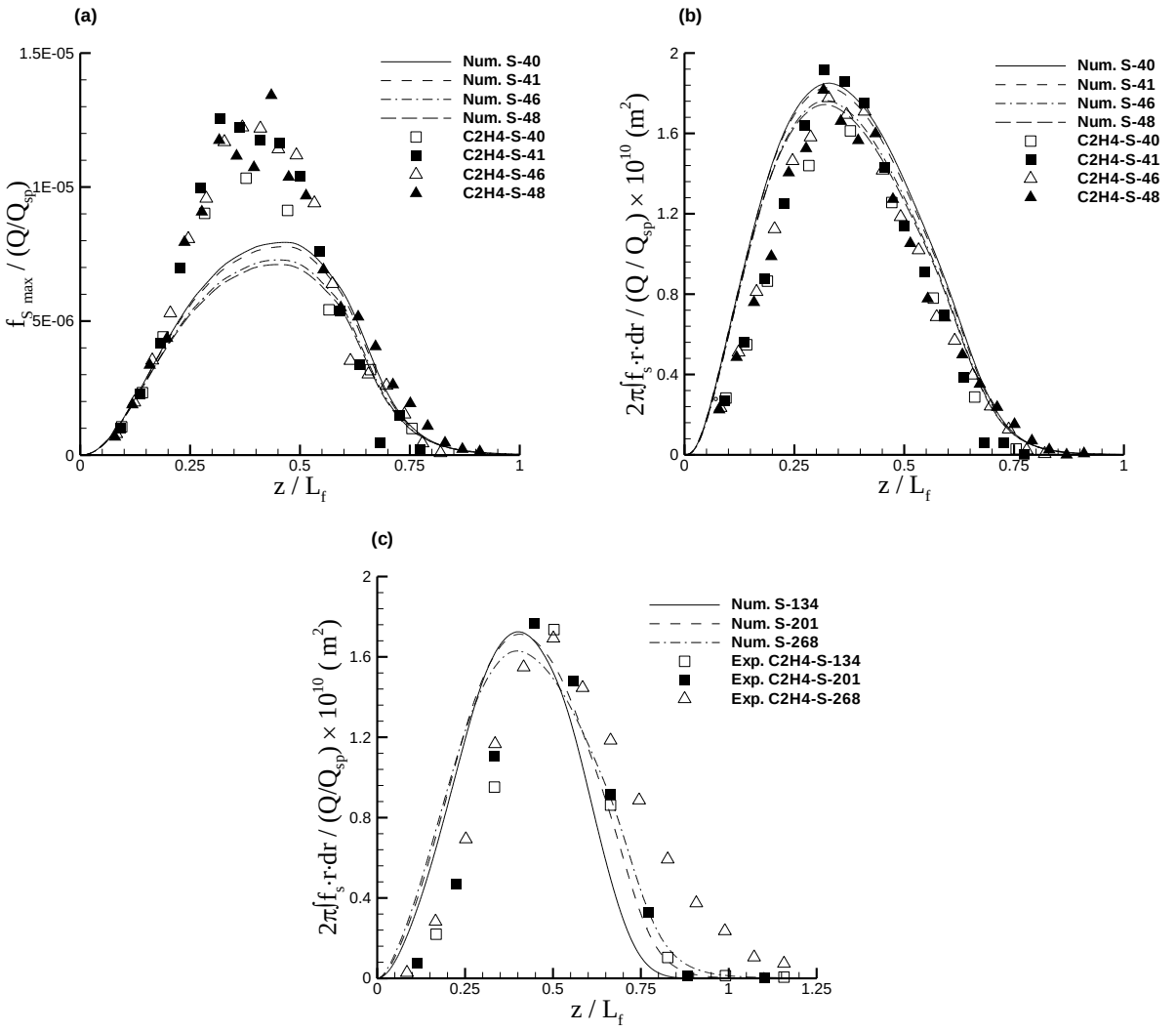

Figure 4.11. Results for the ethylene flames: maximum soot volume fraction (a) and normalized integrated soot volume fraction (b) along the normalized flame height (height above the burner/flame height) of flames C2H4-S-40, C2H4-S-41, C2H4-S-46 and C2H4-S-48. Experimental results from Smyth [142]. (c) Normalized integrated soot volume fraction along the normalized flame height of flames C2H4-S-134, C2H4-S-201 and C2H4-S-268. Experimental results from Markstein and de Ris [97].

Figure 4.12 presents the results obtained for the inverse ethylene flames. The overall agreement between the available experimental data and the simulations is reasonable. For the IDF1 flame the temperature is very well predicted near the centreline whereas it presents a slight under-prediction at the flame periphery (see Figure 4.12a). Temperature along the flame axis, for both flames (see Figure 4.12b), are also in good agreement with the experimental values. The radial profiles of soot volume fractions for the IDF1 flame (see Figure 4.12c) present also a reasonable agreement. The integrated soot volume fraction of both flames is presented in Figure 4.12d. Numerical results under-predict the integrated soot volume fraction released by the IDF1 flame, while this quantity is very well predicted for IDF2.

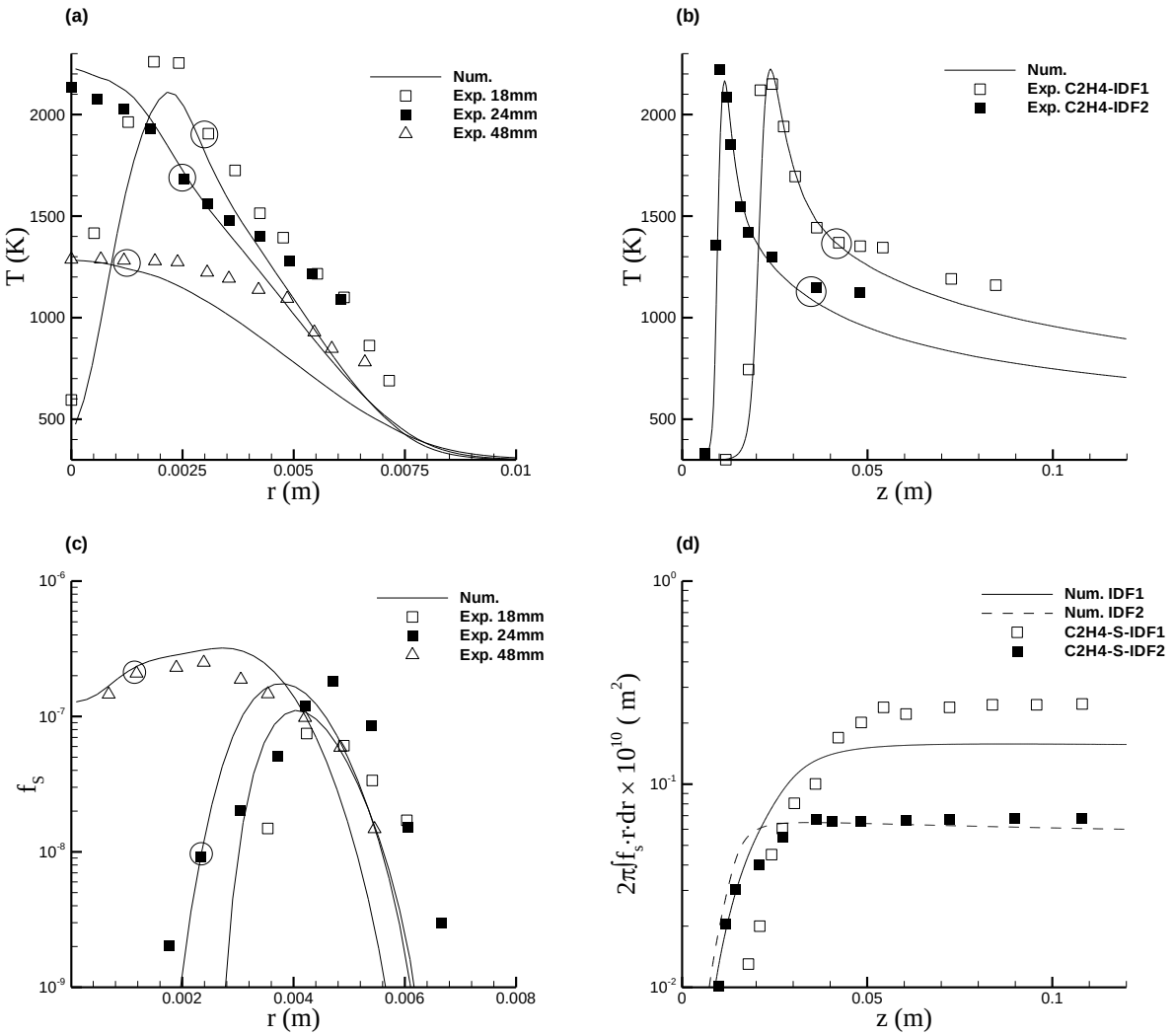

Figure 4.12. Results for the inverse ethylene flames: (a) radial profiles of temperature for IDF1, (b) axial profile of temperature along the centreline, (c) radial profiles of soot volume fraction for IDF1, and (d) integrated soot volume fraction along the height of the flames. Experimental results from Makel and Kennedy [95].

4.5.4.3 Propane

Figure 4.13a and Figure 4.13b present the radial profiles of soot volume fraction for both propane flames. The soot volume fraction is better predicted for C3H8-S-21 than for the C3H8-S-27: for both flames, at the three first heights presented, the peak location is well predicted with peak magnitudes in good agreement for C3H8-S-21, while an over-prediction is observed for C3H8-S-27. For both flames the fourth level presented is not well reproduced, failing to predict the "bell shape" observed at this level. Despite these local differences the maximum soot volume fraction and the integrated soot volume fraction along the height of the flames, Figure 4.13c and Figure 4.13d respectively, present an acceptable agreement in terms of peak location, magnitude and form. The maximum soot volume fraction obtained experimentally presents a bimodal behaviour (for the peak) that is not well reproduced by the models, but the general form is adequate. The integrated soot volume fraction presents the good general shape, with a slight overprediction for C3H8-S-27 and an underprediction for C3H8-S-21.

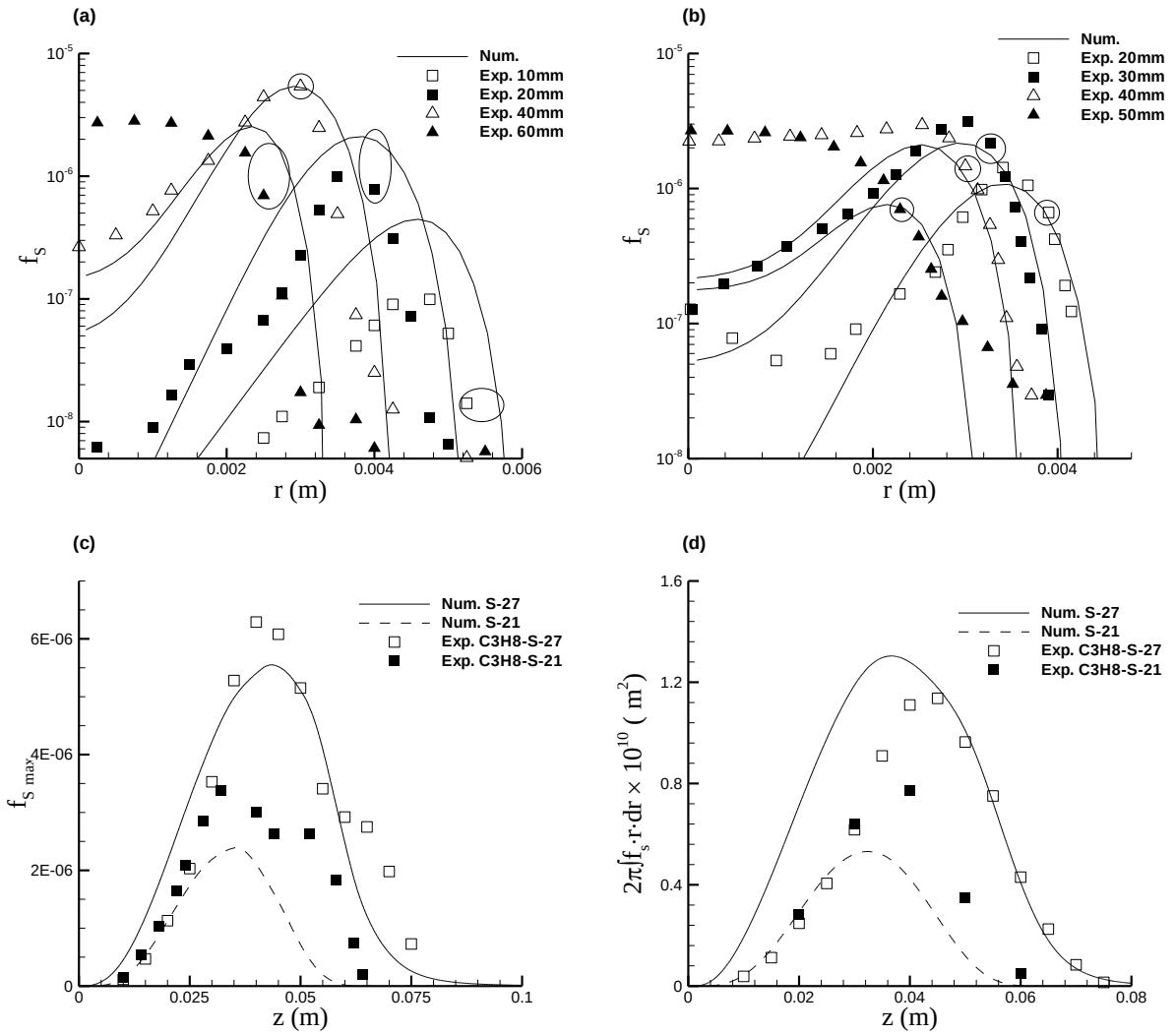

Figure 4.13. Results for the propane flames: radial profiles of soot volume fraction for C3H8-S-27 (a) and C3H8-S-21. Maximum soot volume fraction (c) and integrated soot volume fraction (d) along the height of the flames for both flames. Experimental results from Smyth [142] (C3H8-S-27) and Trottier *et al.* [149] (C3H8-S-21).

4.5.4.4 Propylene

Figure 4.14 presents the normalized integrated soot volume fraction along the normalized flame height for both of the propylene flames. For these flames the auto-similarity is observed, with the only difference that the C3H6-S-69 starts smoking and the C3H6-s-46 flame doesn't smoke. The solutions obtained for these flames are quite acceptable, with the only difficulty of predicting the smoke transition.

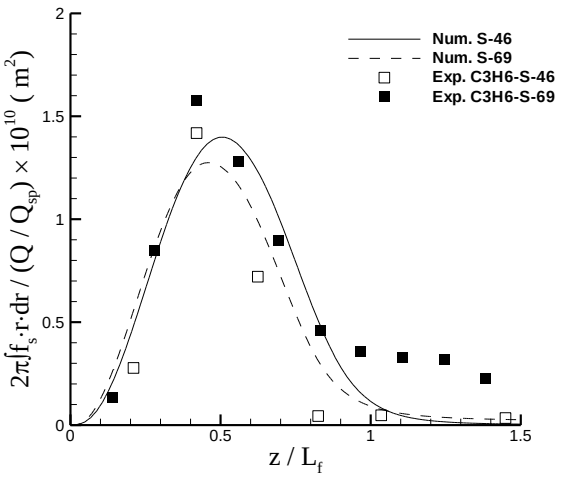

Figure 4.14. Results for the propylene flames: normalized integrated soot volume fraction along the normalized flame height (height above the burner/flame height). Experimental results from Markstein and de Ris [97].

4.6 Concluding remarks

A numerical study of laminar diffusion flames was carried out, first considering and assessing several radiation property models in order to quantify its effects, in a decoupled and in a coupled way. Then, the study pointed into the search of an appropriate and robust soot model, capable of predicting acceptable results for a wide range of fuels normally used. The main conclusions of this study can be summarized as follows:

- Comparisons between the experimental data and the numerical solutions obtained with the SNBCK model show a fairly good agreement.
- The contribution of CO in radiation can be ignored.
- Gas and soot reabsorptions are crucial features for accurately estimating the radiative losses, and then temperature and soot volume fractions. Consequently the OTA leads to inaccurate predictions for heavily sooting flames, especially in the upper part of them.
- The spectral nature of gas and soot is a crucial feature to obtain reliable predictions. Therefore the use of grey models and the GWB model should be avoided if accurate solutions are desired.
- The FSCK provides similar results as compared to the SNBCK with a substantial gain in CPU time. Therefore it is a good alternative to be implemented in order to study soot formation processes.
- Predicted soot volume fractions are very sensitive to the radiative property model used, especially in the zone where the soot is oxidized. In particular the amount of soot released by the smoking flame is highly dependent of the radiative model. As a consequence, numerical studies concerning soot formation/oxidation processes should consider an accurate radiation model.

- The soot model proposed by Liu *et al.* [89] predicts accurately the sooting behaviour of the Santoro's smoking (S) and non-smoking (NS) flames. Unfortunately, this model was found to be limited to these two cases.
- The soot model presented in section 4.5.1 predicts results in acceptable agreement for a wide range of fuels and conditions. Two set of parameters were necessary to obtain a satisfactory agreement, one for the C1-C2 hydrocarbons and another for the C3 hydrocarbons. Nevertheless these two sets differ only by the value of the pre-exponential factor in the surface growth term.
- This soot model, as other acetylene-based semi-empirical model, fails to predict the soot volume fraction at the centreline of the domain, although the maximum soot volume fractions and the (radially) integrated soot volume fraction along the flame height present an overall satisfactory agreement.
- This soot model is judged sufficiently robust to be applied for simulating turbulent diffusion flames.

5 Modelling thermal radiation from turbulent diffusion flames

This chapter is dedicated to modelling the thermal radiation from turbulent diffusion flames. The main difficulty in modelling the radiative heat transfer in this kind of flames, besides the difficulty coming from modelling the spectral nature of gaseous species and soot, arises from the Turbulence-Radiation Interactions (TRI). The turbulent fluctuations of scalars, such as the temperature, the species mole fraction and the soot volume fraction, affect the radiative heat transfer and vice versa. Normally these interactions are ignored or treated in an oversimplified manner in CFD simulations [143]. However, these approximations can have a serious impact on predictions.

Two sections are considered in this chapter: in the first, 5 laboratory-scaled pool fires are modelled considering different heat release rates, 3 for propane-air flames and 2 for methane-air flames. These fuels can be considered as moderately sooting for the propane flames and slightly sooting for the methane flames. Comparisons with experimental data consider not only the radiative flux on remote surfaces, but also mean and fluctuating velocities and temperatures, mean molar concentrations and soot volume fractions. Grey gas and soot approximations are also tested in order to quantify its effects in the studied flames. The second section considers the modelling of two large-scale methane pool fires. Radiant fractions and radiative fluxes on remotes surfaces are compared to experimental values. In this section several TRI considerations are tested in order to quantify different TRI modelling and different levels of closure.

The flames are all simulated using a turbulent buoyancy-modified k-ε model and the Steady Laminar Flamelet (SLF) model is used to describe combustion. Based on the results presented in the last chapters the FSCK model is chosen as the radiative property model considered for estimate the radiative heat transfer. A semi-empirical two-equation soot model, presented in the previous chapter, is considered for modelling the soot. TRI is modelled on the basis of the Optically Thin Fluctuation Approximation (OTFA), with the emission term and the mean absorption coefficient being closed by using a presumed probability density function (PDF) of the mixture fraction, the scalar dissipation rate and the enthalpy defect.

The present work led to the publication in an international journal, some conferences and in an open access journal [21,22,23].

5.1 Flow field models

A turbulent version of the CFD code used in the previous chapter is used for simulating the different buoyant turbulent diffusion flames. The radiative property model (FSCK) and the semi-empirical two-equation soot model tested previously on laminar flames are implemented into this CFD code. Turbulence-Radiation Interactions are also implemented in order to account for these effects.

The mean gas flow field is modelled by the Favre-averaged Navier–Stokes (FANS) equations closed by a buoyancy-modified k-ε model with algebraic stress/flux models (ASM/AFM). The Steady Laminar Flamelet (SLF) model is coupled to a presumed PDF approach to account for Turbulence-Chemistry Interactions.

5.1.1 Transport equations

The solution includes the overall continuity equation, the Navier–Stokes equations using a low Mach number formulation, and transport equations for the mixture fraction, $\tilde{\xi}$, the mixture fraction variance, $\widetilde{\xi''^2}$, the turbulent kinetic energy, k, the turbulent dissipation, ϵ, the soot mass fraction, $\tilde{Y}_S$, the soot number density per unit mass of mixture, $\tilde{N}_s$, the total enthalpy, $\tilde{h}$, and the adiabatic enthalpy, $\tilde{h}_{ad}$. The generalized Favre-averaged conservation equation in axisymmetric cylindrical coordinates (*r, z*) for a dependent variable Φ can be written as:

$$\frac{\partial}{\partial t}\left(\bar{\rho}\tilde{\Phi}\right)+\frac{1}{r}\frac{\partial}{\partial r}\left(r\bar{\rho}\tilde{u}_r\tilde{\Phi}\right)+\frac{\partial}{\partial z}\left(\bar{\rho}\tilde{u}_z\tilde{\Phi}\right)=\frac{1}{r}\frac{\partial}{\partial r}\left(r\Gamma_{\Phi_r}\frac{\partial\tilde{\Phi}}{\partial r}\right)+\frac{\partial}{\partial z}\left(\Gamma_{\Phi_z}\frac{\partial\tilde{\Phi}}{\partial z}\right)+\bar{S}_\Phi \tag{77}$$

The variable Φ, the source terms S_Φ and the effective exchange coefficients Γ_{Φ_i} are listed in Table 5.1.

5.1.2 Turbulence model

A buoyancy-modified k-ε turbulence model is used in the simulations. The shear and buoyancy productions of turbulence are expressed by:

$$P=-\bar{\rho}\widetilde{u_i''u_j''}\frac{\partial\tilde{u}_i}{\partial x_j} \tag{78}$$

$$G=-\overline{u_i''}\left(\frac{\partial p_d}{\partial x_i}+\rho_\infty g_i\right) \tag{79}$$

where p_d represents the hydrodynamic pressure associated with the fluid motion (since the hydrostatic pressure is taken into account through the reference density ρ_∞, which is equal to the density of the ambient air). Introducing $\overline{u_i}=\tilde{u}_i+\overline{u_i''}$ into $\overline{\rho u_i}=\bar{\rho}\overline{u_i}+\overline{\rho' u_i'}$ and using the definition of the Favre average velocity $\bar{\rho}\tilde{u}_i=\overline{\rho u_i}$ leads to $\overline{u_i''}=-\overline{\rho' u_i'}/\bar{\rho}$. This latter equation can be expressed as $\overline{u_i''}=-1/\bar{\rho}\left(\partial\bar{\rho}/\partial\tilde{T}\right)\overline{u_i'T'}=\beta\overline{u_i'T'}$ by applying the ideal gas law [157], where $\beta=-1/\bar{\rho}\left(\partial\bar{\rho}/\partial\tilde{T}\right)$ is the thermal expansion factor. Finally the common approximation that $\overline{u_i'T'}\approx\widetilde{u_i''T''}$ is used in the calculations, leading to:

$$G=-\beta\widetilde{u_i''T''}\left(\frac{\partial p_d}{\partial x_i}+\rho_\infty g_i\right) \tag{80}$$

The turbulent heat flux is modelled by a second-order algebraic expression derived from its parent transport equation [56,87,166]:

$$\widetilde{u_i''T''}=-C_t\frac{k}{\epsilon}\left[\widetilde{u_i''u_j''}\frac{\partial\tilde{T}}{\partial x_j}+\eta_1\widetilde{u_j''T''}\frac{\partial\tilde{u}_i}{\partial x_j}+\eta_2\beta g_i\widetilde{T''^2}\right] \tag{81}$$

The common approximations that $\overline{u_i'u_j'}\approx\widetilde{u_i''u_j''}$ and $\overline{u_i'T'}\approx\widetilde{u_i''T''}$ have been used in this last equation. The formulation of Davidson is used to model the turbulent Reynolds stresses [25]. The

standard Eddy-Viscosity Model (EVM) is considered in order to model the shear stresses due to strain, whereas an Algebraic Stress Model (ASM) is used to account for the anisotropy of turbulence due to buoyancy effects.

Table 5.1. Summary of the transport equations solved in the turbulent simulations.

Equation for:	Φ	Γ_{Φ_i}	S_Φ
Continuity	1	0	0
Axial Momentum	$\tilde{u}_z$	μ_{eff}	$-\frac{\partial \tilde{p}_d}{\partial z} + (\bar{\rho} - \rho_\infty) g_z + \frac{1}{r}\frac{\partial}{\partial r}\left(r\mu_{eff}\frac{\partial \tilde{u}_r}{\partial z}\right) + \frac{\partial}{\partial z}\left(\mu_{eff}\frac{\partial \tilde{u}_z}{\partial z}\right) - \frac{2}{3}\frac{\partial}{\partial z}\left[\mu_{eff}\left(\frac{1}{r}\frac{\partial (r\tilde{u}_r)}{\partial r} + \frac{\partial \tilde{u}_z}{\partial z}\right) + \bar{\rho}k\right]$
Radial Momentum	$\tilde{u}_r$	μ_{eff}	$-\frac{\partial \tilde{p}_d}{\partial r} + \frac{1}{r}\frac{\partial}{\partial r}\left(r\mu_{eff}\frac{\partial \tilde{u}_r}{\partial r}\right) + \frac{\partial}{\partial z}\left(\mu_{eff}\frac{\partial \tilde{u}_z}{\partial r}\right) - \frac{2}{3}\frac{\partial}{\partial r}\left[\mu_{eff}\left(\frac{1}{r}\frac{\partial (r\tilde{u}_r)}{\partial r} + \frac{\partial \tilde{u}_z}{\partial z}\right) + \bar{\rho}k\right]$
Turbulent Kinetic Energy	k	$\mu + \frac{\mu_t}{\sigma_k}$	$P + G - \bar{\rho}\epsilon$
Turbulent Dissipation	ϵ	$\mu + \frac{\mu_t}{\sigma_\epsilon}$	$C_{\epsilon 1}\frac{\epsilon}{k}P - \bar{\rho}C_{\epsilon 2}\frac{\epsilon^2}{k} + C_{\epsilon 3}\frac{\epsilon}{k}G$
Enthalpy	$\tilde{h}$	$\frac{\mu}{Pr} + \frac{\mu_t}{\sigma_t}$	$-\overline{\nabla \cdot q_R''}$
Adiabatic Enthalpy	$\tilde{h}_{ad}$	$\frac{\mu}{Pr} + \frac{\mu_t}{\sigma_t}$	0
Mixture Fraction	$\tilde{\xi}$	$\frac{\mu}{Sc} + \frac{\mu_t}{\sigma_t}$	0
Mixture Fraction Variance	$\widetilde{\xi''^2}$	$\frac{\mu}{Sc} + \frac{\mu_t}{\sigma_t}$	$C_{v1}\mu_t\left[\frac{\partial \tilde{\xi}}{\partial r}\frac{\partial \tilde{\xi}}{\partial r} + \frac{\partial \tilde{\xi}}{\partial z}\frac{\partial \tilde{\xi}}{\partial z}\right] - C_{v2}\bar{\rho}\frac{\epsilon}{k}\widetilde{\xi''^2}$
Soot Mass Fraction	Y_s	$\frac{\mu_t}{\sigma_f} - \rho V_{T,i}$	$\bar{S}_m$
Soot Number Density	N_s	$\frac{\mu_t}{\sigma_f} - \rho V_{T,i}$	$\bar{S}_N$

$Pr = \mu C_p/\lambda\,, \quad Sc = \mu/\rho D\,, \quad \mu_t = \rho C_\mu k^2/\epsilon\,, \quad \mu_{eff} = \mu + \mu_t$

$$\widetilde{u_i'' u_j''} = \left(\widetilde{u_i'' u_j''}\right)_{EVM} + \left(\widetilde{u_i'' u_j''}\right)_{ASM} \tag{82}$$

where

$$\left(\widetilde{u_i'' u_j''}\right)_{EVM} = \frac{2}{3}\delta_{ij}\left(k + \frac{\mu_t}{\bar{\rho}}\frac{\partial \tilde{u}_k}{\partial x_k}\right) - \frac{\mu_t}{\bar{\rho}}\left(\frac{\partial \tilde{u}_i}{\partial x_j} + \frac{\partial \tilde{u}_j}{\partial x_i}\right) \tag{83}$$

$$\left(\widetilde{u_i'' u_j''}\right)_{ASM} = \frac{k}{\epsilon}\frac{(1 - C_2)}{C_1}\left(G_{ij} - \frac{2}{3}\delta_{ij}G\right) \tag{84}$$

In the latter equation G_{ij} is given by $G_{ij} = \left(\beta g_j \widetilde{u_i'' T''} + \beta g_i \widetilde{u_j'' T''}\right)$. The constants of the turbulence model are summarized in Table 5.2.

Table 5.2. Turbulent constants and model parameters [87,166]

$C_{\varepsilon 1}$	$C_{\varepsilon 2}$	$C_{\varepsilon 3}$	C_t	η_1	η_2	C_1	C_2	C_{v1}	C_{v2}	σ_k	σ_ϵ	σ_t
1.44	1.92	1.3	0.28	0.6	0.6	1.8	0.6	2.8	2.0	0.85	1.3	0.85

5.1.3 Turbulence-Combustion interactions

The SLF model is used to obtain state relationships for density, species concentrations and temperature as unique functions of the conserved scalar ξ (mixture fraction), of the scalar dissipation rate, $\chi = 2D_{th}(\nabla\xi \cdot \nabla\xi)$, and of an enthalpy defect parameter, $X_R = (h - h_{ad})/(h_u - h_{ad})$, in the same way as was done in the preceding chapter. The flamelet library is generated using a full chemical kinetic scheme presented by Qin *et al.* [129], consisting of 70 species and 463 reactions, optimized on the oxidation of C3 hydrocarbon species.

Statistical moments for scalar quantities can then be computed from the flamelet library and a joint PDF of the mixture fraction, scalar dissipation rate and the enthalpy defect parameter. Favre and Reynolds averaged quantities are then computed as:

$$\tilde{\varphi} = \int_0^1 \int_0^\infty \int_0^1 \varphi^{fl}(\xi;\chi;X_R)\ \tilde{P}(\xi;\chi;X_R)\, d\xi\, d\chi\, dX_R \tag{85}$$

$$\bar{\varphi} = \bar{\rho} \int_0^1 \int_0^\infty \int_0^1 \frac{\varphi^{fl}(\xi;\chi;X_R)}{\rho^{fl}(\xi;\chi;X_R)} \tilde{P}(\xi;\chi;X_R)\, d\xi\, d\chi\, dX_R \tag{86}$$

Assuming the statistical independence of ξ, χ and X_R: $\tilde{P}(\xi;\chi;X_R) = \tilde{P}(\xi)\tilde{P}(\chi)\tilde{P}(X_R)$. The joint PDF is modelled then as the product of a Beta distribution function for the mixture fraction and two Dirac functions for both the scalar dissipation rate [58] and the enthalpy defect parameter [10].

$$\tilde{\varphi} = \int_0^1 \int_0^\infty \int_0^1 \varphi^{fl}(\xi;\chi;X_R)\, \tilde{P}(\xi)\delta(\chi - \tilde{\chi})\delta\left(X_R - X_{R,mean}\right) d\xi\, d\chi\, dX_R \tag{87}$$

where $\tilde{\chi} = C_{v2}\frac{\epsilon}{k}\widetilde{\xi''^2}$ and $X_{R,mean}$ are the local mean values of the scalar dissipation rate and of the heat loss fraction, respectively. $X_{R,mean}$ is computed as proposed by Brookes and Moss [10]. It should be stated that, unlike turbulent jet flames, laboratory-scale buoyant diffusion flames generally are characterized by low scalar dissipation rates and combustion reactions are consequently closer to the equilibrium.

5.1.4 Soot model

The two-equation semi-empirical soot model described in the previous chapter is used for simulating the turbulent diffusion flames. Only acetylene is considered as soot precursor, leading to $k_{1'} = 0$ in the set of constants given in Table 4.4. This difference arises from the fact that this study was carried out before the evaluation of the soot model reported previously.

The soot constant rates used are given in Table 5.3. The number of carbon atoms in the incipient soot particle and the agglomeration rate are fixed to $C_{min} = 60$ and $C_a = 3$, respectively. The OH collision efficiency factor is fixed to 0.08 instead of 0.2.

Table 5.3. Reaction rate constants for soot formation in the form of an Arrhenius expression, $k_j = A\,T^b \exp(-T_a/T)$ (Units in K, kmol, m, s).

k_j	A	b	T_a	Ref.
k_1	0.63×10^4	0	21000	[80]
k_2	0.75×10^3	0	12100	[156]
k_4	1.27×10^3	-0.5	0	[117]

Production/destruction source terms for the soot mass fraction and soot number density have been stored in the flamelet library as described by Carbonell *et al*. [11] as in the previous chapter. Mean source terms are then computed by using the uncorrelated approach proposed by Brookes and Moss [10], ignoring the correlation between gaseous and soot properties. The study of Brookes and Moss showed that this formulation requires the application of a scaling factor on the mean oxidation rate to reproduce the soot volume fraction with a satisfactory level of accuracy [10]. In the present study the scaling factor was adjusted to reproduce approximately the overall soot yield measured in the overfire region of buoyant turbulent diffusion flames fuelled by propane (0.012 g of soot per g of fuel carbon [68]). For methane flames the scaling factor was kept unchanged. This clearly raises the difficulty encountered for the turbulent closure of terms involving both a gaseous-related part and a particle-related part. The same difficulty arises in the closure of the TRI-emission term where the soot volume fraction-temperature correlation is involved. Improvements are required in order to have a full closure of these terms. This will be discussed in the conclusion as perspective for future works.

5.1.5 Radiation model

Coupled radiative heat transfer calculations are considered, using the FSCK model for estimating the spectral gas and soot radiation. In order to keep the computational cost compatible with applications, the k-distributions are obtained from the Mixed Narrow Band (MNB) database pre-generated from the 43 narrow band database of Soufiani and Taine [146], mixed and assembled using the schemes of Modest and Riazzi [114] and using 5 Gauss-Legendre quadrature points (described in Chapter 2). The spectral soot absorption coefficient constant is fixed to 4.9 which is consistent with the complex index values of refraction of soot, $m = 1.57 - 0.56i$, commonly used for reporting soot volume fraction measurements in flames.

The reference state is determined here by the molar fractions of the gas species and by the soot volume fraction averaged over the flame volume V_f, defined as the part of the computational domain where the mean temperature is greater than 500 K. It was found that modifying this threshold in the range 400-600 K does not alter the results. In agreement with a previous study [21], the reference temperature is computed as a time-averaged emission-weighted temperature:

$$T_0 = \frac{\iiint_{V_f} \overline{\kappa_P T^5} dV}{\iiint_{V_f} \overline{\kappa_P T^4} dV} \tag{88}$$

5.1.6 Turbulence-Radiation Interactions

The radiative transfer equation (RTE), defined as in Chapter 2, is strictly applicable to instantaneous quantities only, which can fluctuate in a turbulent flow. For the other side only time averaged quantities and their mean square fluctuations are provided by the turbulence model. Therefore, time averaging the RTE gives:

$$\frac{d\overline{I_g}}{ds} + \underbrace{\overline{k^*\left(T_0, \underline{\phi}, g_0\right) I_g}}_{Absorption\ TRI} = \underbrace{\overline{k^*\left(T_0, \underline{\phi}, g_0\right) a(T, T_0, g_0) I_b(T)}}_{Emission\ TRI} \tag{89}$$

The absorption term, which can be expressed as $\overline{k^* I_g} = \overline{k^*}\,\overline{I_g} + \overline{k^{*\prime} I_g'}$, raises a difficulty. Its modelling requires a detailed knowledge of the instantaneous fields of the radiative participating species and temperature [18,19,104,105,153]. The absorption coefficient–incident intensity correlation, $\overline{k^{*\prime} I_g'}$, is usually neglected based on the consideration that, if the mean free path for radiation is much larger than the turbulence length scale, then the local radiative intensity is weakly correlated with the local absorption coefficient. This approximation, commonly referred as the Optically Thin Fluctuation Approximation (OTFA) was found to be valid for a wide range of conditions [18,19,21,104,105,153], with the exception of very large-scale sooting jet flames where TRI was found to reduce absorption by about 10% [103].

The emission term is determined on the basis of local properties only. This term is evaluated using a presumed PDF in the same way as presented in equation (**87**). Mean values of the absorption coefficient and of the emission term are computed as:

$$\overline{k^*} = \bar{\rho} \int_0^1 \int_0^1 \int_0^\infty \int_0^1 \frac{k^{fl}(\xi, \chi, X_R, f_s)}{\rho^{fl}(\xi, \chi, X_R)} \tilde{P}(\xi, \chi, X_R, f_s) d\xi\, d\chi\, dX_R\, df_s \tag{90}$$

$$\overline{k^* a I_b} = \bar{\rho} \int_0^1 \int_0^1 \int_0^\infty \int_0^1 \frac{k^{fl}(\xi, \chi, X_R, f_s) a^{fl}(\xi, \chi, X_R) I_b^{fl}(\xi, \chi, X_R)}{\rho^{fl}(\xi, \chi, X_R)} \tilde{P}(\xi, \chi, X_R, f_s) d\xi\, d\chi\, dX_R\, df_s \tag{91}$$

where the PDF is expressed as $\tilde{P}(\xi, \chi, X_R, f_S) = \tilde{P}(\xi)\delta(\chi - \tilde{\chi})\delta\left(X_R - X_{R,mean}\right)\delta\left(f_S - \widetilde{f_S}\right)$, disregarding the influence of the fluctuations of the soot volume fraction.

This approximation does not affect the mean absorption coefficient since it depends linearly on the soot volume fraction. However, it may alter the evaluation of emission TRI since the soot absorption coefficient–Planck function correlation, i.e. the soot volume fraction–temperature correlation, is ignored. This approximation is not expected to have a significant effect in the case of methane flames for which gas radiation dominates. Its effects on more heavily sooting flames can be assessed qualitatively on the basis of the limited works reported in the literature. Experimental [119,137,138] and numerical [65] studies found that the soot volume fraction and temperature are negatively correlated in the underfire region of both buoyant and jet turbulent diffusion flames. The spectral time-average soot emission term can be approximated by the equation [19]:

$$\overline{\kappa_{\eta,S} I_{b\eta}} \approx \overline{\kappa_{\eta,S}} I_{b\eta}(\bar{T}) + \overline{\kappa_{\eta,S}} \frac{\overline{T'^2}}{2} \left(\frac{\partial^2 I_{b\eta}}{\partial T^2} \right)_{T=\bar{T}} + \overline{\kappa'_{\eta,S} T'} \left(\frac{\partial I_{b\eta}}{\partial T} \right)_{T=\bar{T}} \quad (92)$$

The second term on the right-hand side is positive, i.e. the temperature fluctuations contribute to the enhancement of soot emission. The third term is negative since the spectral absorption coefficient and temperature are expected to be negatively correlated. This term thus reduce the effects of the temperature fluctuations and may decrease the radiation emitted by the soot. [19]. Consequently, the greater the absolute value of the soot volume fraction–temperature correlation, the lower the increase in soot emission due to TRI is expected to be. A recent numerical analysis, relative to ethylene jet flames, showed that the increase in soot emission due to TRI is much lower in the case of large-scale flames than for laboratory-scale flames. This suggests therefore that the effects of the correlation between soot volume fraction and temperature become really significant in large-scale flames [103]. However, further investigations are required to confirm the validity of this analysis and to provide quantitative estimations of the influence of this correlation on radiative predictions.

5.1.7 Numerical resolution

The same numerical resolution considerations, used in the resolution of the laminar diffusion flames, are considered in this chapter (see Numerical resolution section in the previous chapter). However, a higher number of control angles, 36x48, are considered for the estimation of the radiative quantities. This change is based on preliminary calculations in which grid-independent solutions are obtained [21].

5.2 Modelling laboratory-scale pool fires

This section focuses on the numerical modelling of radiative heat transfer in laboratory-scale buoyant turbulent diffusion flames, in particular seeking to correctly estimate its radiative flux on remote surfaces. Three propane burner experiments and two methane burner experiments are simulated and compared against experimental measurements.

5.2.1 Propane flames

5.2.1.1 Flame configurations

Three propane flames in open conditions are simulated. These flames, experimentally studied by Gengembre and coworkers [47,147], were generated from a propane burner of 0.3 m in diameter with heat release rates (HRR, $\dot{Q}$) of 15.8, 22.9 and 37.9 kW. Gengembre *et al*. reported experimental data concerning the flame structure such as major species concentrations, mean values of temperature and axial velocity, and the root mean square (r.m.s.) values of temperature fluctuations and of axial and radial velocity fluctuations [47]. The work of Souil *et al*. focused on thermal radiation with measurements of the overall radiant fraction ($\chi_R = \dot{Q}_R/\dot{Q}$) and of vertical radiative flux distributions at a distance of 0.30 m and 0.40 m from the centre of the burner [147]. These experimental data were used before by Snegirev to validate a grey radiative model based on a statistical Monte Carlo method and on Planck-mean absorption coefficients for gas and soot [143].

The overall computational domain is $2m\,(R) \times 4m\,(L)$. A preliminary grid refinement study indicated that a non-uniform mesh with 70×166 cells and a mesh size of $1cm \times 1cm$ in the flaming zone is sufficient to achieve a grid-independent solution. Initial and boundary conditions are summarized in Table 5.4. The flow is assumed to be laminar at the burner exit.

Table 5.4. Initial and boundary conditions.

Initial conditions	
	$u = 0\ m\ s^{-1}, \quad T_\infty = 300\ K, \quad Y_S = 0, \quad N_S = 0, \quad \xi = 0, \quad \widetilde{\xi''^2} = 10^{-6},$ $k = \epsilon = 10^{-6}, \quad Y_\alpha = 0$ except $Y_{O_{2,\infty}} = 0.232$ and $Y_{N_{2,\infty}} = 0.768, \quad p = p_\infty$
Boundary conditions	
Ground	$\tilde{u}_r = \tilde{u}_z = 0, \quad \partial\varphi/\partial n = 0$
Symmetry Plane	$\tilde{u}_r = 0, \quad \partial\varphi/\partial n = 0$
Free Boundary	$p = p_\infty, \quad \partial\tilde{u}_i/\partial n = 0$ $\quad if\ u_n > 0$ then outflow: $\partial\varphi/\partial n = 0$ $\quad if\ u_n < 0$ then inflow: $\varphi = \varphi_\infty$
Burner exit	$\partial p/\partial n = 0, \quad \tilde{u}_r = 0, \quad \tilde{u}_z = u_{inj}, \quad k = \epsilon = 10^{-6}$ $\rho_{inj} u_{inj} \varphi_{inj} = \rho_{inj} u_{inj} \varphi - \Gamma(\partial\varphi/\partial n)$

5.2.1.2 Comparison with available data

Comparisons with experimental data along the axis are presented in Figure 5.1. The zones of the continuous flame (CF) and the intermittent flame (IF) are also indicated in this figure. The scaling factors proposed by McCaffrey [98] are used for plotting this figure: distance and velocity are scaled by $\dot{Q}^{2/5}$ and $\dot{Q}^{1/5}$ respectively. McCaffrey [98], Cox and Chitty [24] and Gengembre *et al*. [47] found that this scaling can reduce the centreline variation of mean temperature, mean velocity and r.m.s. values of temperature and velocity fluctuations to a single curve independent of the HRR. Figure 5.1 shows that the current predictions exhibit a scaling similar to that of the experiments. In addition the delimitations of the different regions, i.e. the CF region for $z/\dot{Q}^{2/5} < 0.08$, the IF region for $0.08 < z/\dot{Q}^{2/5} < 0.2$ and the thermal plume region for $z/\dot{Q}^{2/5} > 0.2$ are captured rather well.

Temperature rise ($\Delta T = T - T_\infty$) and normalized mean axial velocity ($u_z^* = \widetilde{u_z}/\dot{Q}^{1/5}$) along the axis are in satisfactory agreement with the experimental data (see Figure 5.1a and Figure 5.1b). In order to facilitate the reading of Figure 5.1c, only calculations for $\dot{Q} = 37.9$ kW are presented. Figure 5.1c shows that the depletion of O_2 in the flaming region is well reproduced by the model. The computed profile of CO_2 concentration also agrees well with measurements whereas the concentration of CO is under-estimated in the CF region. Comparisons concerning the r.m.s. values of temperature fluctuations ($T_{rms} = \sqrt{\widetilde{T''^2}}$) are only qualitative, since temperature measurements were conducted with 50-µm thermocouples without compensation of thermal inertia, leading to a substantial under-estimation of temperature fluctuations [47]. It is thus not surprising that model results are globally higher than those of the experiments (see Figure 5.1d). Close to the burner, at $z/\dot{Q}^{2/5} < 0.03$, an under-estimation of the temperature fluctuations is observed. This underestimation can be explained because in this region the flow near the burner exit presents a periodic behaviour rather than a fully turbulent flow [47]. The turbulence model used was designed for fully-developed turbulence and is thus not adequate to describe the flow in this region.

Computed r.m.s. velocity fluctuations ($u^*_{r,rms} = \sqrt{\widetilde{u''^2_r}}\Big/\dot{Q}^{1/5}$ and $u^*_{z,rms} = \sqrt{\widetilde{u''^2_z}}/\dot{Q}^{1/5}$) are in good overall agreement with experiments (Figure 5.1e and Figure 5.1f). These figures show that both axial and radial velocity fluctuations increase rapidly in the burner vicinity, reach a peak in the intermittent flame region and then decrease slowly in the plume. A comparison between Figure 5.1e and Figure 5.1f show that the anisotropy of turbulence is well reproduced by the model. As a consequence, the introduction of the ASM model leads to improved solutions as compared to standard formulations of the k-ε model [143]. However, the velocity fluctuations are underestimated near the burner exit (see Figure 5.1e and Figure 5.1f for $z/\dot{Q}^{2/5} < 0.03$). As for temperature, these discrepancies can be attributed to the limited capacity of the turbulence model to deal with the parts of the flow where the turbulence is not fully developed.

Radial profiles of normalized mean temperature, $(T(r,z) - T_\infty)/(T(0,z) - T_\infty)$ and axial velocity, $u_z(r,z)/u_z(0,z)$, at different heights above the burner are represented in Figure 5.2 for a HRR of 37.9 kW. Temperature profiles are well reproduced in the intermittent flame and in the inert plume (see Figure 5.2a$_3$ and Figure 5.2a$_4$), whereas their width is under-predicted in the lower part of the flame (see Figure 5.2a$_1$ and Figure 5.2a$_2$). Figure 5.2b shows that the radial velocity profiles are in close agreement with experimental data whatever the height considered.

Figure 5.3 shows the distributions of soot volume fraction along the axis. Experimental data [64], based on absorption measurements in a 30 cm diameter toluene fire (HRR of 125 KW) and a 30 cm diameter heptane fire (HRR of 116 kW), are also plotted in order to provide a qualitative comparison. Experimental soot volume fractions are approximately constant in the CF region with maximum values of about 12 ppm and 1.3 ppm for the toluene and the heptane pool fires, respectively. In both cases the soot volume fraction decreases rapidly in the IF region owing to soot oxidation. Similar trends are also observed for 7.1 cm diameter toluene, ethylene and methane pool fires [63,158] and for 15 cm diameter kerosene pool fires [163]. These trends are rather well reproduced by the numerical model: maximum values of the soot volume fraction in the CF region are of about 2.00 ppm, 2.05 ppm and 1.59 ppm for the 15.8 kW, 22.9 kW and 37.9 kW pool fires, respectively. Model results show also that the soot particles are not completely oxidized in the flaming region and are then released in the inert plume. As expected the overall soot yield in the overfire region is of 0.012 ppm [68]. Finally, computations suggest that the scaling of McCaffrey [98] can be extended to the soot volume fraction.

Figure 5.4a to Figure 5.4d show the vertical profiles of radiative heat flux at distances, *d*, of either 0.3 or 0.4 m from the center of the burner for the different HRR. Numerical solutions obtained by Snegirev are also plotted [143]. The present calculations exhibit a reasonable agreement with measurements. The magnitude of the peaks is within 15% of measurements whereas their locations are underestimated. Figure 5.4e shows that the evolution of the radiant fraction as a function of the HRR is also well reproduced by the model. The predicted asymptotic value is 0.34, which compares well with the experimental values of 0.35 and 0.33 reported by Souil *et al*. [147] and McCaffrey [98] respectively. Predictions of the radiant fractions are summarized in Table 5.5.

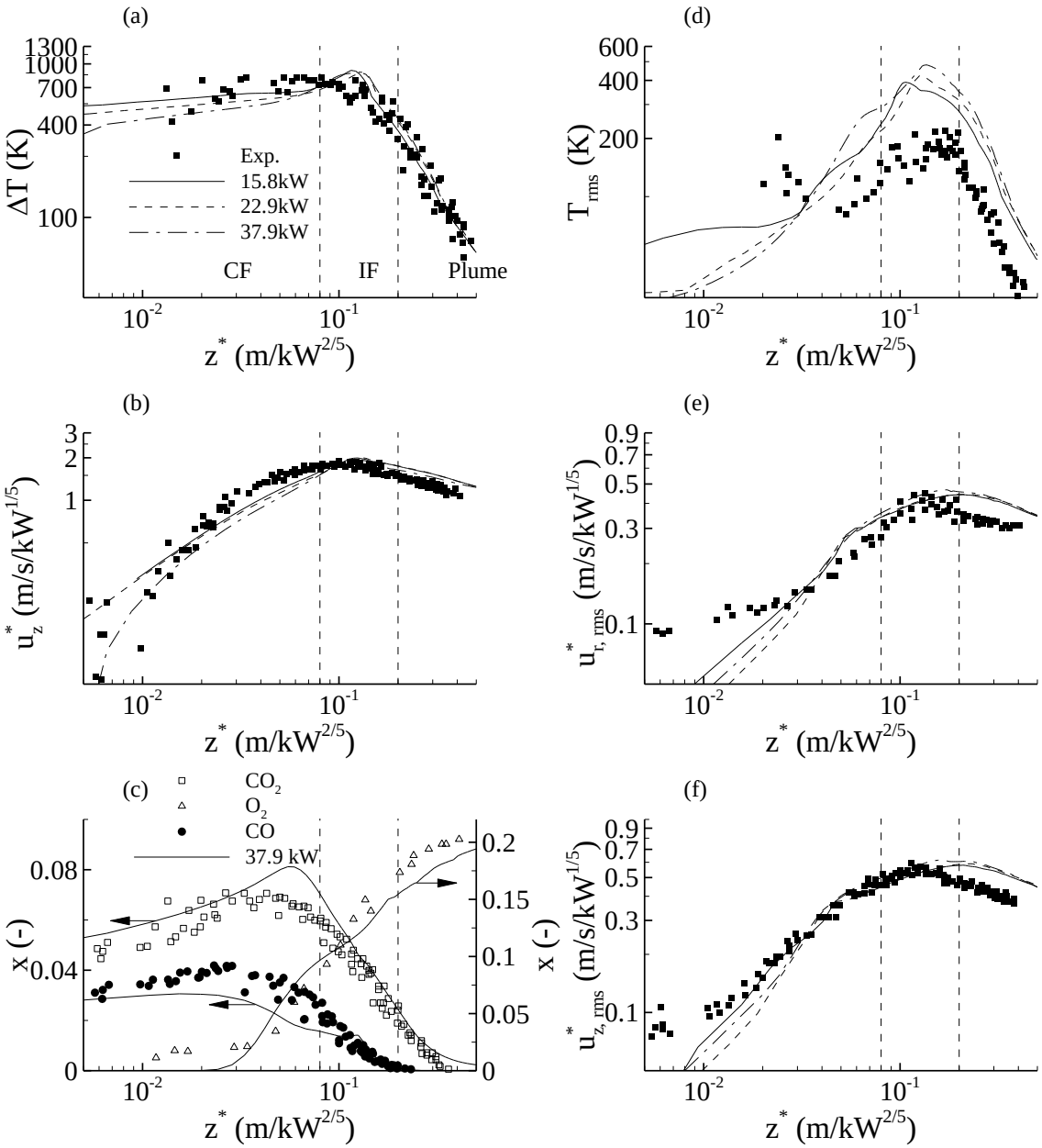

Figure 5.1. Distributions along the axis for the propane flames: a) mean temperature rise, b) normalized mean axial velocity $u_z^* = \widetilde{u_z}/\dot{Q}^{1/5}$, c) gaseous species molar concentrations, d) r.m.s. values of temperature fluctuations, e) normalized r.m.s. values of radial velocity fluctuations $u_{r,rms}^* = \mathrm{u}_{r,rms}/\dot{Q}^{1/5}$, and f) normalized r.m.s. values of axial velocity fluctuations $u_{z,rms}^* = \mathrm{u}_{z,rms}/\dot{Q}^{1/5}$ are plotted as a function of the normalized height $z^* = z/\dot{Q}^{2/5}$. Model predictions (lines) are compared with experimental data (symbols) taken from [47] for $\dot{Q} \in [15.8\ \mathrm{kW} - 37.9\ \mathrm{kW}]$.

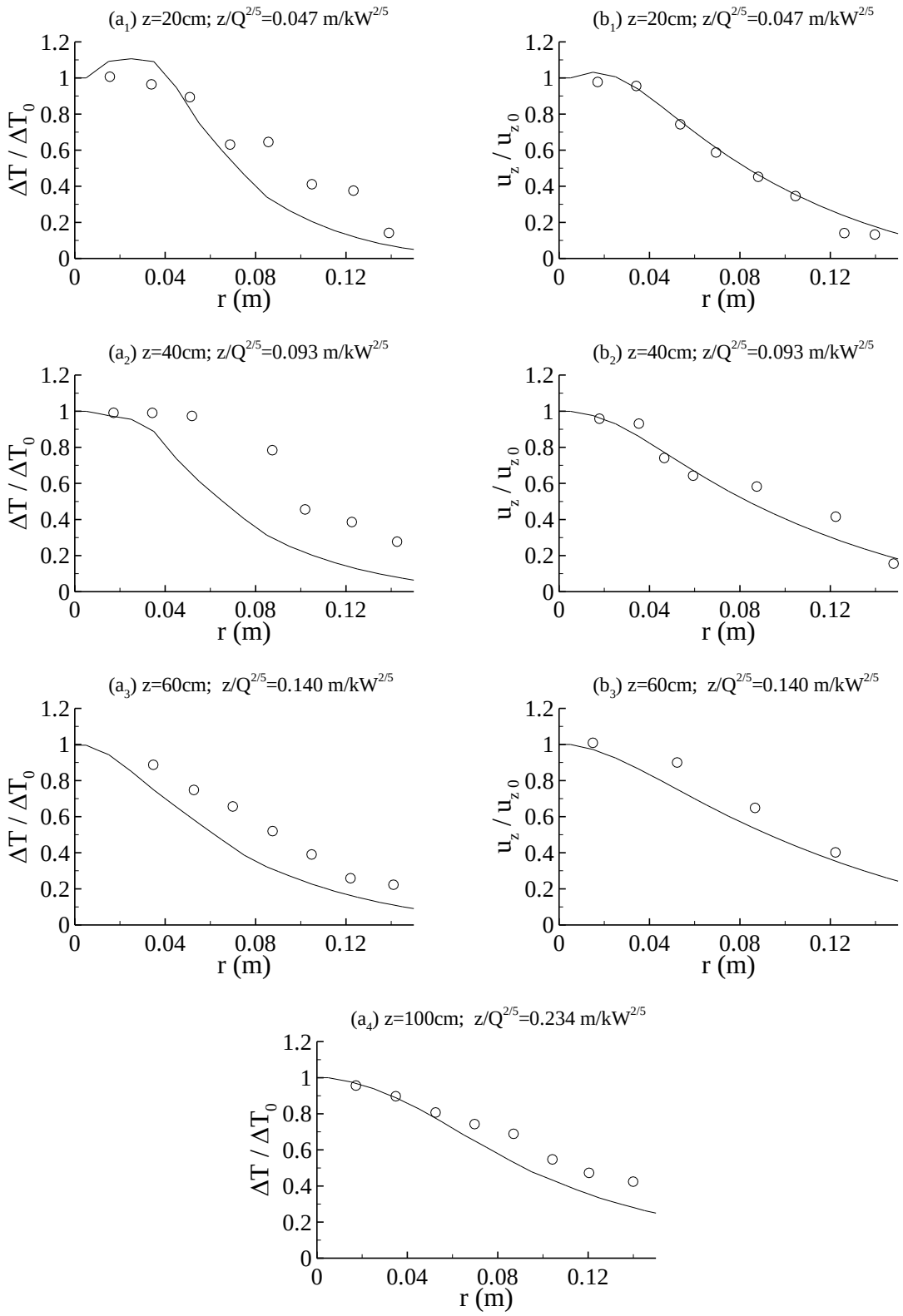

Figure 5.2. Radial profiles for the propane flames of: a) normalized temperature rise, and b) normalized axial velocity at different heights from the burner exit for $\dot{Q} = 37.9$ kW. Model predictions (solid lines) are compared with experimental data (symbols) [47].

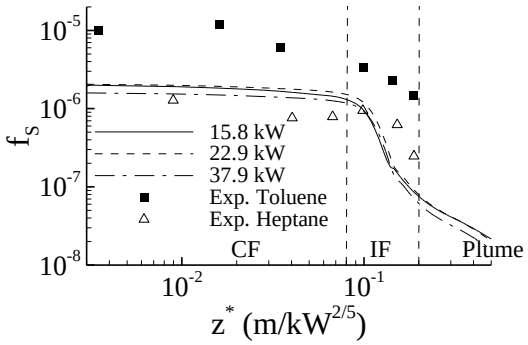

Figure 5.3. Axial distribution of mean soot volume fraction as function of the normalized height $z^* = z/\dot{Q}^{2/5}$ for the propane flames. Experimental data is taken from [64].

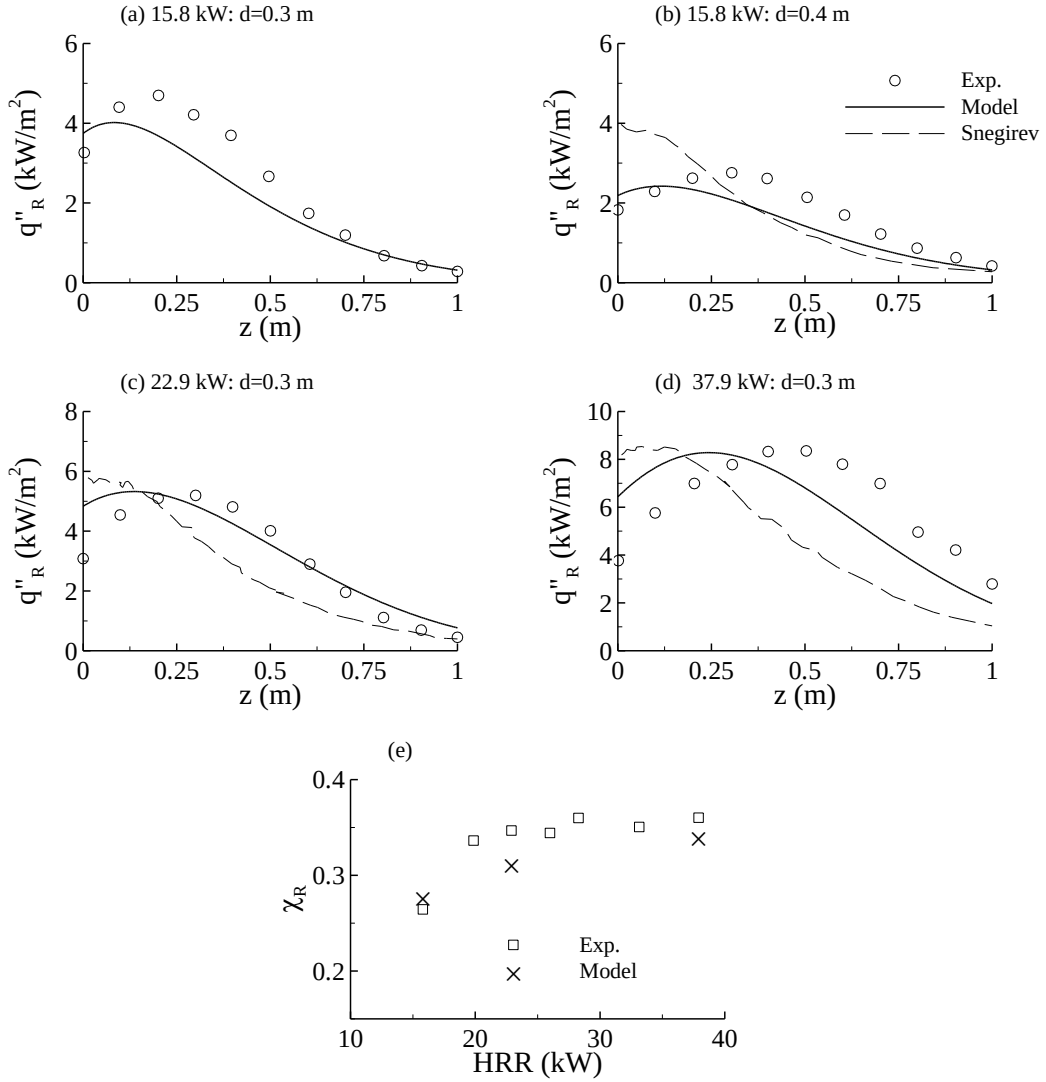

Figure 5.4. Propane flame results: a-d) Vertical distribution of radiative flux at different distances, and e) radiative loss fraction as a function of HRR. In diagrams a-d) model predictions (solid lines) are compared with experimental data (open circles) [147]. Numerical predictions obtained by Snegirev [143] are also plotted (dashed lines).

5.2.2 Methane flames

5.2.2.1 Flame configurations

Two methane pool fires, experimentally investigated by Hostikka *et al*. [59], are simulated. These buoyant diffusion flames were generated on a burner of 0.38 m in diameter with two HRR of 33.4 and 175.8 kW. In both cases the radiant fraction was reported. The vertical radiant heat flux distributions at a distance of 0.732 m from the centre of the burner and the radial radiant heat flux distributions along a radius on the plane aligned with the burner surface were also measured. No measurements of temperature, species or velocity were reported in this study whatsoever. The diameter of the burner and the lower HRR (33.4 kW) are consistent with the experimental conditions used by McCaffrey [98] ($D \approx 0.34\,m$ and $\dot{Q} \in$ [14 kW, 58 kW]) and by Cox and Chitty [24] ($D \approx 0.34\,m$ and $\dot{Q} \in$ [14 kW, 110 kW]). The predicted fire plume structure is then compared with the data reported in these studies.

Measured heat fluxes were used by Hostikka *et al*. [59] to validate the GWB radiation model implemented in Fire Dynamic Simulator (FDS) [99]. Moreover, Krishnamoorthy *et al*. [69] modelled the 176 kW flame by using LES, grey and non-grey formulations of the RTE, and RTE solvers based on parallel versions of either the P_1 approximation or the discrete ordinates method. The non-grey formulation was based on a GWB model similar to that used in FDS.

The computational details are similar to those used for the propane flames. The vertical dimension of the computational domain is extended to 6m in order to keep the outlet boundary far enough from the fire in the case of the 176 kW flame. A non-uniform mesh with 70×240 cells is considered with a mesh size of $1cm \times 1cm$ in the flaming zone.

5.2.2.2 Comparison with available data

Figure 5.5 shows the axial profiles of temperature, velocity, r.m.s. values of temperature fluctuations and mean soot volume fraction normalized by the scaling proposed by McCaffrey [98]. In addition, results of a simulation carried out by considering exactly the same diameter (D ≈ 0.34m) as that used by McCaffrey and by Cox and Chitty are also plotted. As expected the differences between the two simulations are small. Experimental temperatures reported in Figure 5.5a are not corrected for thermocouple radiation, resulting in an under-estimation of 20% according to McCaffrey [98]. Predicted mean temperatures are 200-300 K higher than the experiments in regions where radiation is expected to affect the measurements, and would thus compare well with corrected measured temperatures. The discrepancy between computed and measured mean temperatures is small in the inert plume, where radiation is less important.

Computed mean axial velocities present an excellent agreement with experiments in the CF and IF zones, and are slightly lower than experimental data in the plume. The r.m.s. values of temperature fluctuations exhibit the same trends as those reported for the propane flames (see Figure 5.5c). According to Cox and Chitty [24] temperature fluctuation measurements, conducted with a 13-µm thermocouple, are under-estimated, which explains the discrepancies observed between the model and the experiments for $z/\dot{Q}^{2/5} > 0.03$. This argument is reinforced by recent LES simulations of the McCaffrey flames [154], which reported that the r.m.s. values of temperature fluctuations peak at 500K in the intermittent zone, this value being more consistent with the current simulations. The mean soot volume fraction presents an axial profile similar to those observed in Figure 5.3: it is approximately constant in the CF region with a value of about 0.1 ppm, and then decreases abruptly

in the IF region. It can be observed that soot particles are completely oxidized which is consistent with the experimental observations reported for lab-scale methane pool fires [68].

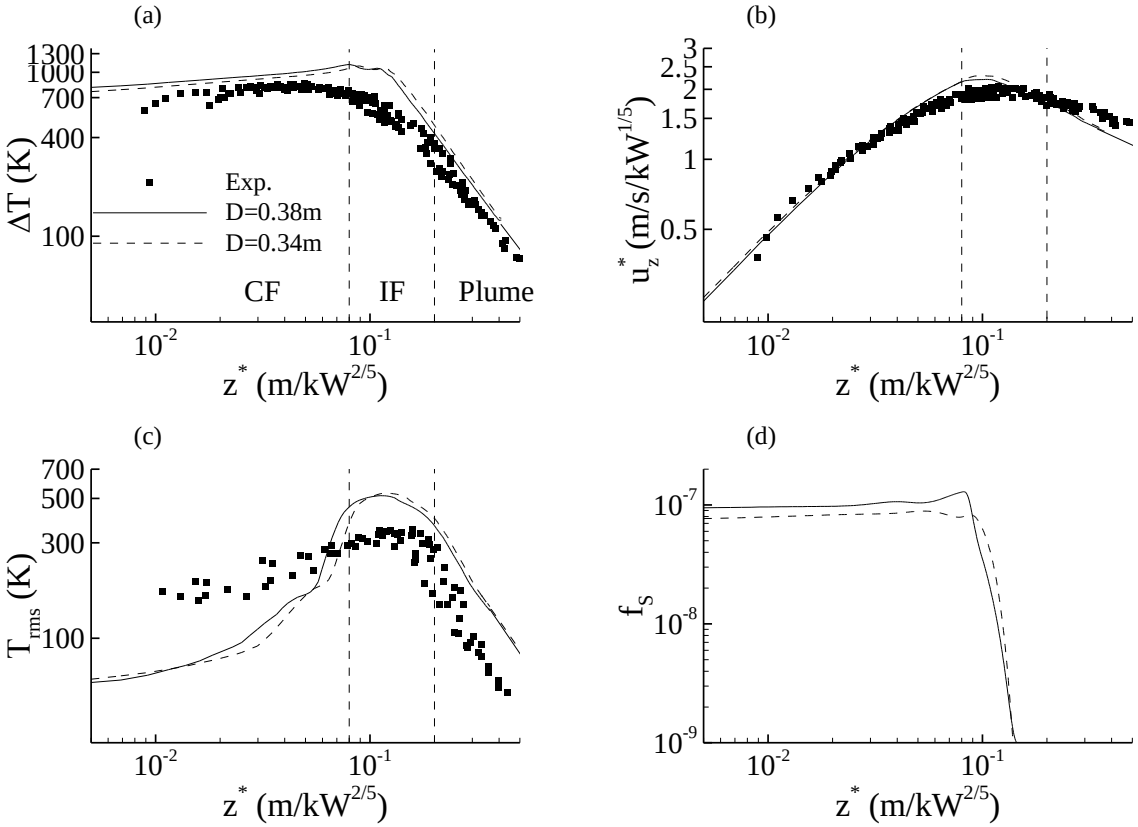

Figure 5.5. Axial distributions for a methane flame with HRR of 34kW: a) mean temperature rise, b) normalized mean axial velocity $u_z^* = \widetilde{u_z}/\dot{Q}^{1/5}$, c) r.m.s. values of temperature fluctuations, and d) soot volume fraction are plotted as a function of the normalized height $z^* = z/\dot{Q}^{2/5}$. Model predictions for $D = 0.38m$ (solid lines) and for $D \approx 0.34m$ (dashed lines) are compared with experimental data (filled squares) taken from [98] for $\dot{Q} \in [14.4\ \mathrm{kW} - 57.5\ \mathrm{kW}]$ (diagrams a and b) and from [24] for $\dot{Q} \in [14.4\ \mathrm{kW} - 109.7\ \mathrm{kW}]$ (diagram c).

Figure 5.6 shows vertical and horizontal heat flux distributions. The numerical results obtained by Hostikka *et al*. [59] and by Krishnamoorthy *et al*. [69] are also plotted in this figure. The predictions of the current model are in reasonable agreement with experiments. In the vertical direction (Figure 5.6a$_1$ and Figure 5.6b$_1$) the fluxes reach a peak at approximately 60% of the uppermost location of the flame tip (defined as $0.2 \times \dot{Q}^{0.4}$) and drop to low values above the visible flame height. In both cases vertical distributions are overpredicted. In the radial direction (see Figure 5.6a$_2$ and Figure 5.6b$_2$) the radiative fluxes decrease monotonically with increasing radial distance and calculated radial profiles are found to match experimental data closely. Predicted radiant fractions are also consistent with experimental data (see Table 5.5).

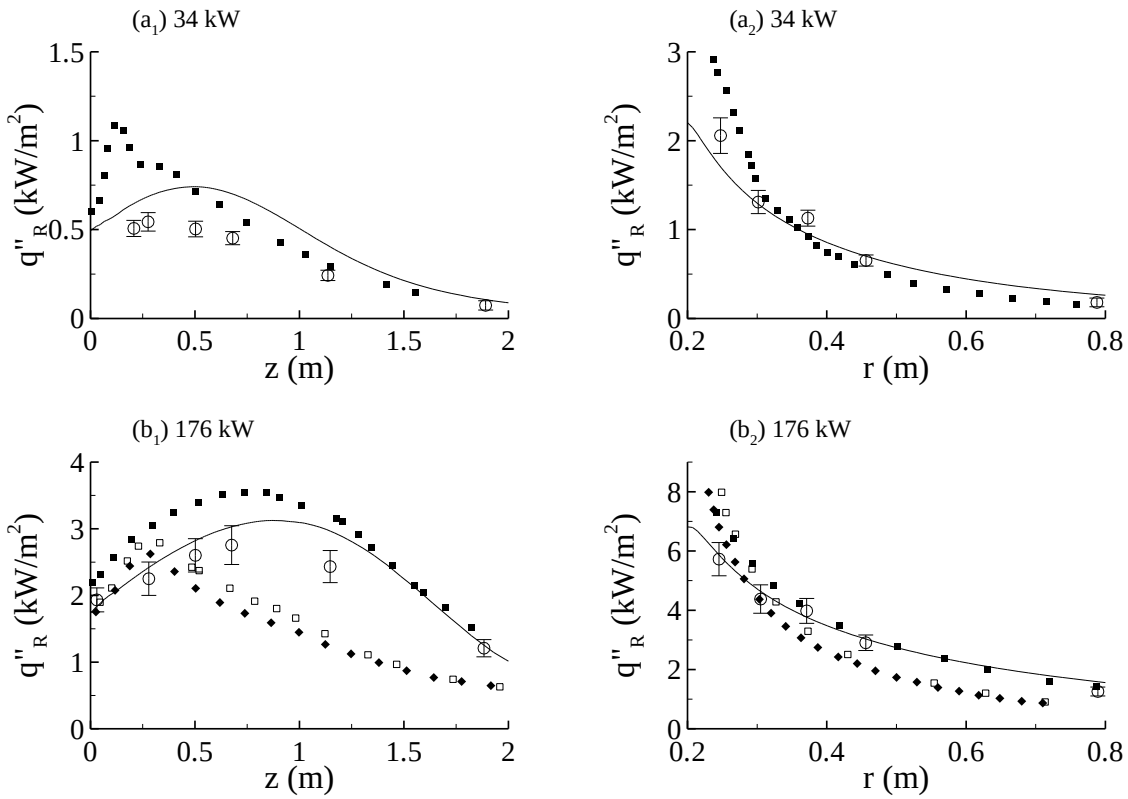

Figure 5.6. Methane flame results: Vertical distribution of the radiant heat flux at a distance of 0.732 m from the centre of the burner (index 1) and radial distribution of the radiant heat flux at z = 0 m (index 2) for: a) $\dot{Q} = 34$ kW, and b) $\dot{Q} = 176$ kW. Model predictions (solid lines) are compared with experimental data [59] (open circles). The numerical predictions obtained by Hostikka *et al*. [59] (filled squares) and Krishnamoorthy *et al*. [69] using non-grey (open squares) and grey (filled diamonds) models are also plotted.

5.2.3 Grey gas and soot approximations

Coupled fluid flow/combustion/radiation simulations and decoupled radiative simulations are carried out in order to quantify the relative importance of non-grey gas and soot radiative properties. Decoupled radiation simulations are carried out by using the fields of scalar variables computed with the FSCK. The interest of performing decoupled computations is to isolate the influence of a modification in the radiative model without adding complexities to the interpretation arising from changes in the flow characteristics. Two simplified radiative models are assessed: the first considers both gases and soot to be grey, whereas the second considers non-grey gases but grey soot. Grey radiative properties are evaluated by considering Planck-mean absorption coefficients.

The influences of these approximations are summarized in Table 5.5. Model results show that considering the medium as grey is a poor approximation resulting in large over-predictions of the radiant fraction. Nevertheless, these discrepancies are greater for the methane flames, where gas radiation dominates, than for the propane flames, where the contributions of gas and soot are comparable. Radiant fractions computed with the grey radiation model are slightly lower for the coupled calculations than for the decoupled ones, which is consistent with the fact that predicted mean temperatures and mean soot volume fractions are lower in the former case.

The computational efficiency of the FSCK method can be considerably improved if soot particles are assumed to be grey. In this case the soot absorption coefficient can be added directly to the FS k-

distributions [151] and, as a consequence, k-distributions can be pre-databased at the FS level. This avoids assembling the FS k-distributions from NB k-distributions during the sequence of calculations, reducing the CPU time by a factor of approximately 6.4 in the present coupled and decoupled simulations. For these computations, Mixed Full Spectrum (MFS) k-distributions were pre-databased for 6 values of R and for 23 values of T and T_0 in the range 300-2500 K. Three-dimensional interpolations are performed for arbitrary species mole fraction ratio, temperature and reference temperature. Model predictions in Table 5.5 show that considering soot as grey particles is a fairly good simplification for the laboratory-scale flames considered in the present study. For both decoupled and coupled calculations it has almost no influence in the case of the methane flames and results in an over-prediction of the radiant fractions of less than 5% for the propane flames (see Table 5.5). Nevertheless, this conclusion must be taken with care when modelling more heavily sooting fuels or larger flames [59,111].

Table 5.5. Radiative fractions of the lab-scale flames. The values in parenthesis indicate the relative error (in %) defined as $E_r = \left(\chi_{R,model} - \chi_{R,FSCK}\right)/\chi_{R,FSCK} \times 100$

Radiative Model	Calculations	Propane [147]			Methane [98]	
		15.8 kW	22.9 kW	37.9 kW	34 kW	176 kW
Exp.	--	0.264	0.347	0.360	0.15 (0.133-0.166)*	0.19 (0.169-0.211)*
FSCK	Coupled	0.278	0.313	0.341	0.172	0.176
Grey Gas/Soot	Coupled	0.392 (41.0%)	0.401 (28.1%)	0.468 (37.2%)	0.461 (168.0%)	0.355 (101.7%)
	Decoupled	0.413 (48.6%)	0.422 (34.8%)	0.515 (51.0%)	0.490 (184.9%)	0.382 (117.0%)
Non-Grey Gas/Grey Soot	Coupled	0.283 (1.8%)	0.321 (2.6%)	0.349 (2.3%)	0.171 (-0.58%)	0.176 (~0)
	Decoupled	0.288 (3.6%)	0.328 (4.8%)	0.357 (4.7%)	0.172 (~0)	0.176 (~0)

* the uncertainty on χ_R is estimated as 11% [59].

5.3 Modelling thermal radiation from large-scale pool fire

Based on the insights obtained from studying laboratory-scale pool fires, two large-scale methane pool fires are studied in this section. The first objective of this study is to compare the radiant fractions and radiative fluxes on remote surfaces in order to assess the radiative property model. The second objective aims to quantify the importance of Turbulence-Radiation Interactions (TRI) in such buoyant flames. The model, described in section 5.1, is referred as Mod 1 hereafter.

5.3.1 Experimental and computational details

Two 1-m diameter methane pool fires with HRR ($\dot{Q}$) of 49 kW and 162 kW are simulated. These flames were experimentally investigated by Hostikka *et al*. [59]. The corresponding dimensionless fire powers, given by $\dot{Q}_D^* = \dot{Q}/\rho_\infty C_p T_\infty \sqrt{gD}D^2$, are of 0.044 and 0.14 respectively. In this expression *D* and *g* represent the pool diameter and the gravitational acceleration respectively. The subscript ∞ refers to ambient conditions. In both cases the radiant fraction, χ_R, was reported. The radial and vertical radiative heat flux profiles outside the flame region were also measured. The vertical

distributions were measured at 1m and 0.8m from the centre of the burner for the 49 kW and the 162 kW pool fires, respectively. The radial distributions were measured along a radius on the plane aligned with the burner surface. Unfortunately, no measurement concerning the flame structure was reported in this study.

The overall computational domain is 3 m (R) × 6 m (L). A preliminary grid refinement study indicated that a non-uniform mesh with 85 × 260 cells and a mesh size of the order of 1 cm × 1 cm in the flaming zone is sufficient to achieve grid-independent solutions.

Figure 5.7 shows the fields of mean temperature. In the case of the 49 kW pool fire (Figure 5.7a), the combustion is found to occur close to the burner. This follows the experimental observations of Zukoski [169] who pointed out that, when $\dot{Q}_D^* < 0.1$, the combustion region is divided into many flamelets that lean toward the axis of the source and that have flame lengths much smaller than the diameter of the source. Predicted flame heights are determined here as the location where the mean mixture fraction reaches its stoichiometric value (0.055 for methane in air). The flame height normalized by the burner diameter is of about 0.05 which is consistent with the data compiled by Zukoski for a small range of $\dot{Q}_D^*$.

As the normalized HRR is increased to 0.14 (Figure 5.7b), the mean temperature field suggests that the classical description of a pool fire with a single continuous flame region, an intermittent flame region and the inert plume is recovered. This behaviour is also in qualitative agreement with experimental observations which mention that the short flamelets are expected to merge and form a single flame for $\dot{Q}_D^* \approx 0.1$ [169]. The normalized flame length is 0.61 which compares rather well with the value of 0.8 computed from both the correlations of Heskestad [57] and Quintiere and Grove [130]. The correlations are applied by setting the radiant fraction, χ_R, to 0.16 as measured by Hostikka *et al*. [59]. The numerical predictions of flame heights agree also well with the data compiled by Zukoski [169] which show that measured normalized flame heights range from about 0.6 to 1 for $\dot{Q}_D^* \approx 0.14$.

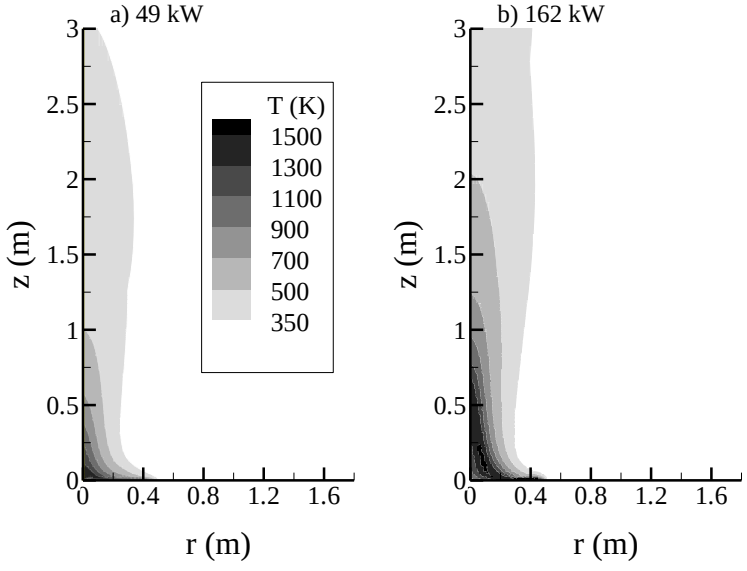

Figure 5.7. Mean temperature fields for methane pool fires at: a) 49 kW, and b) 162 kW.

5.3.2 Comparison with available experimental data

Hostikka *et al*. [59] reported radiant fractions of 0.08 and 0.16 for the 49 and the 162 kW pool fires with an uncertainty on these values of 11%. Measured radiant fractions range thus from 0.071 to 0.089 and from 0.142 to 0.178 for the 49 kW and the 162 kW pool fires respectively. The corresponding predicted radiant fractions are estimated to 0.095 and 0.206, which compares favourably well with the upper bounds of the experimental data. In addition these results show that the model reproduces the increase in radiant fraction with $\dot{Q}_D^*$ correctly.

Figure 5.8 shows the vertical and radial distributions of radiative flux. Predictions are also in good agreement with the experimental data. Figure 5.8a$_1$ and Figure 5.8b$_1$ show that in the vertical direction the radiative heat fluxes reach a peak and then decrease rapidly. Calculated vertical profiles are found to match closely the experiments. Figure 5.8a$_2$ and Figure 5.8b$_2$ show that in the radial direction the radiative heat flux decrease quickly as the radial distance increases. For the 162 kW pool fire the simulation over-predicts the experiment near the burner whereas a more satisfactory agreement is obtained for $r > 0.75m$ (see Figure 5.8b$_2$). The largest discrepancies are observed for the 49 kW pool fire (see Figure 5.8a$_2$), where the heat fluxes are very low (not significant for fire safety purposes) and therefore very sensitive to small errors in the flow field predictions.

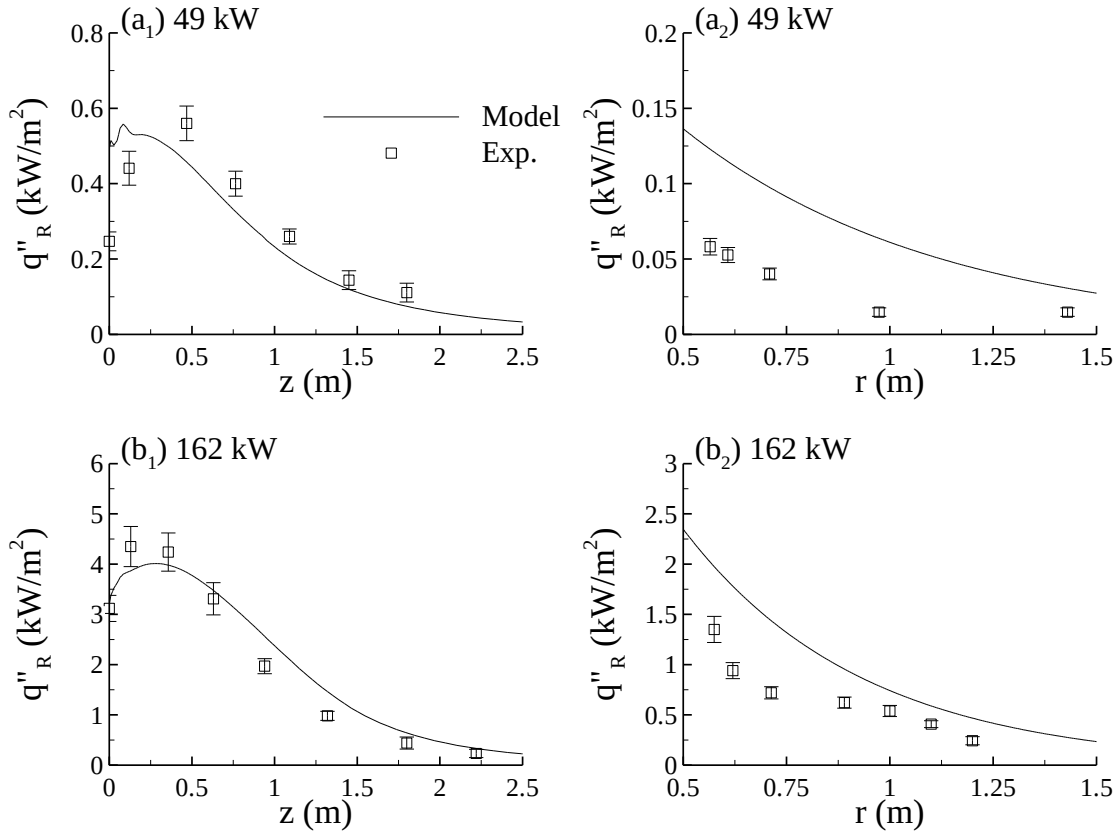

Figure 5.8. Methane pool fires: Predicted heat fluxes vs. experiments for a) the 49 kW pool fire, and b) the 162kW pool fire. The index 1 refers to the vertical distribution of heat flux, at r=1m for the 49kW pool fire and at r=0.8m for the 162kW pool fire, while the index 2 refers to the radial distribution of heat flux at z=0m for both pool fires. Experimental results from Hostikka *et al*. [59].

5.3.3 Influence of TRI-related terms on radiative outputs

This section discusses how the predicted radiant fractions and radiative heat fluxes on surrounding surfaces are affected by considering different TRI closures for the absorption and emission terms. The role of the TRI on radiative outputs can be better understood by isolating their effects on the radiation calculations alone. As a consequence, decoupled radiation calculations are carried out by using the flow field computed with the most complete model studied (Mod 1).

The different scenarios as well as the corresponding predicted radiant fractions are summarized in Table 5.6. The comparison between the calculations carried out with (Mod 1) and without TRI (Mod 2) shows clearly the strong influence of the TRI on the flame radiative losses: the radiant fractions are under-predicted by about 130% and 178% for the 49 kW and the 162 kW pool fires when the TRI are ignored. In addition, these results suggest that the enhancement in radiative losses due to TRI increases with $\dot{Q}^*$.

The comparison of the radiant fractions computed with Mod 2, Mod 3, Mod 4 and Mod 5 show the effects of the different levels of closure on the emission term. In all these simulations the absorption coefficient in the absorption term is modelled from mean property values. In Mod 3 only the influence of TRI on the mean Planck function is considered. In Mod 4 the fluctuations of the absorption coefficient and of the Planck function are taken into account separately, but the correlation between the two is disregarded. Finally, Mod 5 considers the effects of the correlation between the gas absorption coefficient and the Planck function.

Results in Table 5.6 reveal that accounting for the temperature self-correlation increases significantly the radiant fractions (Mod 2 vs. Mod 3) but its contribution alone is not sufficient to model correctly the emission term (Mod 3 vs. Mod 5). Mod 4 improves the predictions as compared to Mod 3 (Mod 4 vs. Mod 5). However the comparison between Mod 4 and Mod 5 shows that the gas absorption coefficient–Planck function correlation cannot be neglected. As discussed by Coelho [19] this correlation is positive, resulting in a large increase in the radiant fractions (Mod 5 vs. Mod 4) in the present cases. Finally Mod 1 extends Mod 5 by considering the effects of the absorption coefficient self-correlation on the absorption term. This term contributes to enhance flame absorption leading to a non-negligible reduction in radiant fraction (see Table 5.6).

Table 5.6. Effects of the different TRI closures on the radiant fraction. The values in parenthesis indicate the relative error (in %) defined as $\mathrm{E_r} = \left(\chi_{\mathrm{R,Mod1}} - \chi_{\mathrm{R,model}}\right)/\chi_{\mathrm{R,model}} \times 100$. Quantities denoted without an overbar refer to evaluation from mean variables, i.e. without accounting for TRI.

Test Case	Absorption	Emission	49 kW	162 kW
Exp.	--	--	0.08 (0.071-0.089)*	0.16 (0.142-0.178)*
Mod 1	$\bar{k}$	$\overline{k \times aI_b}$	0.095	0.206
Mod 2	k	$k \times aI_b$	0.041 (131.7%)	0.074 (178.4%)
Mod 3	k	$k \times \overline{aI_b}$	0.048 (97.9%)	0.103 (100.0%)
Mod 4	k	$\bar{k} \times \overline{aI_b}$	0.061 (57.3%)	0.134 (53.7%)
Mod 5	k	$\overline{k \times aI_b}$	0.120 (-21%)	0.223 (-7.6%)

* the uncertainty on χ_R is estimated as 11%.

Figure 5.9 shows the effects of these different closures on the vertical and radial distributions of radiative flux. A comparison between the simulations made with Mod 1 and Mod 2 shows that heat fluxes are severely under-predicted when TRI are neglected: the peaks in the vertical direction are lower by factors of about 2.8 and 2.5 for the 49 kW and the 162 kW pool fires whereas the radial distributions are also strongly underestimated. The predictions obtained with the other TRI scenarios follow the same trends as those observed for the radiant fractions (presented in Table 5.6). Figure 5.9 shows also that the different closures modify the shape of the distributions. It can be observed that both predicted vertical and radial profiles are much flatter in absence of TRI than when Mod 1 is considered.

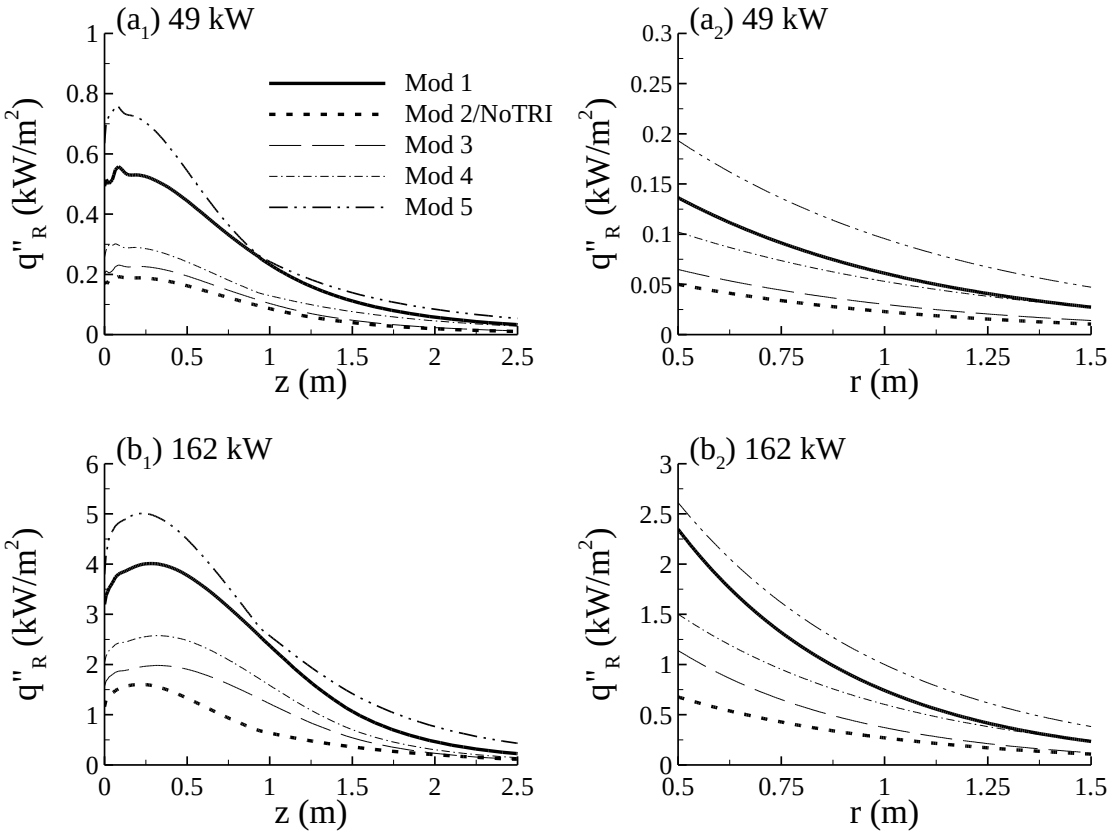

Figure 5.9. Effects of different TRI closures on radiative heat fluxes for a) the 49 kW pool fire, and b) the 162 kW pool fire. The indexes 1 and 2 refer to the vertical distribution of heat flux and to the radial distribution of heat flux, respectively.

5.4 Concluding remarks

Five laboratory-scale turbulent buoyant diffusion flames, considering propane and methane as fuels, and two large-scale turbulent buoyant diffusion flames were simulated by using a buoyancy-modified k-ε model and the SLF model to model chemistry. The FSCK was applied to account for the non-grey nature of gas and soot radiation. A semi-empirical two-equation acetylene-based model was considered for modelling the soot. TRI were modelled on the basis of the OTFA, with the emission

term and the mean absorption coefficient being closed by using a presumed PDF of the mixture fraction, the scalar dissipation rate and the enthalpy defect. In addition, the importance of the TRI and the influence of different levels of closure for the TRI on the prediction of radiative losses and radiative fluxes on remote surfaces were quantified. The following conclusions can be drawn from this study:

- The present model is able to provide reliable predictions concerning the structure of the buoyant fire plume.
- Predicted radiant fractions and radiative heat fluxes on remote surfaces are in satisfactory agreement with available experimental data when TRI are considered.
- The use of the grey approximation to treat combustion gases leads to a severe over-prediction of the radiative losses in the studied lab-scales flames. On the other hand, the grey assumption present good results for the moderately sooting lab-scale flames tested, which results in a substantial gain in CPU time.
- TRI considerably enhance the radiative losses and the radiative heat fluxes on remote surfaces.
- The complete gas absorption coefficient–Planck function correlation should be considered in order to properly take into account the influence of TRI on the emission term.
- The effects of absorption coefficient self-correlation on the absorption term cannot be neglected. They contribute to increase the absorption and in turn to decrease the radiative losses and the heat fluxes on remote targets.

6 Conclusions and perspectives

A numerical study of buoyant diffusion flames was carried out, with the principal objective of modelling the thermal radiative transfer and the soot formation/destruction processes. Several radiative property models, some soot models and the treatment to account for turbulence-radiation interactions (TRI) were implemented into a CFD code in order to numerically study these particular flames. Decoupled radiative calculations in one-dimensional and bi-dimensional axisymmetric benchmarks were carried out for assessing different radiative property models. Laminar coflow diffusion flames were simulated in order to assess the capability of an acetylene/benzene semi-empirical soot model to predict soot formation for different fuels and different configurations. Finally turbulent laboratory-scale and large-scale diffusion flames were simulated considering moderately sooting fuels. Radiant magnitudes were estimated considering a presumed probability density function for closing emission TRI and the mean absorption coefficient. The main conclusion of this study can be summarized as follows:

- The radiative property model which presents the best compromise in terms of accuracy and computational resources is the Full Spectrum Correlated-k (FSCK) model. It allows considering the spectral characteristics of the different participant gases and soot. The mixing model of Modest and Riazzi was found to be the best for properly generating the Full Spectrum k-distributions. The generation of the Mixed Narrow Band (MNB) database allows increasing significantly the efficiency of the model, taking out of the simulations the otherwise “expensive” process of mixing. Considering a Mixed Full Spectrum (MFS) reduces further the CPU time. However the approach is limited to grey particles. Using 5 to 7 Gauss-Legendre quadrature points for the integration of the k-distribution seems to provide a good compromise.
- The semi-empirical acetylene/benzene based two-equation soot model, proposed by Lindstedt, produced acceptable results in the case of laminar coflow diffusion flames. This model provides reliable predictions over a wide range of fuels and configurations: in particular for inverse flames, which are very interesting due to their sooting characteristics, similar to those encountered in under-ventilated fires.
- The results of the different simulations have proven that the implemented radiative property model and the soot formation/destruction model are consistent, producing accurate results either for laminar or turbulent flames. Therefore, the main objective of this study of modelling the thermal radiation and the sooting characteristics of buoyant diffusion flames is fulfilled.

The perspectives of this work are numerous:

In the case of laminar flames it is important to consider a full coupling between the flow and the chemistry in order to simulate the extinction phenomena and study the highly sooting “open flames”. A second perspective could be to consider detailed soot models, in order to have a more general formulation, providing solutions more independent of the fuel considered. Even though these perspectives are promising, it is important to remember that the aim is to apply these models to turbulent flames where the computational cost is an important factor to be considered.

A second axe of research is the application of the actual models to different laminar configurations. Decreasing the oxygen content of the oxidant flow of laminar flames in order to study the sooting characteristics is of practical interest within the framework of unwanted fires. Inverse diffusion flames seem also a good configuration to extend this work for studying fire in under-ventilated conditions. This configuration is easy to be studied experimentally and would provide benchmark tests that are not available nowadays.

A third axe of perspective of this work can be to consider more complete closures for turbulent interactions. Considering the correlation between the gas phase and the sooting characteristic in the soot growth and oxidation model would allow to properly predict the sooting characteristics of the turbulent flames. The same consideration can be taken for the TRI, properly considering the correlation between the soot volume fraction and the emission TRI. This would allow simulating more sooting fuels under turbulent conditions.

Bibliography

[1] I.M. Aksit and J.B. Moss, “A hybrid scalar model for sooting turbulent flames”, *Combust. Flame*, vol. 145, 2006, pp. 231–44.

[2] J. Appel, H. Bockhorn and M. Frenklach, “Kinetic modeling of soot formation with detailed chemistry and physics: laminar premixed flames of C2 hydrocarbons”, Combust. Flame, vol. 121, 2000, 122–36.

[3] X.S. Bai, M. Balthasar, F. Mauss and L. Fuchs, “Detailed soot modeling in turbulent jet diffusion flames”, *27th Symp. Int. Combustion/The Combustion Institute*, 1998, pp. 1623–30.

[4] M. Balthasar, A. Heyl, F. Mauss, F. Schmitt and H. Bockhorn, “Flamelet modeling of soot formation in laminar ethylene/air-diffusion flames”, *26th Symp. Int. Combustion/The Combustion Institute*, 1996, pp. 2369–77.

[5] M. Balthasar and M. Kraft, “A stochastic approach to calculate the particle size distribution function of soot particles in laminar premixed flames”, *Combust. Flame*, vol. 133, 2003, pp. 289–98.

[6] V.V. Barve, O.A. Ezekoye and N.T. Clemens, “Soot reduction in strongly forced lifted CH4-air laminar flames”, *Combust. Theory Model.*, vol. 13, 2009, pp. 671–703.

[7] T. Beji, J.P. Zhang, W. Yao and M. Delichatsios, “A novel soot model for fires: Validation in a laminar non-premixed flame”, *Combust. Flame*, vol. 185, 2011, pp. 281–90.

[8] N.W. Bressloff, J.B. Moss and P.A. Rubini, “CFD prediction of coupled radiation heat transfer and soot production in turbulent flames”, *26th Symp. Int. Combustion/The Combustion Institute*, 1996, pp. 2371–86.

[9] N.W. Bressloff, “The influence of soot loading on weighted-sum-of-grey-gases solutions to radiative transfer equation across mixtures of gases and soot”, *Int. J. Heat Mass Transfer*, vol. 42, 1999, pp. 3469–80.

[10] S. J. Brookes and J. B. Moss, “Predictions of soot and thermal radiation properties in confined turbulent jet diffusion flames”, *Combust. Flame*, vol. 116, 1999, pp. 486–503.

[11] D. Carbonell, C.D. Perez-Segarra, P.J. Coelho and A. Oliva, “Flamelet mathematical models for non-premixed laminar combustion”, *Combust. Flame*, vol. 156, 2009, pp. 334–47.

[12] D. Carbonell, A. Oliva and C.D. Perez-Segarra, “Implementation of two-equation soot flamelet models for laminar diffusion flames”, *Combust. Flame,* vol. 156, 2009, pp. 621–32.

[13] M.R.J. Charest, C.P.T. Groth and Ö.L. Gülder, “A numerical study on the effects of pressure and gravity in laminar ethylene diffusion flames”, *Combust. Flame,* vol. 158, 2011, pp.1933–45.

[14] S.C.P. Cheung and G.H. Yeoh, “A fully-coupled simulation of vortical structures in large-scale buoyant pool fire”, *Int. J. Thermal Sci*., vol. 48, 2009, 2187–202.

[15] E.H. Chui, G.D. Raithby and P.M.J. Hughes, “Prediction of radiative transfer in cylindrical enclosures with the finite volume method”, *J. Thermophys. Heat Transfer*, vol. 6, 1992, pp. 605–11.

[16] P.J. Coelho, “Numerical simulation of radiative heat transfer from non-gray gases in three-dimensional enclosures”, *J. Quant. Spectrosc. Radiat. Transfer*, vol. 74, 2002, pp. 307–28.

[17] P.J. Coelho, P. Perez and M. El Hafi, “Benchmark numerical solutions for radiative heat transfer in two-dimensional axisymmetric enclosures with non-gray sooting media”, *Numer. Heat Transfer Part B*, vol. 43, 2003, 425–44.

[18] P.J. Coelho, “Detailed numerical simulation of radiative transfer in a non-luminous turbulent jet diffusion flame”, *Combust. Flame*, vol. 136, 2004, pp. 481–92.

[19] P.J. Coelho, “Numerical simulation of interaction between turbulence and radiation in reactive flows”, Prog. Energ. Combust. Sci., vol. 33, 2007, pp. 311–83.

[20] J.L. Consalvi, B. Porterie and J.C. Loraud, “Dynamic and radiative aspects of fire-water mist interactions”, *Combust. Sci. and Tech*., vol. 176, 2004, pp. 721–52.

[21] J.L. Consalvi, R. Demarco, A. Fuentes, S. Melis, and J.P. Vantelon, “On the modelling of radiative heat transfer in laboratory-scale pool fires”, *Proc. 7th Mediterranean Combustion Symposium*, Sardinia, 2011.

[22] J.L. Consalvi, R. Demarco and A. Fuentes, “Modelling thermal radiation in buoyant turbulent diffusion flames”, *Combust. Theory Model.*, 2012. Available online in doi:10.1080/13647830.2012.662283

[23] J.L. Consalvi and R. Demarco, “Modelling thermal radiation from one-meter diameter methane pool fires”, *Eurotherm Seminar N°95 Computational Thermal Radiation in Participating media IV*, Nancy, France, 2012. Available online in *J. Phys.: Conf. Ser.* 369 012012 doi:10.1088/1742-6596/369/1/012012

[24] G. Cox and R. Chitty, “Some stochastic properties of fire plumes”, Fire Mater., vol. 6, 1982, pp. 127–34.

[25] L. Davidson, “Second-order correction of the k-ε model to account for non-isotropic effects due to buoyancy”*, Int. J. Heat Mass Trans*., vol. 33, 1990, pp. 2599–608.

[26] J.L. De Ris, “Fire radiation - A review”, *Proc. Combust. Inst.*, vol. 17, 1979, pp. 1003–16.

[27] R. Demarco, J.L. Consalvi, A. Fuentes and S. Melis, “Modelling radiative heat transfer in axisymmetric configurations with non-grey sooting media”, *Proc. International Congress Combustion and Fire Dynamics*, Santander, Spain, 2010.

[28] R. Demarco, J.L. Consalvi, A. Fuentes and S. Melis, “Assessment of radiative property models in non-gray sooting media”, *Int. J. Thermal Sci*., vol. 50, 2011, pp. 1672–84.

[29] R. Demarco, J.L. Consalvi, A. Fuentes and S. Melis, “Modeling radiative heat transfer in sooting laminar coflow flames”, *Proc. 7th Mediterranean Combustion Symp*., Sardinia, Italy, 2011.

[30] R. Demarco, J.L. Consalvi and A. Fuentes, “Influence of radiative property models on soot production in laminar coflow ethylene diffusion flames”, *Eurotherm Seminar N°95 Computational Thermal Radiation in Participating media IV*, Nancy, France, 2012. Available online in *J. Phys.: Conf. Ser.* 369 012011 doi:10.1088/1742-6596/369/1/012011

[31] S. Dembele and J.X. Wen, “Investigation of a spectral formulation for radiative heat transfer in one-dimensional fires and combustion systems”, *Int. J. Heat Mass Transfer*, vol. 43, 2000, pp. 4019–30.

[32] M.K. Denison and B.W. Webb, “A spectral line-based weighted-sum-of-gray-gases model for arbitrary RTE solvers”, *ASME J. Heat Transfer*, vol. 115, 1993, pp. 1004–12.

[33] M.K. Denison and B.W. Webb, “An absorption-line blackbody distribution function for efficient calculation of gas radiative transfer”, *J. Quant. Spectrosc. Radiat. Transfer*, vol. 50, 1993, pp. 499–510.

[34] M.K. Denison and B.W. Webb, “The spectral line-based weighted-sum-of-gray-gases model in non-isothermal non-homogeneous media”, *ASME J. Heat Transfer*, vol. 117, 1995, pp. 359–65.

[35] M.K. Denison and B.W. Webb, “The spectral-line weighted-sum-of-gray-gases model for H2O/CO2 mixtures”, *ASME J. Heat Transfer*, vol. 117, 1995, pp. 788–92.

[36] M.K. Denison and B.W. Webb, “Development and application of an absorption-line blackbody distribution function for CO2”, *Int. J. Heat Mass Transfer*, vol. 38, 1995, pp. 1813–21.

[37] M.K. Denison and B.W. Webb, “The absorption-line blackbody distribution function at elevated pressure” in *Radiative Transfer - I, Proceedings of the First International Symposium on Radiation Transfer*, ed. M.P. Mengüç, Begell House, New York, 1996, pp. 228–38.

[38] S.B. Dworkin, Q. Zhang, M.J. Thomson, N.A. Slavinskaya and U. Riedel, “Application of an enhanced PAH growth model to soot formation in a laminar coflow ethylene/air diffusion flame”, *Combust. Flame*, vol. 158, 2011, pp. 1682–95.

[39] G.M. Faeth, “Laminar and Turbulent Gaseous Diffusion Flames”, in: “Microgravity Combustion”, Ed. H.D. Ross, Academic Press, San Diego, 2001, p. 83.

[40] M. Fairweather W.P. Jones, H.S. Ledin and R.P. Lindstedt, “Predictions of soot formation in turbulent non-premixed propane flames”, *24th Symp. Int. Combustion/The Combustion Institute*, 1992, pp. 1067–74.

[41] C.P. Fenimore and G.W. Jones, “Oxidation of soot by hydroxyl radicals”, *J. Phys. Chem*., vol. 71, 1967, pp. 593–7.

[42] S.J. Fisher, B. Hardouin-Duparc and W.L. Grosshandler, “The structure and radiation of an ethanol pool fire”, *Combust. Flame*, vol. 70, 1987, pp. 291–306.

[43] W.A. Fiveland, “Discrete-ordinates solutions of the radiative transport equation for rectangular enclosures”, *ASME J. Heat Transfer*, vol. 106, 1984, pp. 699–706.

[44] M. Frenklach and S.J. Harris, “Aerosol dynamics modeling using the method of moments”, *J. Colloid Interface Sci.*, vol. 118, 1987, pp. 252–61.

[45] A. Garo, R. Said and R. Borghi, in: “Soot Formation in Combustion: Mechanism and Models”, ed. H. Bockhorn, Springer-Verlag, 1994, p. 527.

[46] F. Gelbard and Y. Tambour, “Sectional representations for simulating aerosol dynamics”, *J. Colloid Interface Sci*., vol. 76, 1980, pp. 541–56.

[47] E. Gengembre, P. Cambray, D. Karmed and J.C. Belet, “Turbulent diffusion flames with large buoyancy effects”, Combust. Sci. Technol., vol. 41, 1984, pp. 55–67.

[48] R.M. Goody, R. West, L. Chen and D. Chrisp, “The correlated-k method for radiation calculations in non-homogeneous atmospheres”, *J. Quant. Spectrosc. Radiat. Transfer*, vol. 42, 1989, pp. 539–50.

[49] J.P. Gore and G.M. Faeth, “Structure and radiation properties of luminous turbulent acetylene/air diffusion flames”, *ASME J. Heat Transfer*, vol. 110, 1988, pp.173–81.

[50] V. Goutiere, F. Liu and A. Charrette, “An assessment of real-gas modeling in 2D enclosures”, *J. Quant. Spectrosc. Radiat. Transfer*, vol. 64, 2000, pp. 299–326.

[51] W. Grosshandler, “A narrow band model for radiation calculations in a combustion environment”, *NIST Technical Note TN 1402*.

[52] H. Guo, F. Liu, G.J. Smallwood and Ö.L. Gülder, “The flame preheating effect on numerical modelling of soot formation in a two-dimensional laminar ethylene–air diffusion flame”, *Combust. Theory Model.*, vol. 6, 2002, pp. 173–87.

[53] H. Guo, F. Liu, G.J. Smallwood and Ö.L. Gülder, “A numerical study of the influence of transport properties of inert diluents on soot formation in a coflow laminar ethylene/air diffusion flame”, *Proc. Combust. Inst*., vol.29, 2002, pp. 2359–65.

[54] H. Guo, F. Liu, G.J. Smallwood and Ö.L. Gülder, “Numerical study on the influence of hydrogen addition on soot formation in a laminar ethylene–air diffusion flame”, *Combust. Flame,* vol. 145, 2006, pp. 324–38.

[55] A. Habibi, B. Merci and D. Roekaerts, “Turbulence radiation interaction in Reynold-averaged Navier-Stokes simulations of nonpremixed piloted turbulent laboratory scale flames”, *Combust. Flame*, vol. 151, 2007, pp. 303–20.

[56] K. Hanjalic, “Achievements and limitations in modeling and computation of buoyant turbulent flows and heat transfer”, *Proceedings of the 10th International Heat Transfer Conference*, 1994, pp. 1–18.

[57] G. Heskestad, “A reduced-scale mass fire experiment”, *Combust. Flame*, vol. 83, 1991, pp. 293–301.

[58] A. Heyl and H. Bockhorn, “Flamelet modeling of NO formation in laminar and turbulent diffusion flames”, *Chemosphere*, vol. 42, 2001, pp. 449–62.

[59] S. Hostikka, K.B. McGrattan and A. Hamins, “Numerical modeling of pool fires using LES and finite volume method for radiation”, *Proceeding of the 7th International Symposium on Fire Safety Science*, ed. D.D. Evans, International Association for Fire Safety Sciences, Boston, 2003, pp. 383–94.

[60] H.C. Hottel and A.F. Sarofim, “Radiative transfer”, New York, McGraw-Hill, 1967.

[61] I.M. Kennedy, C. Yam, D.C. Rapp and R.J. Santoro, “Modeling and measurements of soot and species in a laminar diffusion flame”, *Combust. Flame*, vol. 107, 1996, pp. 368–82.

[62] I.M Kennedy, “Models of soot formation and oxidation”, *Prog. Energy Combust. Sci*., vol.23, 1997, pp. 95–132.

[63] M. Klassen, Y.R. Sivathanu and J.P. Gore, “Simultaneous emission absorption measurements in toluene fuelled pool flames: mean and rms properties”, *Combust. Flame*, vol. 90, 1992, pp. 34–44.

[64] A. Klassen and J.P. Gore, “Structures and Radiation Properties of Pool Fires”, *NIST-GCR94-651*, 1994.

[65] W. Kollmann, I.M. Kennedy, M. Metternich and J.Y. Chen, “Application of a soot model to a turbulent ethylene diffusion flame”, in: “Soot Formation in Combustion: Mechanism and Models”, ed. H. Bockhorn, Springer-Verlag, 1994.

[66] M.E. Kounalakis, J.P. Gore and G.M. Faeth, “Turbulence radiation interactions in non premixed hydrogen/air flames”, *Proc. Combust. Inst.*, vol. 22, 1988, 1281–90.

[67] M.E. Kounalakis, J.P. Gore and G.M. Faeth, “Mean and fluctuating radiation properties of non premixed turbulent carbon monoxide/air flames”, *ASME J. Heat Transfer*, vol. 111, 1989, 1021–30.

[68] U.O. Koylü, Y.R. Sivathanu, and G.M. Faeth, “Carbon monoxide and soot emissions from buoyant turbulent diffusion flames”, *Proceeding of the 3th International Symposium on Fire Safety Science*, eds. G. Cox and B. Langford, International Association for Fire Safety Sciences, Elsevier Applied Science, London and New York, 1991, pp. 625–34.

[69] G. Krishnamoorthy, R. Rawat, J. Spinti and P. J. Smith, “Numerical modeling of radiative heat transfer in pool fire simulations”, *Proceedings of IMECE2005*, Orlando, 2005.

[70] G. Krisnamoorthy, “A comparison of gray and non-gray modeling approaches to radiative transfer in pool fire simulations”, *J. Hazard. Mater*., vol. 182, 2010, pp. 570–80.

[71] A Kronenburg, R.W Bilger and J.H Kent, “Modeling soot formation in turbulent methane–air jet diffusion flames”, *Combust. Flame,* vol. 121, 2000, pp. 24–40.

[72] A.A. Lacis and V. Oinas, “A description of the correlated k-distribution method for modeling non-gray gaseous absorption, thermal emission, and multiple scattering in vertically inhomogeneous atmospheres”, *J. Geophys Res*., vol. 96, 1991, pp. 9027–63.

[73] J. Lahaye and G. Prado, In: “Particulate Carbon Formation During Combustion”, chapter Morphology and Internal Structure of Soot and Carbon Blacks, Plenum Press, 3 edition, 1981.

[74] C.W. Lautenberger, J.L. De Ris, N.A. Dembsey, J.R. Barnett and H.R. Baum, “A simplified model for soot formation and oxidation in CFD simulation of non-premixed hydrocarbon flames”, *Fire Safety. J.*, vol. 40, 2005, pp. 141–76.

[75] C.W. Lautenberger and A.C. Fernandez-Pello, “A model for the oxidative pyrolysis of wood”, *Combust. Flame*, vol. 156, 2009, pp. 1503–13.

[76] K.O. Lee, C.M. Megaridis, S. Zelepouga, A. Saveliev, L.A. Kennedy, O. Charon and F. Ammouri, “Soot Formation Effects of Oxygen Concentration in the Oxidizer Stream of Laminar Coannular Nonpremixed Methane/Air Flames, *Combust. Flame*, vol. 121, 2000, pp. 323–33.

[77] K.M. Leung, R.P. Lindstedt and W.P. Jones, “A simplified reaction mechanism for soot formation in nonpremixed flames”, *Combust. Flame*, vol. 87, 1991, pp. 289–305.

[78] G. Li and M.F. Modest, “Application of composition pdf method in the investigation of turbulence-radiation interactions”, *J. Quant. Spectrosc. Radiat. Transfer*, vol. 73, 2002, pp. 461–72.

[79] G. Li and M.F. Modest, “Importance of turbulence-radiation interactions in turbulent reacting flows”, *ASME J. Heat Transfer*, vol. 125, 2003, pp. 454–62.

[80] R.P. Lindstedt, in: “Soot Formation in Combustion: Mechanism and Models”, ed. H. Bockhorn, Springer-Verlag, 1994, p. 417.

[81] F. Liu, Ö.L. Gülder and G.J. Smallwood. “Non-grey gas radiative transfer analyses using the statistical narrow-band model”, Int. J. Heat Mass Transf., vol. 41, 1998, pp. 2227–36.

[82] F. Liu, G.J. Smallwood and O.L. Gülder, “Radiation heat transfer calculations using the SNBCK method”, *AIAA Paper 99-3679*, 1999.

[83] F. Liu, “Numerical solutions of three-dimensional non-gray gas radiative transfer using the statistical narrow-band model”, *ASME J. Heat Transfer*, vol. 121, 1999, 200–3.

[84] F. Liu, G.J. Smallwood and Ö.L. Gülder, “Application of the statistical narrow-band correlated-k method to low-resolution spectral intensity and radiative heat transfer calculations-effects of the quadrature scheme”, *Int. J. Heat Mass Transfer*, vol. 43, 2000 pp. 3119–135.

[85] F. Liu, G.J. Smallwood and Ö.L. Gülder, “Band lumping strategy for radiation heat transfer using a narrow-band model”, *J. Thermophys Heat Transfer*, vol. 14, 2000, pp. 278–81.

[86] F. Liu, G.L. Smallwood and Ö.L. Gülder, “Application of the statistical narrow-band correlated-k method to non-grey gas radiation in CO2/H2O mixtures: approximate treatments of overlapping bands”, *J. Quant. Spectrosc. Radiat. Transfer*, vol. 68, 2001, pp. 401–17.

[87] F. Liu and J. X. Wen, “The effect of turbulence modelling on the CFD simulation of buoyant diffusion flames”, *Fire Safety J*., vol. 37, 2002, pp. 125–50.

[88] F. Liu, H. Guo, G.J. Smallwood and O.L. Gülder, “Effects of gas and soot radiation on soot formation in a coflow laminar ethylene diffusion flame”, *J. Quant. Spectrosc. Radiat. Transfer*, vol. 73, 2002, pp. 409–21.

[89] F. Liu, H. Guo, G.J. Smallwood and Ö.L. Gülder, “Numerical modeling of soot formation and oxidation in non-smoking and smoking ethylene diffusion flames”, *Combust. Theory Model.*, vol. 7, 2003, pp. 301–15.

[90] F. Liu, H. Guo, and G.J. Smallwood, “Effects of radiation model on the modeling of a laminar coflow methane/air diffusion flame”, *Combust. Flame*, vol. 138, 2004, pp. 136–54.

[91] F. Liu, H. Guo and G.J. Smallwood, “Evaluation of the laminar diffusion flamelet model in the calculation of an axisymmetric coflow laminar ethylene–air diffusion flame”, *Combust. Flame,* vol. 144, 2006, pp. 605–18.

[92] F. Liu, K.A. Thomson, H. Guo and G.J. Smallwood, “Numerical and experimental study of an axisymmetric coflow laminar methane–air diffusion flame at pressures between 5 and 40 atmospheres”, *Combust. Flame,* vol. 146, 2006, pp. 456–71.

[93] A.E. Lutz, R.J. Kee, J.F. Grcar and F.M. Rupley, “OPPDIF: a fortran program por computing opposed-flow diffusion flames”, Sandia National Laboratories, Report SAN96-8243, http://www.sandia.gov/chemkin/docs/OPPDIFabs.html

[94] U. Maas and S.B. Pope, “Simplifying chemical kinetics: Intrinsic low-dimensional manifolds in composition space”, *Combust. Flame*, vol. 88, 1992, pp. 239–64.

[95] D.B. Makel and I.M. Kennedy, “Soot formation in laminar inverse diffusion flames”, *Combust. Sci. Technol*., vol. 97, 1994, pp.303–14.

[96] O. Marin and R.O. Buckius, “Wideband correlated-k method applied to absorbing, emitting, and scattering media”, *J. Thermophys. Heat Transfer*, vol. 10, 1996, pp. 364–71.

[97] G.H. Markstein and J. de Ris, “Radiant emission and absorption by laminar ethylene and propylene diffusion flames”, *20th Symp. Int. Combustion/The Combustion Institute*, 1985, pp. 1637–46.

[98] B.J. McCaffrey, “Purely buoyant diffusion flames: some experimental results”, NBSIR 79-1910, NIST, 1979.

[99] K. McGrattan, H. Baum, R. Rehm, W. Mell, R. McDermott, S. Hostikka and J. Floyd, “Fire dynamics simulator (FDS) technical reference guide”, *NIST Special Publication 1018-5*, 2007.

[100] J.T. McKinnon and J.B. Howard, “The roles of PAH and acetylene in soot nucleation and growth," *Proc. Combust. Inst*., vol. 24, 1992, pp. 965–71.

[101] C.M. Megaridis and R.A. Dobbins, “Soot aerosol dynamics in a laminar ethylene diffusion flame”, *22th Symp. Int. Combustion/The Combustion Institute*, 1988, pp. 353–62.

[102] C.M. Megaridis and R.A. Dobbins, “Comparison of Soot Growth and Oxidation in Smoking and Non–Smoking Ethylene Diffusion Flames”, *Combust. Sci. and Tech*., vol. 66, 1989, pp. 1–16.

[103] R. S. Mehta, “Detailed modeling of soot formation and turbulence-radiation interaction in turbulent jet flames”, Ph.D. Thesis, The Pennsylvania State University, 2008.

[104] R.S. Mehta, D.C. Haworth and M.F. Modest, “Composition pdf/photon Monte Carlo modeling of moderately sooting turbulent jet flames”, *Combust. Flame*, vol. 157, 2010, pp. 982–94.

[105] R. S. Mehta, M. F. Modest, and D. C. Haworth, “Radiation characteristics and turbulence–radiation interactions in sooting turbulent jet flames”, Combust. Theory Model., vol. 14, 2010, pp. 105–24.

[106] S. Melis and L. Audouin, “Effect of Vitiation on the Heat Release Rate in Mechanically-Ventilated Pool Fires”, *Fire Safety Science - Proceedings of the Ninth International Symposium*, International Association for Fire Safety Science, 2008, pp. 931–42.

[107] M.A. Mikofski, T.C. Willims, C.R. Shaddix and L.G. Blevins, “Flame height measurement of laminar inverse diffusion flames”, *Combust. Flame*, vol. 146, 2006, pp. 63–72.

[108] M.A. Mikofski, T.C. Willims, C.R. Shaddix, A.C. Fernandez-Pello and L.G. Blevins, “Structure of laminar sooting inverse diffusion flames”, *Combust. Flame*, vol. 149, 2007, pp. 463–78.

[109] M.F. Modest, “Radiative Heat Transfer, second ed.”, Academic Press, New York, 2003.

[110] M.F. Modest, “The weighted-sum-of-gray-gases model for arbitrary solution methods in radiative transfer”, *ASME J. Heat Transfer*, vol. 113, 1991, pp. 650–56.

[111] M.F. Modest and H. Zhang, “The full-spectrum correlated-k distribution for thermal radiation from molecular gas-particulate mixtures”, *ASME J. Heat Transfer*, vol. 124, 2002, pp. 30–8.

[112] M.F. Modest, “Narrow-band and full-spectrum k-distributions for radiative heat transfer correlated-k vs. scaling approximation”, *J. Quant. Spectrosc. Radiat. Transfer*, vol. 76, 2003, pp. 69–83.

[113] M.F. Modest and R.S. Mehta, “Full spectrum k-distribution correlations for CO2 from the CDSD-1000 spectroscopic databank”, *Int. J. Heat Mass Transfer*, vol. 47, 2004, pp. 2487–91.

[114] M.F. Modest and R.J. Riazzi, “Assembly full spectrum *k*-distribution from a narrow band database: effects of mixing gases, gases and non-gray absorpting particles and non-gray scatters in non-gray enclosures”, *J. Quant. Spectrosc. Radiat. Transfer*, vol. 90, 2005, pp. 169–89.

[115] M. F. Modest and V. Singh, “Engineering correlations for full spectrum k-distributions of H2O from the HITEMP spectroscopic databank”, *J. Quant. Spectrosc. Radiat. Transfer*, vol. 93, 2005, pp. 263–71.

[116] J.B. Moss, C.D. Stewart and K.J. Syed, “Flowfield modelling of soot formation at elevated pressure”, *Proc. Combust. Inst*., vol. 22, 1988, pp. 413–23.

[117] J.B. Moss, C.D. Stewart and K.J. Young, “Modeling soot formation and burnout in a high temperature Laminar diffusion flame burning under oxygen-enriched conditions”, *Combust. Flame*, vol. 101, 1995, pp. 491–500.

[118] J.B. Moss and I.M. Aksit, “Modelling soot formation in a laminar diffusion flame burning a surrogate kerosene fuel”, *Proc. Combust. Inst*., vol. 31, 2007, pp. 3139–46.

[119] J.J. Murphy and C.R. Shaddix, “Soot properties and species measurements in a two-meter diameter JP-8 pool fire”, *Sandia Report*, SAND20034246, 2003.

[120] J. Nagle and R.F. Strickland-Constable, “Oxidation of carbon between 1000-2000°C”, *Proc. 5th conference on carbon*, 1962 London: Pergamon Press, pp. 154–64.

[121] F. Nmira, “Modélisation et simulation numérique de l’interaction entre un feu et un brouillard d’eau”, Thèse de Doctorat de l’Université de Provence, Marseille, 2007.

[122] N. Peters, “Laminar diffusion flamelet models in non-premixed turbulent combustion”, *Prog. Energy Combust. Sci.*, vol. 10, 1984, pp. 319–39.

[123] J.B.M. Pierce and J.B. Moss, “Smoke production, radiation heat transfer and fire growth in a liquid-fuelled compartment fire”, *Fire Safety J*., vol. 42, 2007, pp. 310–20.

[124] L. Pierrot, Ph. Riviere, A. Soufiani and J.Taine, “A fictitious-gas-based absorption distribution function global model for radiative transfer in hot gases”, *J. Quant. Spectrosc. Radiat. Transfer*, vol. 62, 1999, pp. 609–24.

[125] H. Pitsch, N. Peters, “A consistent flamelet formulation for non-premixed combustion considering differential diffusion effects”, *Combust. Flame*, vol. 114, 1998, pp. 26-40.

[126] T. Poinsot and D. Veynante, “Theoretical and numerical combustion”, R.T. Edwards, 2001.

[127] R. Porter, F. Liu, M. Pourkashanian, A. Williams and D. Smith, “Evaluation of solution methods for radiative heat transfer in gaseous oxy-fuel combustion environments”, *J. Quant. Spectrosc. Radiat. Transfer*, vol. 111, 2010, pp. 2084–94.

[128] B. Porterie, D. Morvan, J.C. Loraud and M. Larini, “Firespread through fuel beds: modeling of wind-aided fires and induced hydrodynamics”, *Physics of Fluid*, vol. 12, 2000, pp. 1762–82.

[129] Z. Qin, V.V. Lissianski, H. Yang, W.C. Gardiner, S.G. Davis and H.Wang, “Combustion chemistry of propane: A case study of detailed reaction mechanism optimization”, *Proc. Combust. Inst*., vol. 28, 2000, pp. 1663–69.

[130] J.G. Quintiere and B.S. Grove, “A unified analysis for fIre plumes”, *27th Symp. Int. Combustion/ The Combustion Institute*, 1998, pp. 2757–86.

[131] G.D. Raithby and E.H. Chui, “A finite volume method for predicting a radiant heat transfer in enclosures with participating Media”, *ASME J. Heat Transfer*, vol. 112, 1990, pp. 415–23.

[132] Ph. Riviere, D. Scutaru, T. Soufiani and J. Taine, “A new ck data basis suitable from 300 to 2500 K for spectrally correlated radiative transfer in CO2-H2O-transparent gas mixtures”, *Proceedings of the 10th International Heat Transfer Conference*, 1994 Brighton UK, vol. 2, pp. 129–34.

[133] Ph. Riviere, A. Soufiani, Y. Perrin, H. Riad and A. Gleizes, “Air mixture radiative property modelling in the temperature range 10000-40000 K”, *J. Quant. Spectrosc. Radiat. Transfer*, vol. 56, 1996, pp. 29–45.

[134] F.G. Roper, “The prediction of laminar jet diffusion flame sizes: Part I. Theoretical model”, *Combust. Flame,* vol. 29, 1977, pp.219–26.

[135] R.J. Santoro, T.T. Yeh, J.J. Horvath and H.G. Semerjian, “The transport and growth of soot particles in laminar diffusion flames”, *Combust. Sci. and Tech*., vol. 53, 1987, pp. 89–115.

[136] S.S. Sazhin, E.M. Sazhina, O. Faltsi-Saravelou and P. Wild, “The P-1 model for thermal radiation transfer: advantages and limitations”, Fuel, vol. 75, 1996 pp. 289–94.

[137] Y.R. Sivathanu, J.P. Gore and J. Dolinear, “Transient scalar properties of strongly radiative jet flames”, *Combust. Sci. Technol.*, vol. 76, 1991, 45–66.

[138] Y.R. Sivathanu and J.P. Gore, “Transient structure and radiation properties of strongly radiant buoyant flames”, *ASME J. Heat Transfer*, vol. 114, 1992, pp. 659–65.

[139] G.P. Smith, D.M. Golden, M. Frenklach, N.W. Moriarty, B. Eiteneer, M. Goldenberg, C.T. Bowman, R.K. Hanson, S. Song, W.C. Gardiner Jr., V.V. Lissianski and Z. Qin, http://www.me.berkeley.edu/gri_mech/.

[140] T.F. Smith, Z.F. Shen and J.N. Friedman, “Evaluation of coefficients for the weighted sum of gray gases model”, *ASME J. Heat Transfer*, vol. 104, 1982, pp. 602–8.

[141] M.D. Smooke, C.S. McEnally, L.D. Pfefferle, R.J. Hall and M.B. Colket, “Computational and experimental study of soot formation in a coflow, laminar diffusion flame”, *Combust. Flame*, vol. 117, 1999, pp. 117–39.

[142] K.C. Smyth, “Diffusion flame measurements of species concentrations, soot concentration, temperature, and velocity”, http://www.fire.nist.gov/fire/flamedata/.

[143] A.Y. Snegirev, “Statistical modeling of thermal radiation transfer in buoyant turbulent diffusion flames”, *Combust. Flame*, vol. 136, 2004, pp. 51–71.

[144] V.P. Solovjov and B.W. Webb, “SLW modeling of radiative transfer in multicomponent gas mixtures”, *J. Quant. Spectrosc. Radiat. Transfer*, vol. 65, 2000, pp. 655–72.

[145] V.P. Solovjov and B.W. Webb, “An efficient method for modeling of radiative transfer in multicomponent gas mixtures with soot particles”, ASME J. Heat Transfer, vol. 123, 2001, pp. 450–7.

[146] A. Soufiani and J. Taine, “High temperature gas radiative property parameters of statistical narrow-band model for H2O, CO2 and CO and correlated-k model for H2O and CO2”, *Int. J. Heat Mass Transfer*, vol. 40, 1997, 987–91.

[147] J.M. Souil, P. Joulain and E. Gengembre, “Experimental and theoretical study of thermal radiation from turbulent diffusion flames to vertical target surfaces”*, Combust. Sci. Technol*., vol. 41, 1984, pp. 69–81.

[148] K.C. Tang and M.Q. Brewster, “K-distribution analysis of gas radiation with non-gray, emitting, absorbing, and anisotropic scattering particles”, *ASME J. Heat Transfer*, vol. 116, 1994, pp. 980–85.

[149] S. Trottier, H. Guo, G.J. Smallwood and M.R. Johnson, “Measurement and modeling of the sooting propensity of binary fuel mixtures”, *Proc. Combust. Inst*., vol. 31, 2007, pp. 611–19.

[150] H.Y. Wang, P. Joulain and J.M. Most, “Modeling on burning of large-scale vertical parallel surfaces with fire-induced flow”, Fire Safety J., vol. 32, 1999, pp. 241–71.

[151] L. Wang, M.F. Modest, D.C. Haworth and S.R. Turns, “Modeling nongray gas-phase and soot radiation in luminous turbulent nonpremixed jet flames”, *Combust. Theory and Modelling*, vol. 9, 2005, pp. 673–91.

[152] A. Wang and M.F. Modest, “High accuracy, compact database of narrow-band k-distributions for water vapor and carbon dioxide”, *J. Quant. Spectrosc. Radiat. Transfer*, vol. 93, 2005, pp. 245–61.

[153] A. Wang, M. F. Modest, D. C. Haworth and L. Wang, “Monte Carlo simulation of radiative heat transfer and turbulence interactions in methane/air jet flames”, *J. Quant. Spectrosc. Radiat. Transfer*, vol. 109, 2008, pp. 269–79.

[154] Y. Wang, P. Chatterjee, and J.L. de Ris, “Large eddy simulation of fire plumes”, *Proc. Combust. Inst*., vol. 33, 2011, pp. 2473–80.

[155] J.X. Wen and L.Y. Huang, “CFD modelling of confined jet fires under ventilation-controlled conditions”, *Fire Safety J*., vol. 34, 2000, pp. 1–24.

[156] R.M. Woolley, M. Fairweather and M. Yunardi, “Conditional moment closure modelling of soot formation in turbulent, non-premixed methane and propane flames”, Fuel, vol. 88, 2009, pp. 393–407.

[157] J. Worthy, V. Sanderson and P. Rubini, “Comparison of Modified k-ε models for buoyant plumes”, *Numer. Heat Transfer Part B*, vol. 29, 2001, pp. 151–65.

[158] Y. Xin and J.P. Gore, “Two-dimensional soot distributions in buoyant turbulent fires”, *Proc. Combust. Inst*., vol. 30, 2005, pp. 719–26.

[159] Z. Yan and G. Holmstedt, “Fast narrow-band computer model for radiation calculations”, *Numer. Heat Transfer Part B*, vol. 31, 1997, pp. 61–71.

[160] Z. Yan and G. Holmstedt, “Three-dimensional computation of heat transfer from flames between vertical and parallel walls”, *Combust. Flame*, vol. 117, 1999, pp. 574–88.

[161] M. Yunardi, R.M. Woolley and M. Fairweather, “Conditional moment closure prediction of soot formation in turbulent, nonpremixed ethylene flames”, *Combust. Flame,* vol. 152, 2008, pp. 360–76.

[162] L. Zhang, A. Soufiani and J. Taine, “Spectral correlated and non-correlated radiative transfer in a infinite axisymmetric system containing an absorbing and emitting real gas-particle mixture”, *Int. J. Heat Mass Transf*., vol. 31, 1988, pp. 2261–72.

[163] X.L. Zhang, J.P. Vantelon, P. Joulain and A.C. Fernandez-Pello, “Influence of an external radiant flux on a 15-cm-diameter kerosene pool fire”, *Combust. Flame*, vol. 86, 1991, pp. 237–48.

[164] H. Zhang and M. Modest, “Evaluation of the Planck-mean absorption coefficients from HITRAN and HITEMP databases”, *J. Quant. Spectrosc. Radiat. Transfer*, vol. 73**,** 2002, pp. 649–53.

[165] J. Zhang, S. Dembele and J.X. Wen, “Effect of radiation models on CFD simulations of upward flame spread”, *8th Int. Symp. Fire Safety Sci*., Beijing, 2008.

[166] J. Zhang, S. Dembele, and J. X. Wen, “Investigation of turbulence models for CFD simulations of gas and liquid pool fires”, *J. Fire Sci*., vol. 27, 2009, pp. 157–82.

[167] Q. Zhang, H. Guo, F. Liu, G.J. Smallwood and M.J. Thomson, “Modeling of soot aggregate formation and size distribution in a laminar ethylene/air coflow diffusion flame with detailed PAH chemistry and an advanced sectional aerosol dynamics model”, *Proc. Combust. Inst*., vol. 32, 2009, pp. 761–68.

[168] Y. Zheng, R.S. Barlow and J.P. Gore, “Measurements and calculations of spectral radiation intensities for turbulent non-premixed and partially premixed flames”, *ASME J. Heat Transfer*, vol. 125, 2003, pp. 678–86.

[169] E.E. Zukoski, “Fluid Dynamic Aspects Of Room Fires”, *Proceedings of the First International Symposium on Fire Safety Science*, International Association for Fire Safety Sciences, Barkeley, CA, 1986, pp. 1–30